High Resolution Infrared Laser Spectroscopy in the Solid and Gas Phases

YANG, Mei

A Thesis Submitted in Partial Fulfillment

of the Requirements for the Degree of

Doctor of Philosophy

in

Chemistry

The Chinese University of Hong Kong

May 2015

Thesis Assessment Committee

Professor LIU Zhifeng (Chair)

Professor CHAN Man Chor (Thesis Supervisor)

Professor CHAN Tak Wah Dominic (Committee Member)

Professor HU Shuiming (External Examiner)

Professor CHEUNG Allan Shi-Chung (External Examiner)

ABSTRACT

This thesis reports the high resolution laser spectroscopic studies of molecular systems in the mid- and near- infrared regions. In the system of solid parahydrogen, spectrum in the pure rotational and rovibrational W (ΔJ=6) transitions in the 4 μm and 1.5 μm regions respectively have been studied. A high resolution difference frequency laser spectrometer was constructed from scratch for the study of the pure rotational $W_0(0)$ (ΔJ=6) transition, while the rovibrational $W_1(0)$ (Δv=1, ΔJ=6) transition was studied using a home-built near infrared diode laser spectrometer. The exceedingly high resolution achieved by laser spectroscopy resolved the triplet structure for both transitions due to anisotropic crystal field interactions. Their corresponding crystal field parameters based on the model of localized exciton were determined. In addition, the temperature dependences of line profiles and transition frequencies in the range of 3.8-11.8 K were also studied for both transitions. These observations were consistent with the Debye's model for the dephasing of two-level system by acoustic phonons in the bulk crystal.

Coupled with laser ablation and free jet expansion, high resolution laser induced fluorescence spectroscopy in the near infrared region was applied in the study of three transition metal containing diatomic molecules including RuC, IrP and IrB in the gas phase. For RuC molecule, rotational resolved electronic spectrum have been observed in the range of 12000-14060 cm^{-1}, covering the $^3\Pi_2$-$[0.1]^3\Delta_3$, the $[13.9]^3\Phi_4$-$[0.1]^3\Delta_3$, the $[13.5]^3\Phi_3$-$[0.9]^3\Delta_2$, and the $[13.9]^3\Pi_1$-$[0.9]^3\Delta_2$ band systems. The resolution of our spectrum allowed partially resolved hyperfine structure for both ^{99}RuC and ^{101}RuC isotopes. Accurate molecular constants for all seven RuC isotopic molecules were obtained and hyperfine constants for the $[0.1]^3\Delta_3$, $[12.7]^3\Pi_2$

and [13.9]$^3\Phi_4$ states of both ^{99}RuC and ^{101}RuC isotopes were retrieved and analyzed. For IrP molecule, new electronic transition systems were observed in the range of 12000-14000 cm^{-1} and the molecular constants for both ^{193}IrP and ^{191}IrP isotopes were obtained. For IrB molecule, a new $^3\Delta_3$-X$^3\Delta_3$ transition system was identified with the molecular constants of two isotopes ^{191}Ir^{11}B and ^{193}Ir^{11}B derived.

Abstract of thesis entitled:

High Resolution Laser Spectroscopy in the Solid and Gas Phases

Submitted by YANG, Mei

for the degree of Doctor of Philosophy in Chemistry

at The Chinese University of Hong Kong in May 2015

中文摘要

本論文旨在利用高分辨激光光譜研究中紅外以及近紅外波段的分子體系。首先在固態氫體系中，我們主要研究其分別位於 4 μm 及 1.5 μm 的純轉動和振動轉動的 W 躍遷（ΔJ=6）。我們搭建了一套全新的差頻激光光譜儀用以研究純轉動的 $W_1(0)$躍遷（ΔJ=6）；另外振動轉動 $W_0(0)$躍遷（Δv=1，ΔJ=6）則是用到自行搭建的近紅外二極管激光光譜儀。由於激光光譜的分辨率極高，兩種 W 躍遷都觀察到晶體場效應導致的三重分裂結構，我們基於定態激子模型還得到了相應的晶體場常數。另外，我們還研究了兩種 W 躍遷的線型、頻率與溫度的關係（溫度在 3.8 K 至 11.8 K 區間），并基於德拜兩能級弛豫模型對此做出解釋，相信主要是由於晶體內聲子散射所引致的。

另外我們還研究了三種含過渡金屬元素的氣態雙原子分子，分別是 RuC、IrP 和 IrB。通過聯用激光消融及超聲射流技術，我們研究這些分子體系在近紅外波段的激光誘導熒光光譜。對於 RuC 分子，我們記錄了 12000 至 14000 cm^{-1} 波段的電子光譜，包擴$[12.7]^3\Pi_2$-$[0.1]^3\Delta_3$、 $[13.9]^3\Phi_4$-$[0.1]^3\Delta_3$、$[13.5]^3\Phi_3$-$[0.9]^3\Delta_2$ 和 $[13.9]^3\Pi_1$-$[0.9]^3\Delta_2$ 這四個譜帶系統，并分析得到了所有七種同位素分子的各項分子常數。由於極高的分辨率，我們觀察到 ^{99}RuC 和 ^{101}RuC 這兩個同位素分子的超精細結構，并得到了它們的$[0.1]^3\Delta_3$、$[12.7]^3\Pi_2$、$[13.9]^3\Phi_4$ 這三個電子態的超精細常數。對於 IrP 分子，我們在 12000 至 14000 cm^{-1} 波段發現了新的電子態躍遷，并得到 ^{193}IrP 和 ^{191}IrP 這兩種同位素分子的分子常數。對於 IrB 分子，我們指認了一個新的電子態躍遷 $^3\Delta_3$-$X^3\Delta_3$，并得到了 $^{191}Ir^{11}B$ and $^{193}Ir^{11}B$ 這兩種同位素分子的分子常數。

ACKNOWLEDGEMENTS

I own the most sincere gratitude to my supervisor, Prof. CHAN Man-Chor, for his brilliant ideas, patient guidance, discussion, encouragement and criticisms through my Ph.D research study. He is always full of passion and energy, with permanent interest and enthusiasm in science. I have learned not only knowledge about science and experiments, but also how to do things, how to deal problems.

I also appreciate so much for the support and supervise form Prof. CHEUNG A. S-C. in HKU. He is very nice, patient, and also strict. He taught me the technique in spectral analysis, and always encouraged me on my research. Thanks are also given to Dr. MA Tongmei, Dr. XIA Ye, Dr. NG Tony, and Dr. WANG Na from his group, who gave me a lot of help and discussions in my experiments.

I also want to give my thanks to the group members in Prof. CHAN's group. They are Dr. SONG Yan, Dr. YAN Lei, Dr. LIAO Zhenwu, Mr LI Biuwa , and Mr CHOW Gary and Mr TSANG Ling Fung. Dr. Yan Song and Dr. Lei YAN taught me many things including studying and living in Hong Kong when I was a freshman here. Special thanks should be given to Dr. LIAO Zhenwu LIAO and Mr LI Biuwa, they are my partners in my experiments, giving me solid support and help. Without them, I would not complete my experiments.

Acknowledgement is also given to the staff of technical support unit for their assistance and professional suggestions, which made my research more smoothly.

Finally I would like to express my deepest gratitude to my family and my friends for their forever love and trust. Thanks again to my dear husband and lovely son, who complete my life.

Table of Contents

List of Figures

List of Tables

Chapter 1 **Introduction**

Since the innovation of laser, a revolutionary development of molecular spectroscopy has been witnessed. Due to the monochromaticity and high power density of laser sources, the resolution and sensitivity of spectrum have been greatly improved. The high resolution achieved by laser spectroscopy allows the study of very detailed structure of spectrum, e.g. hyperfine structure due to nuclear spin interactions.[1,2] The high sensitivity makes possible the spectroscopic study of transient species, such as radicals,[3,4] molecular ions[5] and gas phase transition metal compounds at very low abundance.[6] High resolution spectroscopy has been well routinely applied in the study of gaseous molecular species, as well as condensed phase matter in some cases. In this thesis, I will present our experiments of high resolution spectroscopy of a classic quantum crystal: solid parahydrogen and gas phase transition metal compounds.

Solid hydrogen is considered the simplest molecular solid. H_2 molecules remain much of their identities in condensed phases. As a result, both solid and liquid hydrogens exhibit rovibrationally assignable spectra. Although the rovibrational spectrum of gaseous H_2 is strictly dipole forbidden, hydrogens in condensed phases possess a very strong infrared spectra from far to near IR due to intermolecular multipole-induced mechanisms.[7,8] Since the induced dipole and corresponding excitation and relaxation processes are collective property involving all molecules in the system, the properties of hydrogen crystal structure as well as individual molecules contribute to the selection rules, transition frequencies and intensities and so on. On the other hand only properties of isolated molecules are considered for gaseous H_2.

The first observation of pure rotational Raman spectrum of liquid hydrogen was reported by McLennan and McLeod in 1929.[9] Since the monumental study, numerous spectroscopic studies have been reported to reveal many new properties of condensed phase hydrogen.[7,10] Molecular rotation, vibration, orientation and multipolar interactions coupled to lattice vibration (phonon) give rise to the unique

phenomena – phonon-broadening spectral lines, relaxation and dephasing processes, phonon-exciton resonance, and phonon-renormalization etc, which can be investigated using spectroscopic means. In addition, anisotropic intermolecular interactions are so weak to give rise to the crystal field splitting of the rovibrational spectrum.[11] The most exciting issue about spectroscopy of solid hydrogen is the narrow linewidth observed in p-H_2 crystals. The typical linewidth is so narrow that the typical crystal field splitting fine structure can be fully resolved for the detailed study of anisotropic intermolecular interactions.

The narrowness of spectral transitions has been interpreted by the localization of excitation energy (localized excitons) in p-H_2 crystals. To date, the sharpest spectral line observed is the coherent Raman $Q_1(0)$ transition of solid p-H_2, at about 4149.64 cm^{-1} with a linewidth(HWHM) of 5 MHz.[12] Other transitions with typical linewidths less than 0.1 cm^{-1} in p-H_2 crystals include the multipole induced $W_0(0)$ transitions,[11,13] external field induced $Q_1(0)$ transitions,[12,14,15] and zero-phonon $Q_1(1)$ transitions,[16,17] etc. High resolution spectroscopy allows us to resolve the sharp sometimes even dense features in the spectrum of solid hydrogen, which may provide information on the structure and dynamics of this quantum solid. The accurate structural data obtained from experiments also serve as rigorous tests for the theoretical calculations and simulations about quantum solid.

Additionally, I also involved in spectroscopic studies of gas phase transition metal compounds. Transition metals are important species in chemistry, involved in organometallic chemistry,[18,19] catalysis,[20] surface science,[21] high temperature chemistry,[22,23] astrophysics[24,25] and so on. For example, many transition metal compounds are known catalysts for chemical reactions. These unique properties may be ascribed to the d electrons, which can easily form both σ and π bonds with other elements. As a result, transition metals are bonded to most elements or ligand or molecules (both organic and inorganic). Furthermore, the multiple valence of transition metal elements allow them to change between different oxidation states during chemical reactions, which is an essential property as an active catalytic center. Despite their importance in chemistry, the understanding of transition metal compounds is still very limited in both theoretical and experimental aspects. Ab initio calculations cannot provide reliable predictions for even the simple system such as

diatomic molecules.[26] Since the energies of n*d* electrons are close to those of (n+1)*s* and (n+1)*p*, their involvement in chemical bonding makes the electron correlation vital in determine the energies of electronic states. However, there is no general routine to accurately evaluate the effect of electron correlation under the orbital approximation even in modern high level computations. On the other hand, it is an experimental challenge to prepare the transition metal compounds with sufficient abundance for structural studies.[27] In our experiments, transition metal-containing diatomic molecules in the gas phase were produced in mild experimental condition using laser ablation of transition metal followed by reaction with reagent gas. By supersonic expansion of the reaction mixture into high vacuum, the corresponding cooling effect allows the molecules to reach low rotational and translational temperatures, which largely simplify the spectrum.

Transition metal containing diatomic molecules often possess a number of low-lying electronic states due to the involvement of d electrons, and the corresponding transitions lie in the near IR and visible regions.[28] Laser induced fluorescence (LIF) has been widely used in studying the corresponding electronic spectrum because of its very high sensitivity that is particularly suited for species at very low abundance with short life.[29] In this approach, molecules in the ground or low-lying electronic states are excited by a tunable high resolution laser, and the fluorescence emission is collected. By plotting the emission against the excitation frequency, we can obtain a rovibrationally resolved LIF spectrum similar to the corresponding absorption spectrum.

In the following chapters of this thesis, I will give a brief review on the molecular levels of diatomic molecules in chapter 2. In chapter 3, the detailed experimental setups including (1) our home-built absorption laser spectrometers and the cryostats used for the study of solid hydrogen and (2) the LIF spectrometers and the gas handling chamber for the study of transition metal containing diatomic molecules are presented. In chapter 4, the temperature effects on the transition frequency, crystal field splitting, and line profiles of W transitions of solid p-H_2 are discussed. In chapter 5, the electronic transitions of seven RuC isotopic species in the NIR region are reported with derived molecular constants including the hyperfine constants for each isotopic species. In chapter 6, the preliminary results of the electronic transitions of

IrP and IrB are reported. Finally a concluding remark is given in chapter 7.

Chapter 2 **Molecular energy levels of diatomic molecules**

2.1 Born-Oppenheimer approximation

The energy levels of a molecule are given by the eigenvalues of the time independent Schrodinger Equation $\mathrm{H}\Psi = E\Psi$.[30] Since the motions of electrons and nuclei are mutually correlated, the Schrodinger equation is unsolvable without making approximation. Born-Oppenheimer approximation is commonly employed to separate the motions of electrons and nuclei.[31] The physical content of this separation is based on the great mass difference between electrons and nuclei. By carefully choosing the coordinate systems, the coupling between motions of electrons and nuclei can be minimized. Under the B.O. approximation, the coupling energy is neglected and the energy of a molecular system is composed of nuclear part and electronic part. The detailed discussion of the B.O. approximation can be found elsewhere.[32]

For diatomic molecules, the total wavefunction is expressed as

$$\Psi_{total} = \Psi_{el}(r,R)\Psi_N(R),$$

with the total energy

$$E_{total} = E_{el} + E_N .$$

Under the B.O. approximation, the Schrodinger equation can then be separated into two parts, *i.e.* the electronic part Ψ_{el} and the nuclear part Ψ_N respectively:

$$\mathrm{H}_{el}\Psi_{el}(r,R) = E_{el}(R)\Psi_{el}(r,R)$$

$$\mathrm{H}_N\Psi_N(R) = E_N(R)\Psi_N(R) .$$

The nuclear motion involves vibration and rotation. Since the magnitude of vibration-rotation coupling term is small at low vibrational states with atoms vibrate with only small amplitudes about their equilibrium positions, the two motions can be separated and described by independent Hamiltonians.[33] By solving the corresponding Schrodinger equation, the nuclear energy is expressed as the sum of vibration and rotation energies in forms of:

$$E_{vib} = (v+1/2)\omega_e - (v+1/2)^2\omega_e\chi_e + \cdots$$

$$E_{rot} = B_v J(J+1) - D_v J^2 (J+1)^2 + \cdots .$$

Here v and J are the vibrational and rotational quantum numbers. ω_e and B_v are the harmonic frequency and the rotational constant respectively. $\omega_e\chi_e$ and D_v in the correction terms are the anharmonic frequency and centrifugal distortion constant respectively. The total energy is then written as:

$$E_{total} = E_{el} + E_{vib} + E_{rot} .$$

2.2 Angular momentum coupling

The motion of charged particles (electrons and nuclei) in molecules generates magnetic dipoles that give rise to various intramolecular interactions. The corrections of energy arising from these interactions can be dealt with using different schemes of angular momentum coupling. For diatomic molecules, the different sources of angular momenta are listed below.[33]

L: electronic orbital angular momentum;

S: electron spin angular momentum;

J: total angular momentum;

N: total angular momentum excluding electron spin, N=J-S; and

R: rotational angular momentum of the nuclei, R=N-L.

Due to the axial symmetry of the system and the fact that electronic coordinates are expressed with respect to molecular fixed system, only the projection of L on the internuclear axis (z-axis) is a conserved quantity, which obeys momentum conservation in diatomic molecules. The precession of L onto the molecular z-axis gives the component M_L, which can have 2L+1 possible values:

$M_L = L, L-1 , L-2 , \ldots , -L$

Electronic states with different $|M_L|$ values may have different energies and the quantum number $\Lambda = |M_L|$ is commonly used to characterize the electronic states. It is obvious that:

$\Lambda = |M_L| = 0, 1, 2, \ldots$

and the electronic states are doubly degenerate for $\Lambda \neq 0$.

The electronic states (also known as spectroscopic terms) with Λ=0, 1, 2, 3, 4 … are

labeled by Σ, Π, Δ, Φ, Γ …, respectively.

Individual spin angular momentum of each electron couples to form the total spin angular momentum S of an electronic state. 2S+1 is the spin multiplicity to describe the electronic state. Similar to L, the precession of S gives 2S+1 possible projections onto the internuclear z-axis, which is denoted by Σ:

Σ = S, S-1, S-2, … ,-S.

Depending on the strength of the interactions among angular momenta, various coupling schemes, known as the Hund's cases, are obtained. The details of various Hund's cases can be found in Herzberg's classic book on diatomic molecules. Here we only discuss the two most common coupling cases, namely, case (a) and case (b), whose schematic vector diagrams are shown in Figure 2.1.

In Hund's case (a) is common for electronic states with $\Lambda \neq 0$. In this case, the interaction of spin angular momentum S and orbital angular momentum L is relatively strong. As a result, both Σ and Λ couple strongly along the molecular z axis. The sum of of Λ and Σ is denoted by Ω, the total angular momentum along the molecular axis:

$\Omega = \Lambda + \Sigma$.

Then Ω and R form the resultant total angular momentum J excluding nuclear spin:

$J = \Omega + R$.

Therefore for a given Ω:

$J = \Omega, \Omega + 1, \Omega + 2$…

In Hund's case (b), the coupling between R and L is much stronger than the spin-orbital coupling, so Λ is first coupled with R to form N:

$N = R + \Lambda$.

N is then coupled with S to form the total angular momentum J excluding nuclear spin:

$J = N + S$.

Therefore for a given N:

$J = N + S, N + S - 1, \ldots, |N-S|$.

Almost all the Σ states belong to Hund's case (b). Figure 2.1 shows the good quantum numbers for Hund's cases (a) and (b).

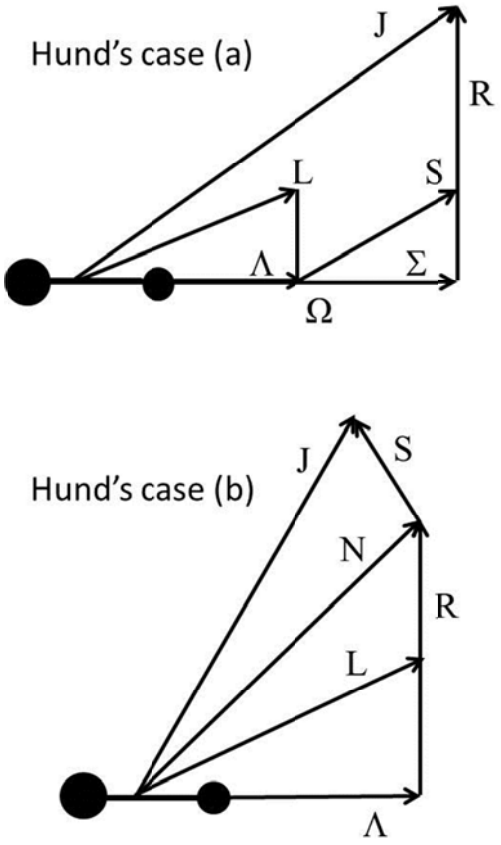

Figure 2.1 Vector diagram for the Hund's coupling case (a) and (b).

2.3 Selection rules

The rovibronic transitions of diatomic molecules are governed by selection rules that can be sassily derived based on symmetry considerations. For transitions due to electric dipole mechanism, the selection rules are listed below:

1. Parity of rovibronic states

$+ \leftrightarrow -$

2. Permutation symmetry (for molecules with identical nuclei)

$s \leftrightarrow s$， $a \leftrightarrow a$

3. Inversion symmetry

$g \leftrightarrow u$

4. Total angular momentum including nuclear spin

$\Delta F=0,\pm 1$

5. Total angular momentum excluding nuclear spin

$\Delta J=0,\pm1$

6. Nuclear spin

$\Delta I=0$

These are rigorous selection rules as they are based on rigorous symmetry properties. In addition, various approximate selection rules can be derived depending on the Hund's cases:

7. Orbital angular momentum along molecular axis

$\Delta\Lambda=0,\pm1$

$\Sigma^+ \leftrightarrow \Sigma^+, \Sigma^- \leftrightarrow \Sigma^-$ (for transitions between Σ states)

8. Electronic spin

$\Delta S=0$ (for spin-orbital coupling not very strong)

9. Electronic spin along molecular axis

$\Delta\Sigma=0$ (for Hund's case (a) only)

10. Total angular momentum (excluding nuclear spin) along molecular axis

$\Delta\Omega=0,\pm1$ (for Hund's case (a) only)

11. Total angular momentum (excluding electronic spin and nuclear spin)

$\Delta N=0,\pm1$ (for Hund's case (b) only)

2.4 Analysis of spectra

The experimental of spectra involves the following procedures: (1) to make assignment of quantum numbers in the observed transitions based on selection rules and spectral pattern; and (2) to derive the corresponding structural constants based on the assignment and the appropriate Hamiltonian using least- square fitting. The two procedures are often done repeatedly until the error of fitting is comparable to the experimental uncertainty. The effective Hamiltonian used for least-square fitting is written in a general form

$$H_{\text{eff}} = H_{el} + H_{vib} + H_{rot} + H_{SR} + H_{SO} + H_{SS} + H_{\Lambda} + H_{hyp} + H_{eqQ} + H_{NR},$$

in which the last seven terms represent the coupling of electron spin-rotation, electron spin-orbital, electron spin-electron spin, Λ-doubling, magnetic hyperfine, electric quadrupole and nuclear spin-rotation respectively. Detailed description of

physical content and expressions of these coupling terms can be found elsewhere.[33] Only some of these coupling terms are important for a particular electronic transition system. Once the effective Hamiltonian is determined, the rovibronic energy can be calculated by diagonalization of the Hamiltonian matrix using appropriate basis functions for the states. Correspondingly, with the energy of rovibronic states determined from observed transition frequencies in experiments, the structure parameters can be calculated from least square fitting.

Chapter 3 **Home-built apparatus for spectroscopic study**

Two sets of experimental apparatus have been used for the spectroscopic study of solid parahydrogen and gasous metal-containing diatomic molecules. Both setups include a high resolution spectrometer with coherent light source and a sample handling system.

Laser radiation has been widely used in spectroscopic experiments for several decades. Its unique properties such as coherence, good polarization, monochromaticity, high spectral power density and good collimation, make it a powerful light source in spectroscopic studies. Compared to dispersion spectrometers or Fourier transform interferometers, spectrometers based on tunable coherent light source such as laser radiation are advantageous with much better spectral resolution and polarization. A lot of laser techniques have been developed over the years, for instance, frequency modulation absorption spectroscopy, laser induced fluorescence (LIF), cavity ring-down laser absorption spectroscopy (CRLAS), resonance-enhanced multi-photon ionization (REMPI) *etc*.[29] These techniques provide high resolution and high detection sensitivity for spectroscopic studies.

However, commercial lasers are not always suited for spectroscopic experiments. It is therefore a common practice to custom-build laser spectrometers suited for specific experiments. Three home-built high resolution laser spectrometers have been used for the experiments described in this thesis including a mid-infrared difference frequency spectrometer and a near infrared diode laser spectrometer used in the study of solid hydrogen and a laser-induced fluorescence spectrometer for the study of gas phase transition metal diatomic molecules. In the following the details of the apparatus used in our experiments are described.

A. Apparatus for spectroscopic study of solid parahydrogen

In the study of solid hydrogen, two home-built spectrometers have been used to record spectra in the mid- and near- infrared regions. The sample system was composed of a gas handling system that was used to produce parahydrogen gas and a cryostat that was used to prepare solid parahydrogen samples. These components

are discussed below.

3.1 Mid-IR difference frequency spectrometer

The mid-IR difference frequency spectrometer was built from scratch for the study of solid parahydrogen. The common mid-IR laser sources, like CO/CO_2 gas laser, lead-salt diode laser, and optical parametric oscillator (OPO) laser, are either limited in tenability or expensive in price. With the Ti:Sapphire ring laser and high power single frequency diode fiber laser available in our laboratory, we built a coherent mid-infrared spectrometer based on difference frequency generation (DFG), which utilizes nonlinear optical materials to generate mid-IR radiations from the difference frequency of two near-IR or visible laser sources.[34]. In our case, a tunable high resolution Ti:Sapphire laser operated in the 700 nm region and a single frequency diode fiber laser at 1064 nm were mixed in a periodically poled lithium niobate (PPLN) crystal. By tuning the output frequency of the Ti:Sapphire laser, the output frequency of the infrared radiation can be changed continuously to cover wide spectral range as long as the phase matching condition is satisfied.

3.1.1 Difference frequency generation (DFG)

Difference frequency generation is a nonlinear optical frequency conversion technique. In a nonlinear crystal material where the phase-matching condition is satisfied, the DFG emission v_{idler} can be generated if the two beams v_{pump} and v_{signal} are mixed in the nonlinear material. The phase-matching condition includes the rules of conservation of energy hv and momentum k.

$$v_{pump} = v_{signal} + v_{idler}$$
$$\vec{k}_{pump} = \vec{k}_{signal} + \vec{k}_{idler}$$

In these equations, the momentum $\left|\vec{k}\right| = nc/\lambda$, in which n is the refractive index of light in the material, c is speed of light in vacuum and λ is the wavelength. The refractive index n depends on both the light frequency and the nonlinear material. In order to satisfy the phase-matching condition, traditional approach is limited to a small range of wavelengths that can be phase matched and the alignment and tuning

process are rather complicated. Periodically poled lithium niobate (PPLN) is an engineered, quasi-phase-matched material that is a good solution to overcome the problem.[35] In a PPLN crystal, the quasi-phase-matching condition is expressed as below,

$$\vec{k}_{pump} = \vec{k}_{signal} + \vec{k}_{idler} + \vec{k}_{PPLN} .$$

In this case, PPLN compensates the momentum difference between the two beams. The direction for maximum nonlinear coefficient is chosen to improve the conversion efficiency. The three light beams propagate in the same direction, so it is easy to for alignment. And the frequency tuning process is quite convenient through controlling the temperature of PPLN crystal.

The PPLN crystal used in our work was 40 mm long with several channels manufactured with difference poling periods for different working frequency ranges. It is mounted in a copper housing of an oven for temperature control of the PPLN to fulfill the quasi-phase-matching conditions. For our PPLN crystal, the signal beam was at 1064 nm. By tuning the Ti:Sapphire laser frequency and varying the temperature of the PPLN crystal, tunable mid-IR radiation was generated in the range of 2.4-5.0 μm. With inputs of the Ti:Sapphire and 1064 nm diode fiber laser set to about 400 mW and 700 mW respectively, a coherent infrared radiation of about tens of μW was generated.

3.1.2 Tone-burst modulation with an electro-optical modulator (EOM)

The high sensitivity of laser spectroscopy is achieved by removing the serious power noise background of the source based on modulation technique. In the study of solid hydrogen, the tone-burst frequency modulation was applied using an electro-optical modulator (EOM). The operation of the EOM is based on the linear electro-optic effect (or called Pockels effect), i.e. the linear dependence of the refractive index on the applied electric field *E*. The change of refractive index is expressed as $\Delta n = 1/2 n_e^3 r_{33} E$, in which n_e is the unperturbed refractive index and r_{33} is the appropriate element in the electro-optical tensor. When a sinusoidal voltage with radio frequency (RF) $V = V_0 \sin \omega_{rf} t$ is applied across the crystal with width *d* to give

an electric field *E=V/d*, the electric field of the laser with frequency ω_L transmitted through the phase-modulator with length *l* is

$$E(t) = E_0 e^{i\omega_L t} \sum_{n=-\infty}^{+\infty} J_n(\eta) e^{in\omega_{rf} t},$$

where $\eta = \omega_L n_e^3 r_{33} l V_0 / 2dc$ (here *c* is velocity of light) is modulation index and J_n are Bessel functions of order *n*. As a result, side bands with frequencies of integral number times modulation frequency are generated for the laser beam. In Figure 3.1(a), we show the dependeces of intensities of laser and its sidebands (i.e. $J_n(\eta)^2$) on the modulation index η. When $\eta<1$, all J_n almost vanish except J_0, and $J_{\pm1}$. In this case, a frequency modulated beam is generated with a strong intensity at frequency ω_L with two weaker sidebands at frequency $\omega_L \pm \omega_{rf}$ as seen in Figure 3.1(b).

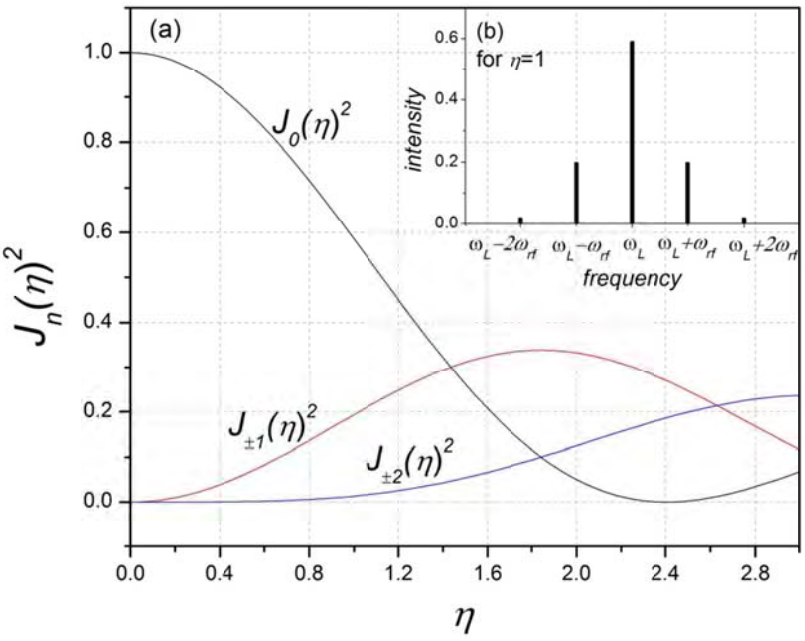

Figure 3.1 (a) Dependences of intensities of laser and its sidebands (in terms of $J_n(\eta)^2$) on modulation index η (for $\eta<3$ and only the first 4 sidebands are given here); (b) Intensities of laser and its sidebands, for $\eta=1$ as an example.

When the RF source is amplitude modulated with a square wave at several kHz, through a double-balanced mixer, consequently the sidebands are turned on and off at the corresponding frequency. This modulation method is called the tone-burst

modulation. When laser is scanned through the absorption lines, the tone-burst modulation will give a 2nd derivative spectrum at 1*f* lock-in detection provided that the RF frequency is comparable to the line width of the transition. This approach will significantly enhance the resolution of the spectrum as lines splitting comparable to line width can be fully resolved. It is particularly crucial in resolving the structure of the W transitions of solid hydrogen.

In applying the tone-burst modulation, high power (~10 Watts) radio frequency (RF) signal at 15 to 100 MHz was sent into EOM to generate RF sidebands on the Ti:Sapphire laser. The RF signal was amplitude modulated by a square wave at 100 kHz through a double-balanced mixer, therefore the sidebands were turned on and off at frequency of 100 kHz. After difference frequency generation, the RF sidebands were transferred to the idler beam (IR beam). This frequency modulation technique greatly improves the sensitivity of fractional detection to about 5×10^{-4}, compared to the power modulation about 1×10^{-2} using a mechanical chopper. The sensitivity of tone-burst modulation is mainly limited by the residual amplitude modulation noise and source noise.

3.1.3 Construction of mid-IR DF spectrometer

The configuration of our mid-IR DF spectrometer used in the study of $W_0(0)$ transition of solid p-H_2 is shown in Figure 3.2. The CW mid-IR DFG radiation was generated by mixing the NIR beams of a 1064 nm single frequency diode fiber laser (*Novawave* SFL-1064PM) and a tunable Ti:Sapphire ring laser (*Coherent* 899-21) in a PPLN crystal (*Covesion* DFG2-0.5-40). The Ti:Sapphire laser was pumped by a 532 nm DPSS laser (*Laser Quantum* Finesse). And by changing three sets of cavity mirrors, the Ti:Sapphire laser can be tunable in the range of 700-900 nm. By electrically tuning the thick etalon in the optical cavity, Ti:Sapphire laser can continuously scan 24 GHz (0.8 cm^{-1}) each time. And then by controlling the thin etalon and birefringent filter (BRF), we can choose the starting frequency of each scan. So the whole frequency range can be continuously tuned in this way. Detailed description can be found elsewhere.[36] The Ti:Sapphire laser was either power modulated using a mechanical

chopper at a frequency up to 6kHz or tone-burst modulated using an electro-optic modulator (EOM) (*New Focus* 4002) at 100 kHz with RF frequency in the range of 15 - 100 MHz. The absorption signal was detected by an InSb detector cooled with liquid N_2. A germanium filter was used to block the near-IR beams just in front of the InSb detector. The signals from the InSb detector were demodulated using a lock-in amplifier referenced at the square wave frequency. The analog signals from the lock-in amplifier were digitized by an ADC card and then recorded in a PC. The spectral purity of our mid-IR DF spectrometer was estimated to be several MHz, which was determined by the two master lasers. The infrared frequency was calibrated by measuring output frequencies of the Ti:Sapphire laser and the fiber laser using a wavelength meter (Burleigh WA1500) at a resolution of 0.001 cm^{-1}. The digital readout from the wavelength meter was also sent to the PC synchronously. An in-house *Labview* programme was written for data acquisition, frequency calibration and data processing.

In the routine operation, the appropriate frequency of the Ti:Sapphire laser was determined based on the output IR frequency. The suitable poling period of PPLN crystal was then chosen. Since only a small frequency range (<0.5 cm^{-1}) was needed to cover the $W_0(0)$ transition in our experiments, the corresponding PPLN temperature was optimized for the highest IR output power at the center of the coverage. With only one wavelength meter, it was used to monitor the frequency of Ti:Sapphire laser at most time. Only just before and after each scan, the wavelength meter was used to measure the frequencies of 1064 nm fiber laser for about 10 seconds each time. During the scanning process of around two minutes, the fiber laser exhibited little change in output frequency. By assuming a linear drift of output frequency for the fiber laser, a linear fitting routine was performed to extrapolate the exact output frequency of the fiber laser at any time of the scan. since the frequency of Ti:Sapphire laser during the scan was extrapolated by a polynomial fit, the corresponding infrared frequency was determined based on the subtraction of the two frequencies. The IR spectrum was then obtained by plotting the signals processed from the lock-in amplifier against the calculated infrared frequency.

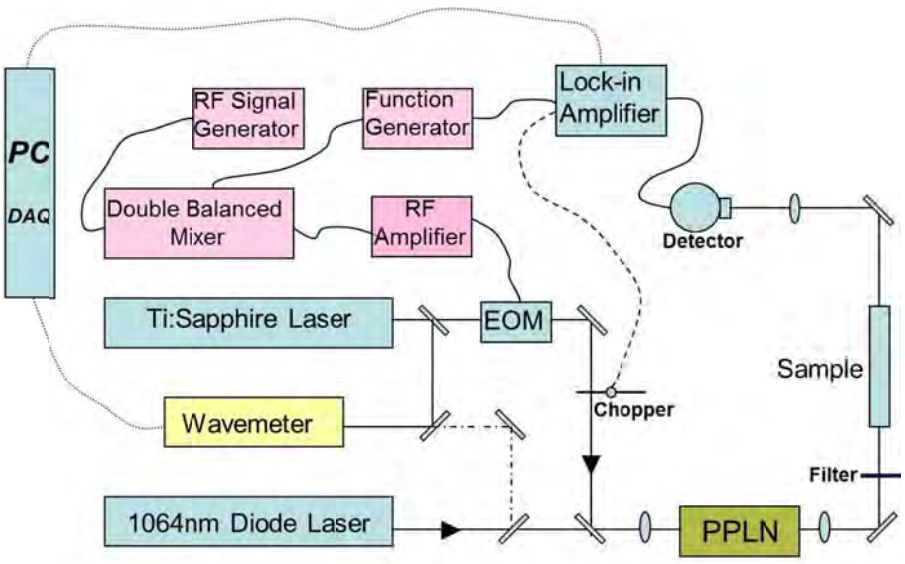

Figure 3.2 The configuration of the MIR DFG spectrometer

3.2 Near-IR diode laser spectrometer

Diode laser is the most common form of semiconductor laser, which is low priced, compact, and relatively easy to operate. However, unlike the difference frequency laser, the coverage of a laser diode is patchy—only a few wave numbers can be covered continuously even by changing modes. Fortunately for the NIR diode laser (*Newport* 2010M) in our experiment, the coverage is continuous for the $W_1(0)$ transition of solid p-H_2. The output power of NIR diode laser is about tens of mW in the 1.5 μm region. The spectral purity is about several MHz.

The construction of a NIR laser absorption spectrometer in our laboratory has been described elsewhere.[36] The schematic setup of the spectrometer with the sample system is shown in Figure 3.3. The frequency of the laser was calibrated by a wavelength meter with resolution of 0.001 cm^{-1}. An uncertainty of ~0.002 cm^{-1} was expected by comparing the measured transition of CO with the corresponding literature values. On the other hand, the relative uncertainty within a scan was on the order of 0.0005 cm^{-1}. A polarization rotator is used to change the direction of polarization of the laser beam. The laser output was either power modulated using a chopper at a frequency up to 6 kHz or frequency modulated at about 1 kHz. In frequency modulation, a sine wave $A\sin\Omega t$ from a function generator was sent into

the laser controller to periodically change the length of the laser resonator by modulating the piezoelectric driver at 1 kHz (i.e. Ω=1 kHz). As a result, the laser output frequency was shift back and forth in the range ω-ω_d to ω+ω_d. The modulation depth ω_d was called determined by the amplitude *A* of the sine wave. When ω_d is comparable to the spectral line width, a first derivative line profile will be observed using *1f* phase-sensitive detection. Other signals with different widths will not be efficiently picked up and thus the noise background will be significantly reduced. For better resolving power, *2f* phase-detection will be used to record the second derivative line profile. For $W_1(0)$ transition, the modulation depth ω_d was set at about 300 MHz calibrated by a spectrum analyzer (*Thorlab*). After passing through the sample, the laser beam was collected by an InGaAs detector and then demodulated by a lock-in amplifier. The analog signal was then store and analyzed in a PC through an in-house *Labview* programme.

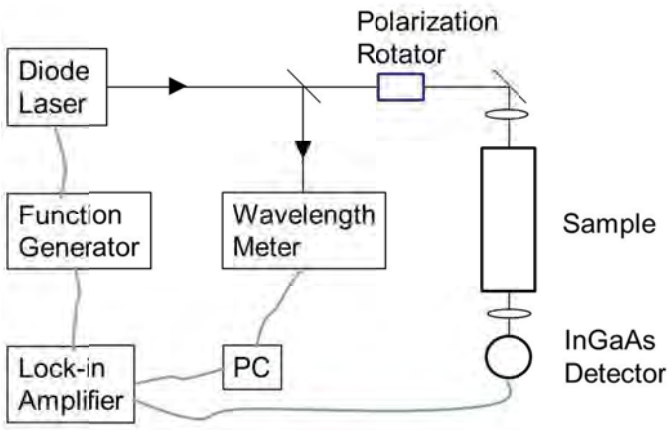

Figure 3.3 The configuration of the NIR laser spectrometer

3.3 Preparation of solid p-H_2

i. Preparation of p-H_2 gas

A gas handling system for preparation, storage and transportation of p-H_2 gas was built from scrach in our laboratory, which has been discussed in details elsewhere[36,37]. Para-enriched H_2 gas was produced using an ortho/para converter with paramagnetic Fe_2O_3 powder as the active catalyst. By controlling the conversion temperature in the range of 14 -16 K, slightly above the melting point (13.8 K) of

hydrogen, 99.95% para-enriched H_2 gas was prepared from n-H_2. The actual o-H_2 content was quantitatively determined by the experimental integrated intensity of $Q_1(1)$ transition of the solid samples. The freshly prepared p-H_2 gas was stored in a stainless steel chamber to about 40 kPa for the preparation of solid p-H_2.

ii. Cryostat and cell for crystal growth

In our solid hydrogen studies, the cryostat was a modified version of the commercial HDL-8 Dewar from *Infrared Laboratories*, as shown in Figure 3.4. There are two cryogenic vessels in this Dewar. An upper liquid nitrogen vessel was used to cool the radiation shield surrounding the liquid helium vessel and the cold work surface. The lower liquid helium vessel was used to directly cool the cold work surface. Two CaF_2 windows are installed on the optical axis to let the infrared radiation pass through. Our sample cell was mounted on an OFHC copper platform which was supported by four OFHC copper rods mounted on the cold surface so that the solid hydrogen sample was kept close to liquid helium temperature.

The cylindrical sample cell, which was made of OFHC copper, was about 30 mm in length and 15 mm in diameter. Both ends of the cell were sealed with sapphire windows using indium gaskets. A stainless steel tube about 1/16 inch O.D. was soldered on the cell wall for the inlet/outlet of H_2 gas. The temperature of the solid hydrogen sample was monitored by a cryogenic sensor installed on the cell wall. Due to the good thermal conductivity of solid hydrogen and OFHC copper, the temperature difference between the sensor and the solid H_2 sample was expected to be less than 0.5 K. The cell temperature is measured at about 5.0 K with liquid helium bath. The capacity of the helium vessel allowed continuous operation for about 24 hours before each refill. In order to vary the cell temperature, a *Nichrome* wire was wrapped around the sample cell for controlling the temperature between 5 to 12 K. By reducing the saturated vapor pressure of the helium vessel, the temperature of the He bath as well as the cell was further reduced. The lowest temperature achieved in our experiments was 3.8 K. However, the consumption of liquid helium would be much faster in both cases above. To cover a temperature range from 3.8 to 11.8 K, several refills of liquid helium was necessary.

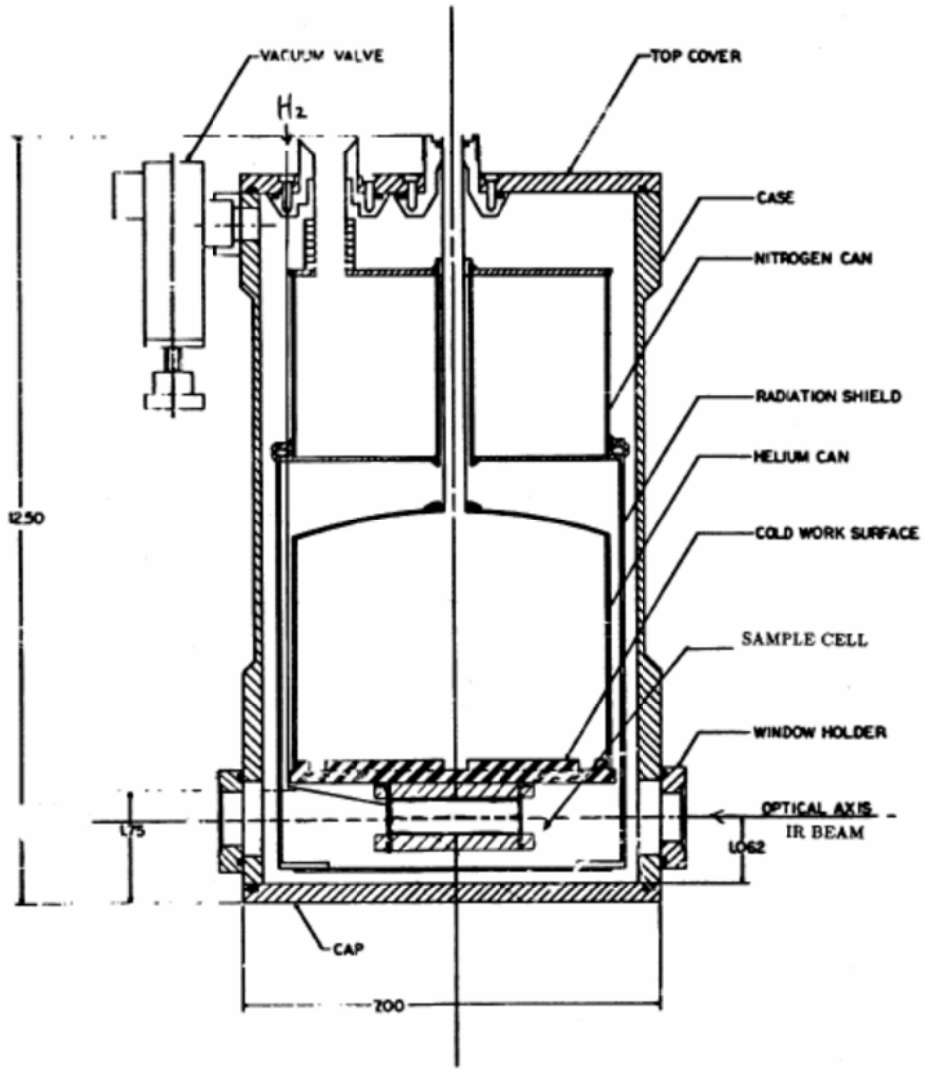

Figure 3.4 Cryostat modified from the commercial *HDL-8* Dewar.

iii. Growth of solid p-H_2 crystals

In filling the 3-cm sample cell with solid p-H_2, the main difficulty is to minimize the temperature fluctuation of the cell during the growing process. Since the volume contraction of solid H_2 is relatively large (about 13.5%) when cooling from 14 K (liquid) to 5 K (solid), the solid cracks in case that solid H_2 is prepared at melting point followed by cooling. An empirical approach to avoid this problem is to fill the cell by applying successive gas pulses so that its temperature is maintained at about 7 to 9 K through the whole growing process. After the growth is completed, the solid p-H_2 crystal is then cooled down to about 5 K. This approach is applicable because the volume change of solid H_2 is small. The samples in our experiments were prepared

following this approach as described previously.[36,37] Using this method, the sample cell was fully filled with optically transparent p-H_2 crystal in most cases.

B. Apparatus for spectroscopic study of gaseous diatomic molecules

To obtain the high resolution spectrum of transition metal containing gas molecules, some special techniques are needed due to the low abundance and short life time of target molecules in the system. In our study of transition metal containing gas molecules, laser ablation and free jet expansion techniques are used to produce diatomic transition metal molecules.[38] A high resolution Ti:Sapphire laser was used to excite the target molecules for the observation of fluorescence emission (also known as laser induced fluorescence, LIF) from excited states. By plotting the LIF signals against the excitation laser frequency, a spectrum very similar to the absorption spectrum can be obtained since absorption process occurs prior to the fluorescence emission. Nevertheless, the LIF spectrum exhibits different relative transition intensities compared to absorption spectrum. Similar to other zero-background techniques, LIF spectroscopy is very sensitive and therefore suited for the detection of species at low concentration.

3.4 Production of the metal-containing molecules

Gas phase transition metal-containing molecules can be commonly produced by reacting metal vapor with appropriate precursor gas. Laser ablation of metal rod has been mostly used to produce metal vapor without reaching high boiling temperature. The mechanisms of laser ablation are very complicated and more than one mechanism may be simultaneously involved to generate the metal vapor. These mechanisms can generally be divided into photochemical, mechanical and thermal processes with the dominant process determined by the frequency of ablation laser. When a pulse laser with power of up to tens of mJ in each pulse is focused on a spot of the surface of a metal, the temperature of the surface area near the spot will increases rapidly. And when the thermal energy is high enough, the metal atoms can be vaporized out from the bulk metal for reacting with the reagent gas.

In order to minimize further reactions of the freshly formed reactive metal

compounds, the reaction gas mixture are usually supersonically expanded into a high vacuum chamber for the detection. Supersonic free jet expansion has proved to be a simple and efficient approach to reduce the gas temperature and increase the mean free path.[29] As seen in Figure 3.5, a free jet is formed when gas expands from a high pressure region to the high vacuum region through a small nozzle. When the diameter d of the nozzle is much larger than the mean free path μ_0, the orifice will convert the random motions of molecules into mass flow in the direction normal to the nozzle. As a result, the molecular motion has a preferential direction instead of random in all directions. This effect can minimize the Doppler broadening in spectral line width by using a probe beam orthogonal to the preferential direction. Furthermore, the adiabatic cooling is very efficient in the rotational population that helps to reduce spectral congestion for recording high resolution spectrum.

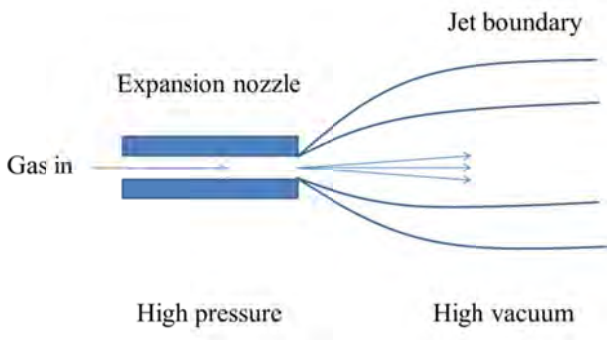

Figure 3.5 Schematic diagram of free jet expansion through a nozzle.

The ablation laser used in our experiments was a pulse Nd:YAG laser (*Continuum* Sitellite S) with emission at 1064 nm and repetition rate of 10 Hz. The pulse width was ~7 ns and a total power of about 20 mJ. To avoid overheating the metal, the laser beam is defocused to a spot size of 2 mm on the metal surface. Figure 3.6 shows the schematic diagram of the laser ablation module. Metal rods of diameters up to 8 mm were mounted on a home-made metal holder next to a solenoid valve controlling the reagent gas flow. The valve and the holder were separated by a gas passage channel of 2 mm in diameter and 20 mm in length. A hole of 2 mm in diameter was opened to allow the ablation laser beam propagating perpendicular to the gas flow to strike on the surface of the metal rod. In addition, the mount of the

metal rod was connected to an electric motor to rotate the metal surface for even exposure to the ablation laser in the course of the experiments. As a result, good stability in the production of metal vapor was achieved. In order to remove the soot and reduce the noise of ablation, the surface of metal rod was cleaned after several hours of laser ablation operation.

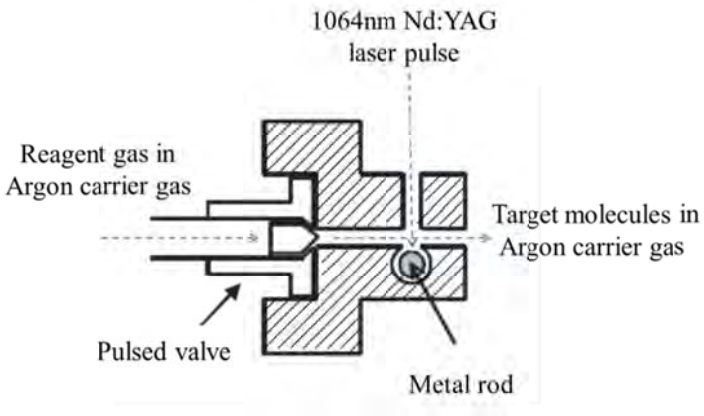

Figure 3.6 Schematic diagram of laser ablation of transition metal.

The reagent gas used in our experiments was mainly Ar buffer gas pre-mixed with low concentration of precursor gas at a total pressure up to about 10 atm. The gas mixture was expanded to a vacuum chamber about 10^{-4} Torr through an orifice with diameter of 2 mm. the solenoid valve was used to control the reagent gas pulses synchronized with the ablation laser pulses at a frequency of 10 Hz with a flow time of about 300 μs and a time delay depending on the dimension of the gas channel. Comparing to continuous expansion, pulse expansion allows smaller pumping capacity, lower consumption of reagent gas, and less condensation, especially in the case of corrosive regent gas, to achieve the same rotational cooling. Under our experimental conditions, both translational and rotational temperatures were cooled down to about 100 K to give line width of about 0.02 - 0.03 cm^{-1} and a rotational population of about J up to 20.

3.5 High resolution laser induced fluorescence (LIF) spectrometer

In our study of metal-containing diatomic molecules in the gas phase, a high resolution laser induced fluorescence spectrometer was coupled with a gas handling

system and a vacuum chamber to record the rovibronic spectra of the species of interest. The laser induced fluorescence spectrometer mainly contains a high resolution excitation laser source, a frequency calibration device, a fluorescence detection system and a data acquisition system. The complete experimental setup of the system is shown in Figure 3.7.

As shown in Figure 3.7, the excitation laser source was a high resolution tunable Ti:Sapphire ring Laser (*Coherent* 899-21) optically pumped by a DPSS laser (*Laser Quantum* Finesse) at 532 nm. With three sets of cavity mirrors, the Ti:Sapphire laser emitted light in the range from10000 to 14000 cm^{-1} at a power of several hundreds of mW with a spectral purity of about 500 kHz(RMS). By electrically tuning the thick etalon in the optically cavity, the Ti:Sapphire laser could continuously cover 24 GHz (0.8 cm^{-1}) in each scan. The starting frequency of each scan was varied by controlling the thin etalon and birefringent filter (BRF). The complete frequency range was continuously covered in this fashion. The accurate frequency of the laser was calibrated by a commercial wavelength meter with a resolution of 0.001 cm^{-1}. By comparing the frequency measurement of some known transitions, we found that the absolute frequency for our system was better than 0.003 cm^{-1}.

The excitation laser beam was sent to the gas chamber perpendicular to the expansion jet of target molecules. The fluorescence emitted by molecules after excitation was collected by a lens system orthogonal to both the directions of excitation laser and the gas jet. The fluorescence was sent into a monochronmater and eventually detected by a photomultiplier tube (PMT) sensitive in the NIR region. The monochronmater was served as an optical filter for recording LIF spectrum and also used for obtaining the wavelength resolved fluorescence (WRF) spectrum. The fluorescence signal detected by PMT is then digitized by a fast oscilloscope. An in-house programme was written for synchronous acquisition of data from both oscilloscope and wavelength meter. By plotting the fluorescence signal vs the frequency read by wavelength meter, a high resolution LIF spectrum was recorded.

In the initial search of the target molecules, the Ti:Sapphire laser was manually scanned over a broad spectral range to search LIF signals. By removing the intra-cavity etalon assemblies (ICA) and manually scanning the BRF, a spectral resolution at about 2 GHz was achieved for each scan of about 50 cm^{-1} at a speed of

about 0.2 cm^{-1}/s. After the identification of observed vibronic bands, high resolution rotationally resolved LIF spectra were recorded with the ICA installed.

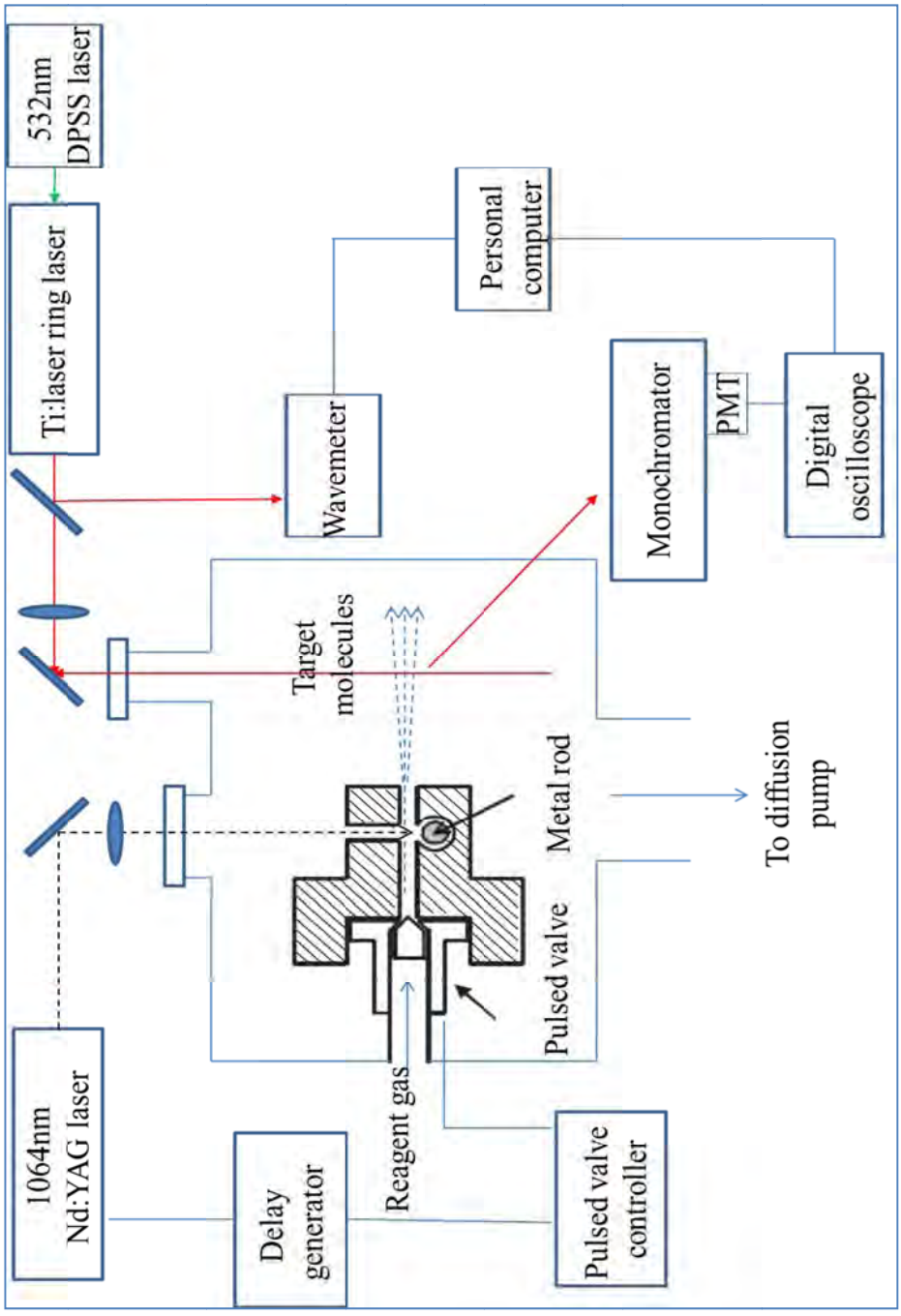

Figure 3.7 Schematic diagram of high resolution laser induced fluorescence spectrometer.

Chapter 4 High resolution infrared Laser spectrum of solid parahydrogen

4.1 Introduction

Solid hydrogen is the simplest yet interesting molecular crystal of all, and it is known as a quantum crystal. Solid hydrogen has two crystal structures, namely, face-centered cubic (fcc) and hexagonal close-paced (hcp).[8] When hydrogen molecules is condensed from liquid to solid, hcp structure is usually formed. The molecules in the solid are held together mainly by long range isotropic dispersion interactions. The combination of small molecular mass, small molecular size (the internuclear distance of H_2 is 0.741 Å), large intermolecular separation (the nearest neighbor distance R_0 is 3.793 Å), and the weak intermolecular interaction give rise to the remarkable properties of solid hydrogen.

Due to small molecular size and large intermolecular separations, H_2 molecules are only slightly perturbed in the solid state to have nearly free rotation and vibration even at very low temperature, as indicated by numerous spectroscopic studies. On the other hand, the small molecular mass and weak intermolecular interactions give rise to the exceedingly large amplitude of zero-point lattice vibration. Solid hydrogen can therefore be considered an assembly of molecules translationally localized with a relative large lattice motion, but still free to rotate and vibrate quite independently. Rotational diffusion is another interesting quantum phenomenon due to resonance exchange of ortho/para hydrogen which is responsible for the equilibrium of spatial distribution of ortho and para hydrogen at cryogenic temperature. More detailed properties of solid hydrogen have been reviewed by Silvera[8] and van Kranendonk[7].

The rotational and/or vibrational transitions in pure solid hydrogen are ascribed to many-body radiative interactions. The multipole moments of each hydrogen molecules induces coherent dipole moments in the surrounding molecules and these dipole moments cause the absorption of photon by the central molecule through

many-body interaction. Since the observation of very sharp pure rotational transition $W_0(0)$,[11] many infrared and Raman studies of solid hydrogen have been carried out using high resolution laser spectroscopy.[12,39,40] The high resolution spectra provide valuable detailed information on intermolecular interactions in the crystal. These properties can also be calculated from the first principle with high precision.[41]

Solid parahydrogen has also been extensively used as a solid matrix for studying the rovibrational dynamics of small dopant molecules in the condensed phase. The *J*= 0 p-H_2 molecules are spherically symmetric in charge distribution without multipole moments, which gives rise to a nearly isotropic crystal environment. In addition, owing to its quantum nature and large intermolecular distance, solid parahydrogen provides ample space for guest molecules to have rotation and vibration. Because of the weak interactions between guest molecules and surrounding host molecules, the lifetimes of rovibrational excited states of the guest molecule in solid parahydrogen are prolonged to give rise to the sharpness of the spectral transitions observed in solid parahydrogen.[42-45] Moreover, crystal defects around the guest molecules are expected to automatically repair themselves quickly. As a consequence, the rovibrational motion of guest molecules as well as the host-guest interactions is more observable in the spectra of solid hydrogen. There observations serve to provide rigorous tests for theoretical model and quantitative prediction.

One of the most remarkable phenomena in the rovibrational spectra of solid hydrogen is the exceptionally narrow line width in samples enriched with parahydrogen. The narrow line width allows study of detailed spectral features due to intermolecular interactions in the solid state such as crystal field splitting.[11] On the other hand, the temperature dependence of spectral frequency and line shape provide information about the mechanism of exciton relaxation.[12,15,46,47] In 1986, Skinner *et al* proposed two theoretical models to describe relaxation of two-level system in the bulk crystal.[48] One is the Debye model, in which the phase relaxation is caused by acoustic phonon scattering. The temperature dependence of spectral line position and line width are derived to follow the power functions of T^4 and T^7 respectively. The other one is called the pseudolocal modes model, in which the relaxation is caused through a low frequency local vibrational mode around the impurity of interest. In this model, the temperature dependence of line width is

described by an Arrhenius type function of exp(-hν/kT). The narrow linewidth of spectral transitions in solid parahydrogen provide an excellent system for line width and line profile studies that are essential in understanding the relaxation mechanism in the solid state. In studying the electric field induced Condon $Q_1(0)$ transition in 1994,[15] Oka and coworkers observed the temperature dependence of line width. They found that it appeared to have a Gaussian line shape at low temperature but became more Lorentzian at temperature close to triple point. These observations suggested that the line widths observed at low temperature might be due to inhomogeneous broadening. The transition frequency was observed to have a blue shift with temperature dependence close to T^4, which was interpreted by the thermal expansion of the volume of the crystal. Recently, Kuroda *et al* reported the high resolution coherent Raman spectra of $Q_1(0)$ transition in the temperature range of 4 to 13 K.[12] The transition was observed to have a Lorentzian line shape with a width (HWHM) as narrow as 5 MHz,[12] indicating a homogeneous broadening throughout the temperature range. Based on the observed T^4 and T^7 temperature dependences, respectively, for Raman shift and line width, the relaxation was explained by the Debye model, i.e. due to the interaction between vibron and thermal acoustic phonons.

The line profile of dopant molecules in solid parahydrogen matrix has also been investigated. The vibrational relaxation of v_3 and v_4 mode of CD_4 molecule in solid parahydrogen has been investigated by Momose *et al*.[47] They observed a blue shift for both v_3 and v_4 transitions, and the temperature dependence of their line widths are fitted by a T^4 power function. Recently, Kanamori and coworkers have studied the spectral line profile of rovibrational transitions of CO embedded in p-H_2 crystal.[46] Four transitions were observed, which are $R(0)^{//}$, $R(0)^{\perp}$, $P(1)^{//}$ and $P(1)^{\perp}$ in the fundamental band. When increasing the temperature, both red shifts and blue shifts were seen in just one vibrational band. The line width is fitted well by Voigt function. The Gaussian component shows no temperature dependence. While the temperature dependence of Lorentzian component can be fitted by an exponential function of an Arrhenius equation, which is well explained by the pseudolocal modes model. The fitted activation energy corresponds to the fundamental frequency of the local mode for CO vibrating within the cage of neighboring H_2 molecules.

In this chapter, our study of the line profiles and transition frequencies of rovibrational $W_1(0)$ and pure rotational $W_0(0)$ transitions of solid p-H_2 crystal are reported. The W transitions ($\Delta J=6$) are due to dipole moments coherently induced by tetrahexacontapole (64^{th} pole) of H_2 molecules in the crystal. Both $W_0(0)$ and $W_1(0)$ have been observed with a typical line width on the order of 0.001 cm^{-1} (FWHM), that has been qualitatively ascribed to the slow relaxation of the J=6 localized rotons. It will be interesting to examine the temperature dependence of transition frequencies and line profiles for both transitions, which will no doubt shed some light on the understanding of interactions and relaxation process in the solid hydrogen crystal.

4.2 Theoretical considerations

The W transitions ($\Delta J=6$) of H_2 in the gas phase are dipole forbidden. In the solid phase, however, intermolecular interactions give rise to dipole moments coherently induced by tetrahexacontapole (64^{th} pole) between molecules. As a result of the anisotropic crystal environment, rotational states of the same J manifold with different projection of angular momentum will have different energy. The triplet structure of both $W_0(0)$[11] and $W_1(0)$[13] transitions were observed in 1991 and 2009 respectively using high resolution laser spectroscopy. The observed crystal field splitting has been interpreted using a localized exciton model that gives an excellent agreement with theoretical calculations based on *ab initio* intermolecular potential. The detailed theoretical background will be discussed below.

As discussed before, we assume the p-H_2 crystals to have hcp structure. If a p-H_2 molecule is excited to the J=6 state surrounded by J=0 molecules, this central molecule will be exposed to a D_{3h} crystal field. Since the energy on excited H_2 molecules can only dissipated to the surrounding H_2 molecules through resonance hopping that requires the extremely weak tetrahexacontapole-tetrahexacontapole interactions, the excitation energy is expected to localized on the central molecules for extended time. Similar to the case of v=1 excitation, a localized exciton is therefore formed. Applying the group theory of matrix isolated molecules

developed by Miller and Decius[49], one can deduce that only the sublevels with |M|=2, 3 and 4 in the J=6 manifold are allowed for J=6←0 transition. When the light polarization is parallel to the crystal c axis (C_3 rotation axis), only |M|=3 transition is allowed. And when the light polarization is perpendicular to the c axis, |M|=2 and 4 transitions are expected.

The relative transition intensity of each M component can be calculated following Balasubramanian's formulas.[50] In the crystal frame, by summing of the tetrahexacontapole induced dipoles in the surrounding molecules, the v^{th} (v=0, ±1) component of this dipole moment is

$$\mu_v = 4\pi\sqrt{\frac{7}{15}}\frac{\alpha_{00}Q^{(6)}}{R_0^8}\sum_m C(617;m,v,m+v)Y_{6m}^*(\Omega)S_{7,m-v}$$

where $\alpha_{00} = \langle v=0, J=0|\alpha|v=0, J=0\rangle$ is the isotropic polarizability of the J=0 molecules in the ground state, $Q^{(6)} = \langle v=0 \text{ or } 1, J=6|Q^{(6)}|v=0, J=0\rangle$ is the transition 64-pole moment, and

$$S_{7,m+v} = \sum_{i=2}^{N}(\frac{R_0}{R_i})^8 Y_{7,m-v}(\Omega)$$

is the dimensionless lattice sum. Then it is seen that μ_0 gives rise to the transition with |M|=3 whereas $\mu_{\pm1}$ give rise to transitions with |M|=2 or 4. From the derived induced dipole, the relative intensity of the three components can be calculated for depolarized light as below:

I(|M|=2): I(|M|=3): I(|M|=4)=45:40:6.

The anisotropic crystal field splitting for a localized exciton in J=6 state can be determined using van Kranendonk's expression[7],

$$\begin{aligned} V(\Omega) &= \sum_{i=2}^{N}\sum_{l=2,4}A_{l00}(R)\sum_{m=-l}^{l}C_{lm}(\Omega)C_{l\bar{m}}(\Omega_i) \\ &= \sum_{l=2,4}\sum_{i=2}^{N}B_l(R)C_{l0}(\Omega_i)C_{l0}(\Omega) \\ &= \sum_{l=2,4}\varepsilon_{l0}C_{l0}(\Omega) \end{aligned}$$

where Ω and Ω_i are the orientations of the excited molecule and position vector $\mathbf{R_i}$ of the i^{th} molecule in the crystal frame. So the Hamiltonian of the transition frequency can then be expressed by

$$\mathrm{H} = \nu_0 + \varepsilon_{20}\mathrm{C}_{20}(\Omega) + \varepsilon_{40}\mathrm{C}_{40}(\Omega)$$

with three experimentally determined parameters. Here the angle independent transition frequency ν_0 is included and only the two lowest anisotropic terms are considered. Based on the *ab initio* calculations by Mulder *et al*,[41] the crystal field coupling constants ε_{20} and ε_{40} values can be calculated theoretically.

$$\varepsilon_{2c} = \sum_{n=6,8,10} \frac{b_n}{R_0^n} \sum_k {}'(\frac{R_0}{R_k})^n C_{20}(\Omega_k)$$

$$\varepsilon_{4c} = \sum_{n=8,10} \frac{c_n}{R_0^n} \sum_k {}'(\frac{R_0}{R_k})^n C_{40}(\Omega_k)$$

The anisotropic interaction coefficients b_n and c_n are obtained from Mulder et al. The dispersion interaction (R^{-6} term) is the main contribution to ε_{2c}. Summering the effects for 20 shells, ε_{2c} is determined to be -0.0022 cm^{-1}. Similarly, ε_{4c} is determined to be -0.1124 cm^{-1} after lattice sum of 20 shells. In contrast to the case of ε_{2c}, both dispersion and induction contribute to the ε_{4c} term, with induction being the dominant effect. The ε_{2c} term is considerably small because the lattice sum for the first two shells accidentally vanishes in perfect D_{3h} symmetry. However, the breakdown of D_{3h} symmetry often occurs due to the imperfection of solid p-H_2 crystal in experiments. The deviation from D_{3h} symmetry is expected to increase the value of experimentally ε_{2c} value that was observed by an order of magnitude greater in most experiments. Based on the *ab initial* calculations of quadrupole moments of H_2 in the v=0 and v=1 states, it is estimated that ε_{4c} has an increase of 10% upon the vibrational excitation.

4.3 Results and analysis

In all of the measurements, samples of 3 cm long solid prarhydrogen (99.95% p-H_2) crystals were used. Both the pure rotational $W_0(0)$ and rovirational $W_1(0)$ transitions were studied. The quality of the crystals was examined using an FTIR spectrometer at 0.1 cm^{-1} resolution. Both $W_0(0)$ and $W_1(0)$ appeared as a single peak with an instrument-limited line width. Three samples of solid p-H_2 were used in our measurements. For each sample the fine structures of both transitions were first

measured using our laser spectrometers. The temperature dependence of the transition frequency, line width and line shape were then studied for each transition. These results are discussed below.

A. Transition frequency and appearance at 5.0 K

The spectrum of $W_1(0)$ of our sample at 5.0 K under chopper modulation and *2f* frequency modulation with both horizontal and vertical polarization of light are shown in Figure 4.1. Trace (a) shows the chopper modulated spectrum at parallel polarization. Only one peak was observed at 6441.7372 cm^{-1}. The fraction absorption ($\Delta I/I$) is about 5% and line width is about 0.015 cm^{-1}. Unresolved structure was observed in Trace (b) using perpendicular polarization. Trace (c) and (d) show the spectrum using 2f frequency modulation with improve effective resolution so that the fine structure was completely resolved. In trace (d), the triplet structure is clearly shown using perpendicular polarization. The three peaks are observed at 6441.7223, 6441.7372 and 6441.7484 cm^{-1} respectively. A typical line width of about 100 MHz is observed in the *2f* modulation scheme. It should be noted that the profile shown under frequency modulation does not represent the true line shape but resemble of the 2^{nd} derivatives of the spectral transition observed in amplitude modulation according to the *2f* demodulation scheme.

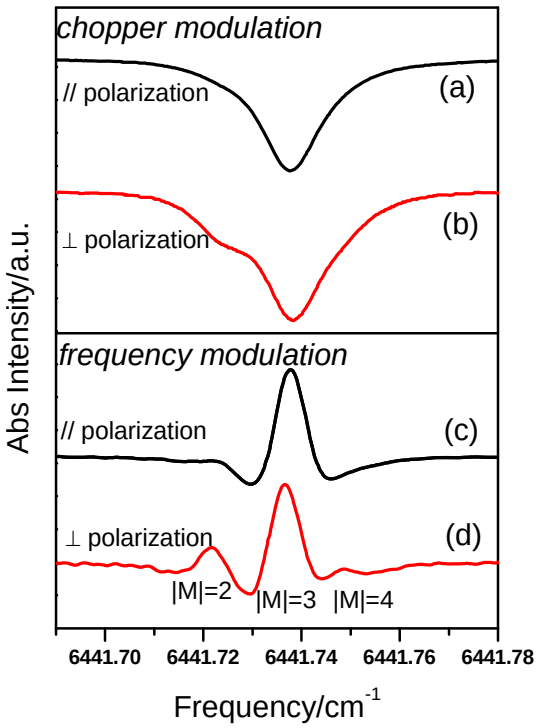

Figure 4.1 Spectrum of $W_1(0)$ transition under chopper modulation and frequency modulation with both parallel and perpendicular polarization.

The triplet structure in trace (d) were assigned to the transitions from J=0 to |M|=2, 3 and 4 sublevels in the J=6 manifold according to the polarization dependence and relative intensity as discussed in the theoretical background. The transition frequency is expressed by :

$$\mathrm{H} = \nu_0 + \varepsilon_{20}\mathrm{C}_{20}(\Omega) + \varepsilon_{40}\mathrm{C}_{40}(\Omega).$$

Based on the assignments, the three parameters ν_0, ε_{2c} and ε_{4c} were determined by least-squares fitting. The measured transition frequencies for the three samples of solid p-H_2 were shown in

Table 4.1. By taking three samples of the observed frequencies of the triplet $W_1(0)$ transition, the three parameters derived from least-squares fitting were ν_0 = 6441.7298(26) cm^{-1}, ε_{2c} = -0.0248(148) cm^{-1} and ε_{4c} = -0.1067(168) cm^{-1} respectively, consistent with the previous results by Song[36].

The fitted value of ε_{2c} is about an order of magnitude greater than the

theoretical value, which is expected. Since the lattice sum from the first two layers accidentally vanishes in D_{3h} symmetry, so ε_{2c} is very sensitive to the symmetry of the crystals. Therefore, the deviation indicates that the crystal may not be perfect D_{3h} symmetry. On the other hand, the value of ε_{4c}, which is not sensitive to the imperfection of crystal, is in good agreement with the theoretical value.

Table 4.1 Observed frequencies of $W_1(0)$ transition of three samples at 5.0 K. The results of least-squares fitting are also listed with the corresponding uncertainty in parenthesis.

Sample	Assignment	Observed frequency (cm^{-1})
I	|M|=2	6441.7223
	|M|=3	6441.7372
	|M|=4	6441.7484
II	|M|=2	6441.7241
	|M|=3	6441.7387
	|M|=4	6441.7497
III	|M|=2	6441.7230
	|M|=3	6441.7375
	|M|=4	6441.7487
Fitted parameters (cm^{-1})		
ν_0		6441.7298(26)
ε_{2c}		-0.0248(148)
ε_{4c}		-0.1067(168)
Variance		0.0008

As shown in Figure 4.2, the $W_0(0)$ transition exhibited a similar pattern as the $W_1(0)$ transition. The transition was therefore expected to be split into M components by the crystal field interactions similar to the $W_1(0)$ transition. The observed transition frequencies shown in Table 4.2 were fitted using the same Hamiltonian to obtain the three parameters ν_0 = 2410.5332(17) cm^{-1}, ε_{2c} = -0.0244(97) cm^{-1} and ε_{4c} = -0.1031(110) cm^{-1}, respectively. These results are in excellent agreement with the previous preliminary studies.[11]

It is seen that the ε_{4c} value of $W_1(0)$ transition is slightly larger than that of $W_0(0)$

transition. This is consistent with the fact that there is an increase of about 10% of the quadrupole moment of the J=6 molecule in the v=1 excited state compared to that in the v=0 state. This agreement further confirms the localization of J=6 roton in both $W_0(0)$ and $W_1(0)$ transitions.

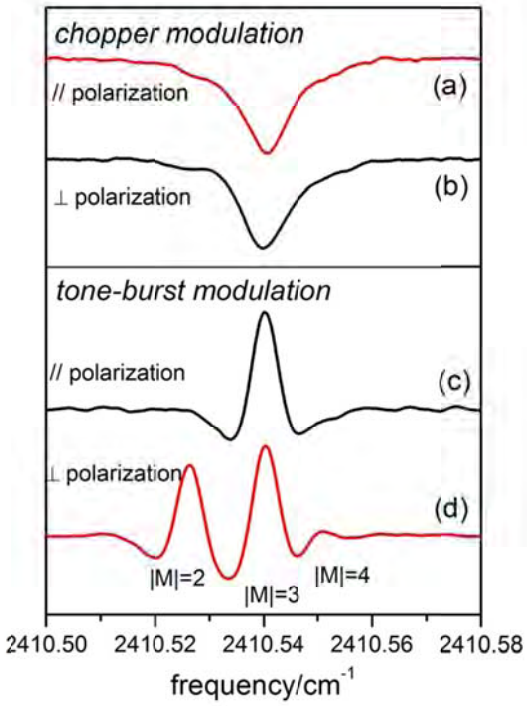

Figure 4.2 Spectrum of $W_0(0)$ transition under chopper modulation and tone-burst modulation with both parallel and perpendicular polarization.

Table 4.2 Observed frequencies of $W_0(0)$ transition of three samples at 5.0 K. The results of least-squares fitting are also listed with the corresponding uncertainty in parenthesis.

Sample	Assignment	Observed frequency (cm^{-1})
I	|M|=2	2410.5257
	|M|=3	2410.5398
	|M|=4	2410.5504
II	|M|=2	2410.5256
	|M|=3	2410.5397
	|M|=4	2410.5502
III	|M|=2	2410.5260
	|M|=3	2410.5403
	|M|=4	2410.5517
Fitted parameters (cm^{-1})		
ν_0		2410.5322(17)
ε_{2c}		-0.0244(97)
ε_{4c}		-0.1031(110)
Variance		0.0005

B. Line shape of W transitions at 5.0 K

We also studied the line profiles of both W transitions. As discussed above, chopper modulation with the vertically polarized light gives M=±3←0 component with little contribution from the other two components. It is therefore an ideal condition to study the line profiles for understanding the relaxation mechanism. As shown in Figure 4.3, a Lorentzian fit of trace (a) in Figure 4.1 gives an excellent agreement with a fitted width of 0.0155 cm^{-1} (FWHM). This observation indicates that the observed line width at 5.0 K was dominated by homogeneous broadening mechanism.

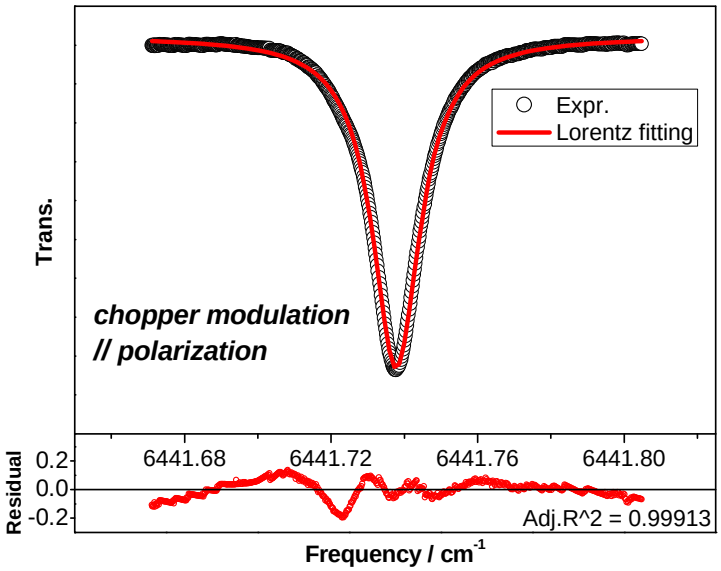

Figure 4.3 The |M|=3←0 peak of $W_1(0)$ transition fitted by Lorentzian profile.

!

The line profile of $W_0(0)$ transition was fitted similarly. The profile was also fitted to a Lorentzian shape with a width of 0.0101 cm^{-1}, as shown in Figure 4.4. Because of the lower signal-to-noise ratio, the fitted uncertainty of $W_0(0)$ transition was higher compared to the case of $W_1(0)$ transition. For a more accurate fitting result, it is necessary to significantly improve the S/N in future studies.

Based on the line profile fits, both $W_1(0)$ and $W_0(0)$ transitions exhibit Lorentzian line shape at 5.0 K indicating homogeneous broadening mechanism for both transitions. As discussed below, throughout the temperature range of our measurements, both lines remained the Lorentzian profiles, indicating homogeneous relaxation mechanism of localized excitons from 3.8 – 11.8 K.

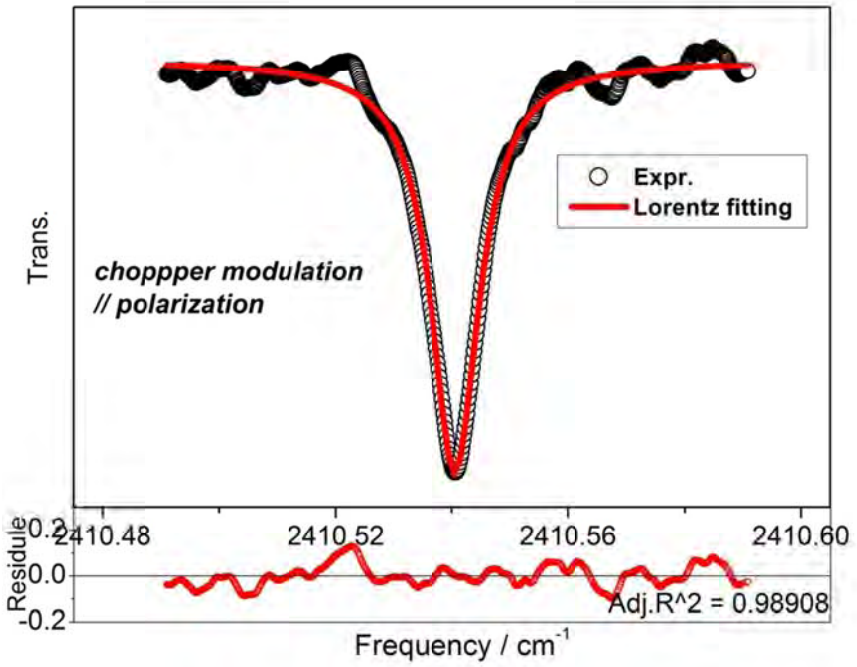

Figure 4.4 The |M|=3←0 peak of $W_0(0)$ transition fitted by Lorentzian profile.

C. Temperature dependence of line profiles

The line profiles of both W transitions at 5.0 K exhibited Lorentzian shapes, indicating homogeneous broadening mechanism. In order to investigate if the relaxation mechanism varies with temperature, we studied the line profiles of the |M|=3←0 line for both W transitions at different temperatures. It was found that the profiles remained Lorentzian in the temperature range 3.8 – 11.8 K in both cases. This observation suggested that observed line shapes and line widths were due to homogeneous relaxation mechanism.

D. Temperature dependence of crystal field splitting

The temperature dependence of the transition frequencies of both $W_1(0)$ and $W_0(0)$ transitions were studied in the temperature range of 3.8 -11.8 K. It was found that the triplet patterns of both transitions shifted to higher frequency upon increasing temperature. On the other hand, the relative position of the three M components remained essentially unchanged. Table 4.3 and Table 4.4 list the transition frequencies at different temperature for the $W_1(0)$ and $W_0(0)$ transitions,

respectively. In order to examine the temperature effect on crystal field splitting, the differences $\Delta\nu_1 = \nu(M=3) - \nu(M=2)$ and $\Delta\nu_2 = \nu(M=4) - \nu(M=3)$ against temperature are plotted in Figure 4.5. It is seen that the difference is well within the experimental uncertainty. It is therefore expected that temperature causes the same shift to all M components. This observation suggested not only that the frequency shift is due to isotropic interactions but also the shift is not related to the change of intermolecular separation due to increasing temperature. To investigate the temperature shift of the transition, we plotted the transitions frequencies of the |M|=3←0 transition at different temperature as shown in Figure 4.6 and Figure 4.7. According to the Debye model, the observed frequencies shift should have T^4 dependence for phonon scattering relaxation. By fitting the data using the polynomial expression

$$\nu(T)=A_0+A_4T^4,$$

we found that A_0 = 6441.7353(3) cm^{-1} and A_4 = 3.23(4)$\times10^{-6}$ $cm^{-1}K^{-4}$, respectively, with a correlation of 0.9974 for the $W_1(0)$ transition. By fitting the temperature dependence of ν_0 in to the expression:

$$\nu_0(T)=B_0+B_4T^4,$$

we obtain B_0 = 6441.7269(3) cm^{-1} and B_4 = 3.07(8) $\times10^{-6}$ $cm^{-1}K^{-4}$, respectively, with a correlation of 0.992. Both A4 and B4 with in the error of measurements indicating the temperature shift is due to isotropic effect with little contribution from anisotropic interactions, consistent with the results shown in Figure 4.5.

Table 4.3 The transition frequencies at different temperatures for $W_1(0)$ transition.

	Frequency/cm^{-1}		
T/K	|M|=2←0	|M|=3←0	|M|=4←0
3.8	6441.7219	6441.7370	6441.7481
4.0	6441.7219	6441.7372	6441.7482
4.5	6441.7224	6441.7370	6441.7476
5.0	6441.7232	6441.7378	6441.7489
5.5	6441.7233	6441.7384	6441.7494
6.0	6441.7248	6441.7395	6441.7511
6.5	6441.7260	6441.7403	6441.7514

7.0	6441.7284	6441.7429	6441.7537
7.5	6441.7304	6441.7449	6441.7561
8.0	6441.7331	6441.7479	6441.7593
8.5	6441.7364	6441.7511	6441.7623
9.0	6441.7403	6441.7554	6441.7667
9.5	6441.7465	6441.7616	6441.7725

Table 4.4 The transition frequencies at different temperatures for $W_0(0)$ transition.

	Frequency/cm^{-1}		
T/K	|M|=2←0	|M|=3←0	|M|=4←0
3.8	2410.5251	2410.5392	2410.5500
4.0	2410.5252	2410.5393	2410.5502
4.5	2410.5255	2410.5396	2410.5503
5.0	2410.5258	2410.5399	2410.5508
5.5	2410.5263	2410.5407	2410.551
6.0	2410.5267	2410.5409	2410.5513
6.5	2410.5272	2410.5414	2410.5520
7.0	2410.5276	2410.5419	2410.5526
7.5	2410.5281	2410.5425	2410.5529
8.0	2410.5291	2410.5434	2410.5536
8.5	2410.5298	2410.5441	2410.5545
9.0	2410.5312	2410.5455	2410.5553
9.5	2410.5329	2410.5476	2410.5575
10.0	2410.5360	2410.5498	2410.5598
10.5	2410.5381	2410.5518	2410.5621

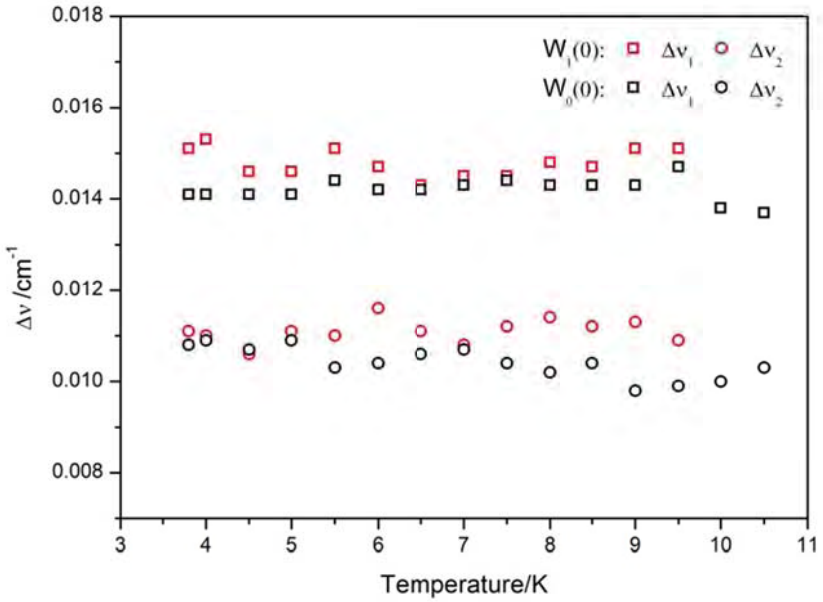

Figure 4.5 Temperature dependencies of the frequency differences $\Delta\nu_1$ = ν(M=3) - ν(M=2) and $\Delta\nu_2$ = ν(M=4) - ν(M=3) for $W_1(0)$ and $W_0(0)$ transitions.

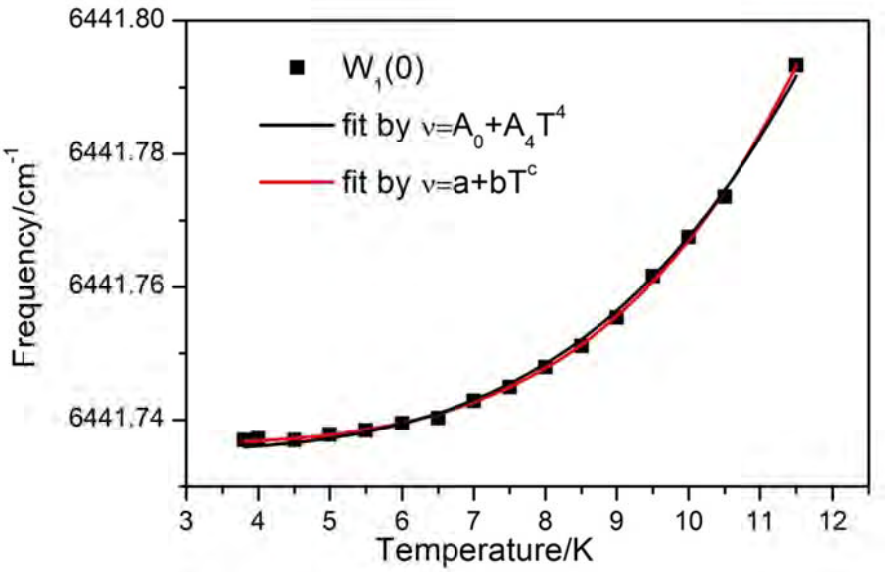

Figure 4.6 Temperature dependence of transition frequency of the |M|=3←0 $W_1(0)$ transition.

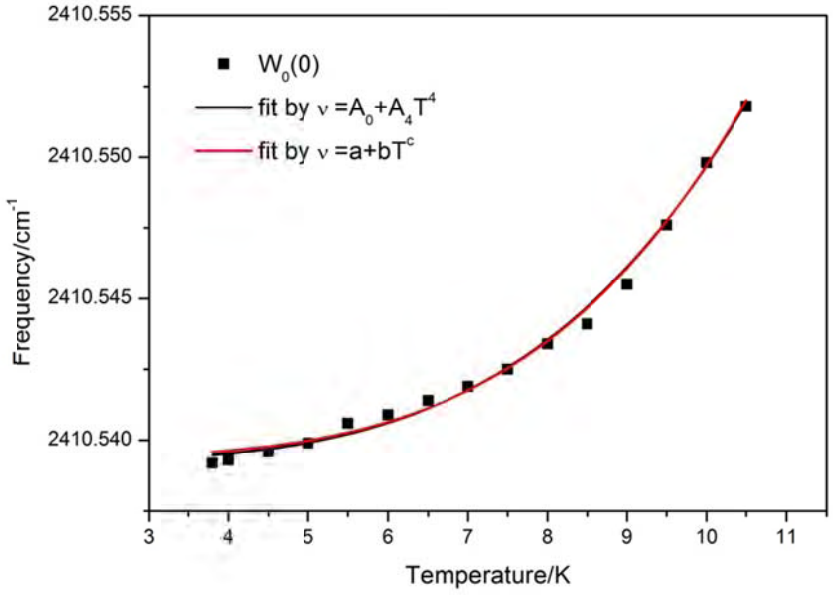

Figure 4.7 Temperature dependence of transition frequency of the |M|=3←0 $W_0(0)$ transition.

It should be noted that a lightly better fitting correlation (0.9993) was obtained by varying the power of temperature. In this case, a temperature dependence of $T^{4.41(7)}$ was obtained with A_0 = 6441.7363 cm^{-1} and A_4 = 1.20(20)×10^{-6} $cm^{-1}K^{-4.41}$, respectively. By fitting ν_0 similarly we found a $T^{3.44(26)}$ dependence. The difference in the power of T in both fits implies the anisotropic effect also contributes to the overall temperature dependence of transition frequency. This implication is, however, in contrary to the constant crystal file coupling constants observed at different temperature. We therefore believe that the genuine temperature dependence is T^4, as predicted in the Debye model. The deviation from T^4 power obtained in the fitting may arise due to moderate signal to noise in the experiments and the great difference between A_0 and A_4.

Since both $W_1(0)$ and $W_0(0)$ transitions exhibited Lorentzian profiles in the temperature range of the experiments, we expect that the relaxation mechanism of $W_0(0)$ transition is the same as the $W_1(0)$ transition and the same temperature dependence of the transition frequency for the $W_0(0)$ transition. However, in the temperature range of experiments, the $W_0(0)$ transition exhibited a smaller

frequency shift at ~0.02 cm^{-1} compared to ~0.07 cm^{-1} for the $W_1(0)$ transition. Like the case of $W_1(0)$ transition, the crystal field splitting appeared to remain unchanged with the temperature as shown in Figure 4. The temperature dependence of the $|M|=3\leftarrow 0$ of the $W_0(0)$ transition frequency is plotted in Figure4. It was fitted to the expression $\nu(T)=A_0+A_4T^4$ as before to obtain A_0 = 2410.5393(1) cm^{-1} and A_4 = $1.04(2)\times10^{-6}$ $cm^{-1}K^{-4}$, with a fitting correlation of 0.9964. It should be noted that the lower signal-to-noise ratio of the transition gave rise to greater errors in the fitting. In the case of $W_0(0)$ transition, allowing the power of T to vary resulted a $T^{4.14(20)}$ dependence with a fitting correlation of 0.9962. While this temperature dependence is barely consistent with the value of $T^{4.41(7)}$ for $W_1(0)$ transition, it is unlikely to be the genuine effect as we will further this in the next section.

E. Temperature dependence of line widths

Study of the temperature dependence of the line widths for the W transitions was also attempted. However, the S/N ratio of our observed spectrum was not satisfactory to exhibit consistent results. The S/N ratio became significantly worse at higher temperature as its transparency greatly reduced. With the great experimental error expected, the observed line widths of the $W_1(0)$ transition was plotted in Figure 4.8. According to the Debye model, the observed line widths were fitted using the expression $\Gamma=\Gamma_0+\Gamma_7T^7$ to obtain

Γ = 0.0157(4) + $4.30(38)\times10^{-10}T^7$ (RMS=0.887).

The fitting correlation was not satisfactory due to great uncertainty in defining the baseline of the spectrum for measuring the FWHM of the transition. The fitting quality remained about the same by vary the power of temperature in the fit with a $T^{7.36(156)}$ dependence and a correlation coefficient of 0.880. While the fitting is far from perfect, the general trend of the temperature dependence for line width is shown clearly. For the $W_0(0)$ transition, S/N ratio was not good enough to obtain a good fit for temperature dependence of line width and thus the plot is not provided here.

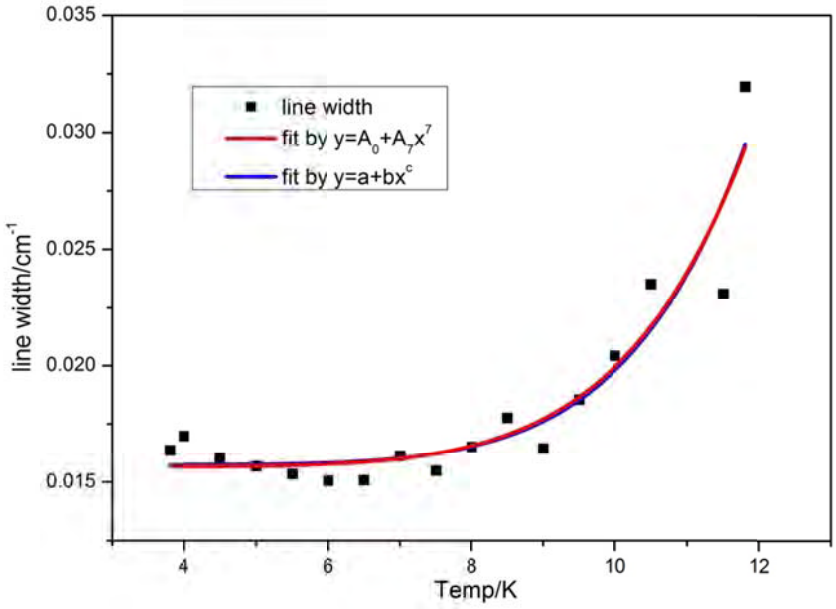

Figure 4.8 Temperature dependence of line width (FWHM) of the |M|=3←0 $W_1(0)$ transition.

4.4 Discussion

The narrowness of the transitions in solid parahydrogen allows the investigation of relaxation mechanism though the temperature dependences of line profiles and transition frequencies. In Table 4.5, we list the results of the handful of studies to date. It is noteworthy that all observed transitions exhibit Lorentzian profiles except the $Q_1(0)$ transitions reported by Oka and coworkers using stimulated Raman gain spectroscopy[51] and Codon spectroscopy[15] on solid p-H_2 samples prepared by gas pulses deposition. The Gaussian profiles observed in these experiments indicated inhomogeneous broadened line widths of ~0.0043 cm^{-1}. The temperature dependence of the transition frequency was then explained by the change of lattice constants as a result of thermal expansion. On the other hand, Kuroda et al observed an exceedingly narrow linewidth of 0.0003 cm^{-1} for the Raman $Q_1(0)$ transition in samples prepared form liquid in the high pressure regime that exhibit little thermal expansion.[12] The observed perfect Lorentzian profile and T^4 dependence of the transition frequency were explained by the acoustic phonon scattering relaxation of exciton based on the Debye model. These two studies imply that the imperfection of

the solid samples prepared in Oka's group gives rise to a typical inhomogeneous line width of about ~0.0043 cm^{-1}. As a result, the Lorentzian line profiles were not observed in their experiments due to the significantly narrower homogeneous line width.

Table 4.5 Comparison of different transitions in solid p-H_2.

transition	fitted frequency shift $\Delta\nu$ /cm^{-1}	$\Delta\nu$ (4 to 12K) /cm^{-1}	FWHM at 5K /cm^{-1}
$Q_1(0)$ Raman[a]	$\alpha(\frac{T}{T_D})^4\int_0^{T_D/T} dx\frac{x^3}{(e^x-1)}$ $\alpha = 60(4)cm^{-1}\ (T_D = 100K)$	0.058	0.0003 (Lorentzian)
$Q_1(0)$ Raman[b]			0.0047 (Gaussian)
$Q_1(0)$ Condon[c]	$2.96\times10^{-6}T^{4.096}$	0.077	0.0043 (Gaussian)
$W_1(0)$[b]	$1.20(20)\times10^{-6}T^{4.41(7)}$	0.068	0.0155 (Lorentzian)
$W_0(0)$[b]	$7.11(372)\times10^{-7}T^{4.16(22)}$	0.022	0.0104 (Lorentzian)

[a] From ref [12]

[b] From our experiments

[c] From ref [15]

In our study of W transitions, the samples were prepared using pulse deposition as in the case of Oka's group. We therefore expected similar inhomogeneous line broadening of about 0.0043 cm^{-1}. In order to examine the inhomogeneous line broadening, we measured the $Q_1(0)$ transition of our samples using stimulated Raman gain spectroscopy. The transition was observed at 4149.6694 cm^{-1} with a Gaussian line shape and a FWHM of about 0.0047 cm^{-1}, in excellent agreement with Kerr et al. The relaxation of the W transitions, however, is much faster to exhibit line width on the order of 0.01 cm^{-1} that is much broader than the inhomogeneous line width measured in our samples. As a result, the line profile of the W transitions following the Lorentzian shape dominated by a homogeneous broadening mechanism.

The great difference of the homogeneous line width between the pure vibrational $Q_1(0)$ transition and W transitions may be ascribed to the greater mismatch between the Debye frequency and vibron energy compared to between the Debye frequency and the roton energy. Furthermore, the broader homogeneous width observed for the $W_1(0)$ transition compared to $W_0(0)$ transition indicates that the phase relaxation is faster for the rotons in the v=1 band for the $W_1(0)$ transition than the roton in the v=0 band for the $W_0(0)$ transition.

As discussed by Skinner[48], the Debye model for dephasing of two-level system (TLS) by acoustic phonons in bulk crystal gives the temperature dependences for variation of transition frequency $\Delta\nu$ and line width $\Delta\Gamma$:

$$\Delta\nu = \nu_D \frac{3W}{2}\left(\frac{T}{T_D}\right)^4 \int_0^{T_D/T} dx \frac{x^3}{(e^x - 1)}$$

$$\Delta\Gamma = \nu_D \frac{9\pi W^2}{4}\left(\frac{T}{T_D}\right)^7 \int_0^{T_D/T} dx \frac{x^6 e^x}{(e^x - 1)^2},$$

where $h\nu_D = kT_D$, and T_D is the Debye temperature of the crystal (T_D=100 K for solid hydrogen). W is the dimensionless quadratic coupling constant of TLS-bath interaction. Since the temperature range in the experiments was much lower than the Debye temperature, the integrals in above equations were expected to have little temperature dependence. As a result, $\Delta\nu$ and $\Delta\Gamma$ should be give the T^4 and T^7 dependence, respectively. In the case of the $Q_1(0)$ transition, the observation by Kuroda et al were in excellent agreement with the Debye model. In our observations, the W transitions exhibited Lorentzian profiles, an indication of homogeneous line broadening, with a T^4 dependence of transition frequency. The inhomogeneous line width of about ~0.0047 cm^{-1} appeared to have little effect on the observed line profile and temperature dependence.

While transitions with Lorentzian profiles exhibit T^4 dependence in frequency shift, the pre-exponential factor are quite different for different transitions as shown in Table 4.3. The difference is due to the coupling constant W in the equations above. The theoretical expression of the coupling constant is, however, not known to date. Experimental line profiles will no doubt provide crucial information for establishing a theoretical model to interpret the coupling constant W quantitatively.

The effect of thermal expansion on frequency shift is due to the temperature

variation of the intermolecular distance. The temperature dependence of molar volume of solid p-H_2 follows the power law $\Delta V(T) = 2.233\times10^{-6}T^{4.424}cm^3/mol$, the volume change of solid hydrogen from 0 K (23.063 cm^3/mol) to triplet point 13.8 K (23.312 cm^3/mol) is very small at about 1.08%, which corresponds to the change of about 0.36% in the lattice constant R_0. Since the crystal field interaction depending on R_0^{-n} is expected to also vary with temperature, the corresponding shift of transition frequency induced by thermal expansion can therefore be approximated by $k\cdot T^{4.424}$ cm^{-1}. Based on the fitting results discussed above, the effect due to thermal expansion appears to be no more than the experimental uncertainty. In addition, the triplet structure of both W transitions remains constant relative frequencies suggesting that the thermal expansion also has little effect on the anisotropic coupling constants ε_{2c} and ε_{4c}. Together with the observed Lorentzian line profiles of the W transitions, it is very likely that the observed frequency shifts are dominated by the phonon scattering mechanism.

Because of insufficient S/N ratio in our experiments, the study of temperature dependence of line widths in our experiments was not satisfactory. While the temperature dependence of line widths roughly follow a T^7 law according to phonon scattering mechanism, more reliable results with little uncertainty will be obtained with improved S/N in the experiments. These results will provide the essential information leading to a better understanding of the relaxation mechanism.

Chapter 5 **Laser induced fluorescence spectrum of RuC**

5.1 Background

Ruthenium monocarbide (RuC) has been studied for more than four decades and numerous experimental and theoretical investigations have been reported.[52-59] The first spectroscopic studies was performed by Scullman and Thelin using a grating spectrograph and a King furnace molecular source.[52,53] Emission and absorption spectra of RuC were recorded in the near infrared and visible regions. Due to the high temperature environment of the furnace, the numerous levels of RuC were populated to give rise to a spectrum that was too congested for detail analysis as it was not possible to unambiguously determine the Ω values involved in the observed transitions. Much later Morse and coworkers[54,56] used resonant two-photon ionization (R2PI) spectroscopy and a laser ablation supersonic jet expansion (LA-SJE) molecular source to investigate the electronic transition spectrum of RuC from the near infrared to the ultra-violet spectral region. Not only had they observed those bands recorded by Scullman and Thelin,[52,53] numerous new transition bands were recorded and analyzed. Rotational structure was generally resolved in their spectrum and the ground state of RuC was determined to be the $X^1\Sigma^+$ state. Accurate molecular constants for the ground and many low-lying electronic states were reported. Using laser induced fluorescence spectroscopy and also the LA-SJE source, Steimle and coworkers[57,59] studied the Stark spectrum of RuC in the near infrared region and reported the dipole moment in the ground and many electronic states in the near infrared region. Recently, the same group performed pump/probe microwave-optical double resonance (PPMODR) study of the ground $X^1\Sigma^+$ state and reported the electric quadrupole coupling parameter for the ^{101}RuC molecule.[60] Theoretical calculations on the electronic structure of RuC were first performed by Shim *et al*[61] , using all electron Hatree-Fock at the valence configuration interaction level to predict a $^3\Delta$ ground state together with the energy order of 28 low-lying electronic states. However, in subsequent calculations using all-electron *ab initio* multi-configuration self-consistent-field (CASSCF) and multi-reference configuration interaction (MRCI)

including relativistic corrections they corrected their earlier prediction to propose the $X^1\Sigma^+$ ground state.[55] Guo and Balasubramanian[58] using CASSCF and MRCI with relativistic effective pseudo potential (REPP) computed 29 low-lying electronic states of RuC with different spin multiplicities and spatial symmetries with energy separations less than 38000 cm^{-1}. The computed spectroscopic constants and dipole moments are generally in good agreement with experimental results.

In this chapter, we report high-resolution spectroscopic study of the rotational and hyperfine structure of four electronic transition systems, namely the $[12.7]^3\Pi_2 - [0.1]^3\Delta_3$, the $[13.5]^3\Phi_3 - [0.9]^3\Delta_2$, the $[13.9]^3\Phi_4 - [0.1]^3\Delta_3$, and the $[13.9]^3\Pi_1 - [0.9]^3\Delta_2$ transitions using laser vaporization /reaction supersonic free jet expansion coupled with high resolution laser induced fluorescence spectroscopy. For these transitions, due to the excellent singal-to-noise ratio of the spectrum, species due to the natural abundance of all seven isotopes of ruthenium element were observed. In addition, partially resolved hyperfine structures of the ^{99}RuC and ^{101}RuC isotopic molecules have also been analyzed. Accurate rotational constants for the seven RuC isotopes are obtained and hyperfine constants for the ^{99}RuC and ^{101}RuC isotopes were derived.

5.2 Experimental conditions

The LIF spectrometer and laser ablation free jet expansion system has been discribed in Chapter 3. Only a brief description of experimental conditions of RuC is given here. RuC molecules were produced from the reactions of ruthenium atoms with 2% ethyl bromide (C_2H_5Br) in argon buffer. The Ru atoms were produced by laser ablation of a pure ruthenium rod using a pulsed Nd:YAG laser operated at 1064 nm and 10 Hz repetition rate with an energy of about 20 mJ per shot. The argon-buffered reagent gas was controlled by a pulse valve synchronized with Nd:YAG pulse laser with an appropriate time delay. The backing pressure of pulse valve is about 5 atm, and the background pressure of the expansion chamber is about 10^{-4} torr. The jet cooled RuC molecules were excited by a Ti:Sapphire ring laser at a power of about 0.3 W. The laser induced fluorescence signal collected by a lens system was sent to a

monochromator and detected by a photomultiplier tube (PMT). The absolute accuracy of a measured line position is about $\pm$0.002 cm^{-1}.

5.3 Results and Analysis

LIF spectrum of RuC in the NIR region between 12000 cm^{-1} and 14060 cm^{-1} has been recorded. Among the 22 transition bands observed in low resolution scan, only 13 of them were rotationally resolved and analyzed. Figure 5.1 summarizes the transitions identified and studied in this work with the bold arrows representing transitions recorded at high resolution. These bands belong to four electronic transition systems with the lower state originating from the meta-stable $^3\Delta_i$ state, namely [12.7]$^3\Pi_2$ – [0.1]$^3\Delta_3$, [13.5]$^3\Phi_3$ – [0.9]$^3\Delta_2$, [13.9]$^3\Phi_4$ – [0.1]$^3\Delta_3$, and [13.9]$^3\Pi_1$ – [0.9]$^3\Delta_2$ transitions. Ruthenium element has seven naturally occurring isotopes at the following abundances: ^{96}Ru(5.5%), ^{98}Ru(1.9%), ^{99}Ru(12.7%), ^{100}Ru(12.6%), ^{101}Ru(17%), ^{102}Ru(31.6%), ^{104}Ru(18.7%). Among the seven isotopes, only ^{99}Ru and ^{101}Ru isotopes have nonzero nuclear spin at I = 5/2. With our very intense molecular source, the LIF spectrum of all seven RuC isotopic molecules was observed with excellent signal-to-noise ratio. The hyperfine structures in the spectra of ^{99}RuC and ^{101}RuC arising from the interaction of none-zero nuclear spin with unpaired electrons have also been partially resolved.

The rotational assignment was straightforward. The observed line positions for individual isotopic molecule that has no hyperfine structure were fitted to a standard formula as follow:[33]

$$\nu = \nu_0 + B'J'(J'+1) - D'[J'(J'+1)]^2 - \{B''J''(J''+1) - D''[J''(J''+1)]^2\} \quad (1)$$

where the ′ and ′′ refer to the upper and the lower states respectively. Here ν_o stands for the vibronic energy, B is rotational constant and D is the centrifugal distortion constant. The least-square fitting of the observed transition lines was performed in two steps for each RuC isotopic molecule. Initially each band was fitted individually and, subsequently, all bands of the same system were merged together in the final fit to determine a single set of molecular constants for each vibrational level. The

molecular constants determined for the $[0.1]^3\Delta_3$, $[0.9]^3\Delta_2$, the $[12.7]^3\Pi_2$, the $[13.5]^3\Phi_3$, the $[13.9]^3\Phi_4$ and the $[13.9]^3\Pi_1$ states of the RuC isotopic molecules are listed in Table 5.1 -- Table 5.3. The four individual electronic transition systems observed are discussed in details below.

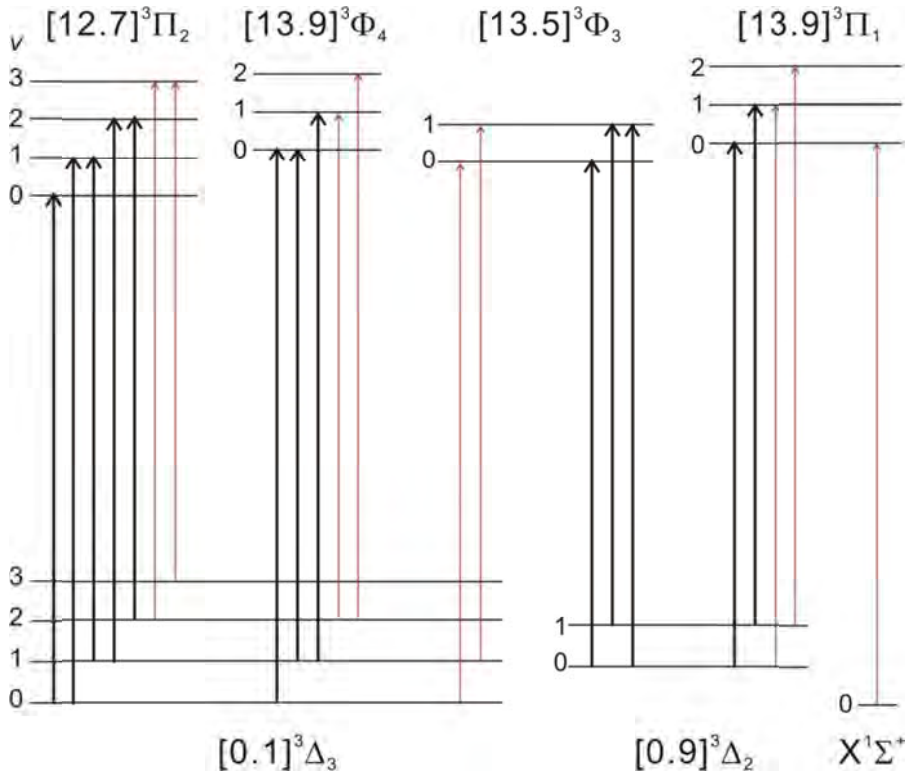

Figure 5.1 Observed electronic transitions of RuC: rotationally resolved and analyzed bands are indicated with thick lines, and other observed transition bands but not analyzed are shown by red lines.

5.3.1 The $[12.7]^3\Pi_2 - [0.1]^3\Delta_3$ transition and hyperfine structure

Five vibrational bands have been analyzed for the $[12.7]^3\Pi_2 - [0.1]^3\Delta_3$ transition system. Each vibrational band showed resolved P, Q and R branches with the first line of each branch assigned to P(3), Q(3) and R(3) respectively, which confirms unambiguously that $\Omega' = 2$ and $\Omega'' = 3$ values for the electronic states involved. Furthermore, the P branches showed greater intensity than the R branches, as expected for $\Delta\Lambda = -1$ transition. Figure 5.2 shows the band head region of the (0, 0) band, the transition lines of the isotopic molecules were only partially resolved,

whereas the transition lines of all the seven isotopic molecules were fully resolved in the (1, 0) band, as shown in Figure 5.3. The isotopic shifts between the band origin of ^{96}RuC and ^{104}RuC is about -0.044 cm^{-1} for the (0, 0) band while becoming about 4 cm^{-1} for the (1, 0) band. The molecular constants for each vibrational state studied in this transition system are listed in Table 5.1, while the derived equilibrium molecular constants are listed in Table 5.4.

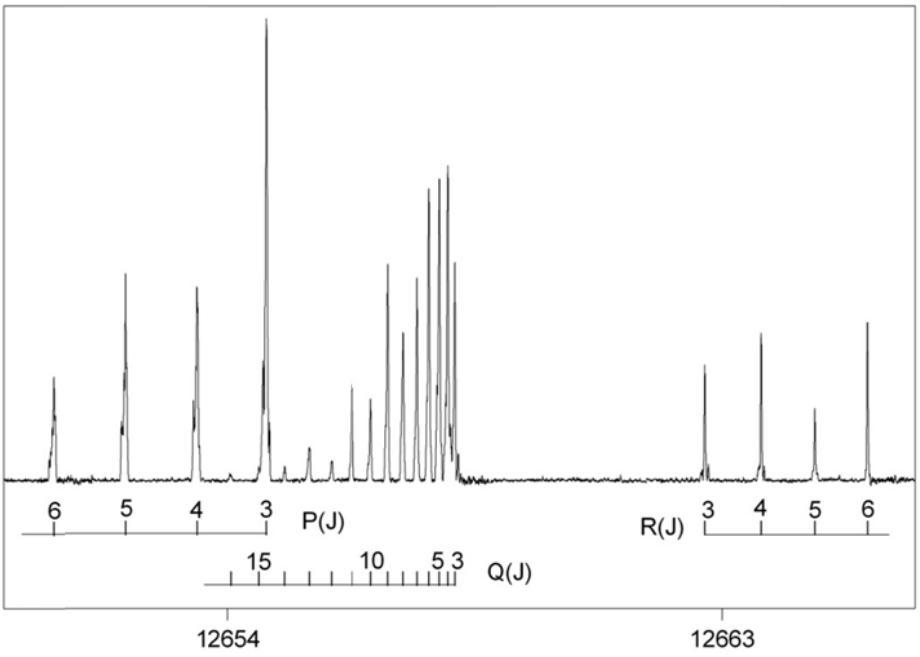

Figure 5.2 The (0,0) band of the $[12.7]^3\Pi_2 - [0.1]^3\Delta_3$ transition of RuC.

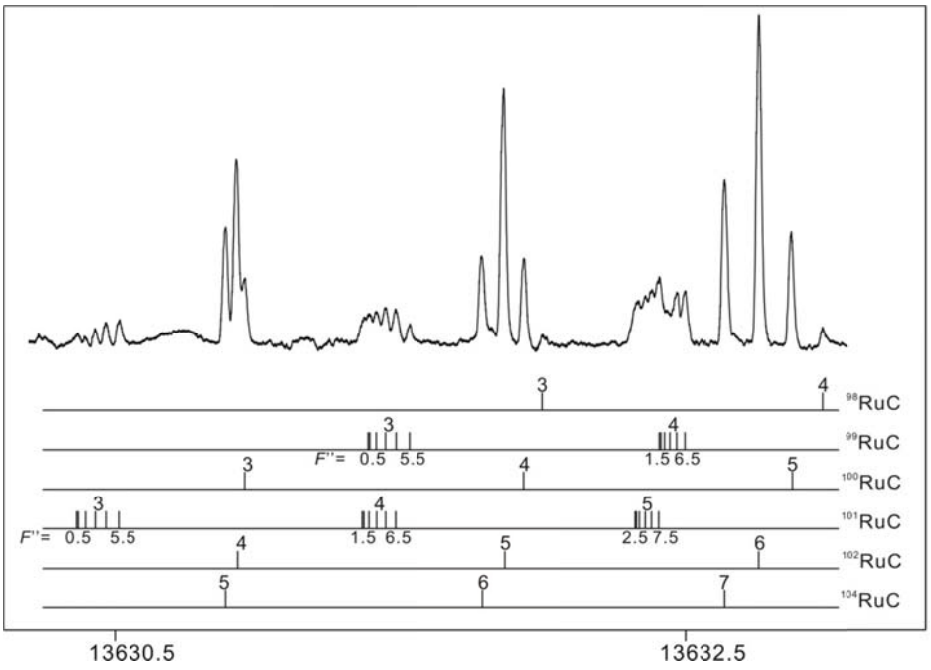

Figure 5.3 A portion of R branch of (1,0) band of the $[12.7]^3\Pi_2 - [0.1]^3\Delta_3$ transition of RuC showing isotopic shifts and hyperfine structure.

For the (1, 0) band of the ^{99}RuC and ^{101}RuC isotopic molecules, the low J lines of this band exhibited partially resolved hyperfine structure, which arises from the interaction between none-zero nuclear spin and unpaired electrons in the molecules. As show in Figure 5.3, it is easily noticed that the hyperfine structure decreases rapidly as J increases, which confirms the Hund's case a_β scheme for the hyperfine interaction. The grand total quantum number F is the resultant from coupling the nuclear spin momentum I with the total angular momentum J (i.e. F = I + J). In the spectrum, transitions with $\Delta J = \Delta F = -1$ are expected to be strong. The assignment of the hyperfine components is straightforward. Since the hyperfine structure is dominated by the lower $[0.1]^3\Delta_3$ state, it shows a nice pattern obeying the Lande interval rule[62], which suggests that the interval between successive components is proportional to the larger of their total angular momentum values (that is the separation is largest for the highest F value). The Hamiltonian for the hyperfine interactions is given by (2), and the terms involved are the nuclear spin electron orbit interaction, Fermi contact interaction and the dipolar nuclear spin electron spin interaction respectively:

$$\hat{H}_{hfs} = a\hat{I}_Z \cdot \hat{L}_Z + b\hat{I} \cdot \hat{S} + c\hat{I}_Z \cdot \hat{S}_Z \qquad (2)$$

where a, b, and c parameters are the same as those defined by Frosch and Foley.[63] The matrix elements of the hyperfine Hamiltonian for $^3\Delta_3$ and $^3\Pi_2$ states in the Hund's case a_β coupling scheme can be found in Azuma *et al*:[64]

$$\left\langle J\Omega IF\left|\hat{H}_{hfs}\right|J\Omega IF\right\rangle = \frac{\Omega \cdot h[F(F+1) - I(I+1) - J(J+1)]}{2J(J+1)} \qquad (3)$$

$$\left\langle J\Omega IF\left|\hat{H}_{hfs}\right|J-1,\Omega IF\right\rangle = \frac{h \cdot \sqrt{J^2-\Omega^2} \cdot \sqrt{(I+J+F+1)(J+F-I)(J+I-F)(I+J+F+1)}}{2J\sqrt{(2J+1)(2J-1)}} \qquad (4)$$

where h assumes the value of $a\Lambda + (b + c)\Sigma = a + (b+c)$ for a $^3\Pi_2$ sub-state (that is with $\Lambda = 1$ and $\Sigma = 1$) and the value of $a\Lambda + (b + c)\Sigma = 2a + (b + c)$ for a $^3\Delta_3$ sub-state (that is with $\Lambda = 2$ and $\Sigma = 1$).

The observed line positions of the (1, 0) band of the $[12.7]^3\Pi_2 - [0.1]^3\Delta_3$ transition for ^{99}RuC and ^{101}RuC were fitted to the Hamiltonian matrix with expressions (3) and (4) for retrieving the hyperfine parameter of the upper and lower states. For both ^{99}RuC and ^{101}RuC molecules, about 160 transition lines have been included in the least-squares fit in each case. Table 5.3 listed the hyperfine parameters for the $[12.7]^3\Pi_2$ and the $[0.1]^3\Delta_3$ states obtained in the fit. Since the meta-stable $[0.1]^3\Delta_3$ state is 75.953 cm^{-1} above the ground state for ^{102}RuC isotope,[54] this energy difference is designated by a in Table 5.1. The sign of the hyperfine parameter is negative for $[12.7]^3\Pi_2$ but positive for $[0.1]^3\Delta_3$. It is rather unusual that the molecular constants for all the RuC isotopes can be determined together with the hyperfine constants for both ^{99}RuC and ^{101}RuC isotopes. Compared to the previous work, structural parameters in this work appear to have much better accuracy. A comparison with molecular constants obtained by Morse and coworkers for ^{102}RuC and ^{101}RuC molecules is also given in the tables.

5.3.2 The $[13.9]^3\Phi_4 - [0.1]^3\Delta_3$ transition and its hyperfine structure

The (0, 0), (0, 1) and (1, 1) bands of the $[13.9]^3\Phi_4 - [0.1]^3\Delta_3$ transition system were observed and analyzed. Each band showed resolved P, Q and R branches with P(5), Q(4) and R(3), respectively, as the first line for each branch. This confirmed

unambiguously the electronic states with $\Omega' = 4$ and $\Omega'' = 3$ were involved. Figure 5.4 shows a portion of R branch of the (0, 1) band, the intensity of the P branches is generally weaker, which is consistent with an electronic transition with $\Delta\Lambda = +1$. For this transition system, all rotational lines of the seven isotopic molecules were measured and fitted to derive the molecular constants for each vibrational level involved as well as equilibrium position as shown in Table 5.1, Table 5.3 and Table 5.4, respectively.

As shown in Figure 5.4, the $[13.9]^3\Phi_4 - [0.1]^3\Delta_3$ transition for ^{99}RuC and ^{101}RuC exhibited hyperfine structure. Similar to the $[12.7]^3\Pi_2 - [0.1]^3\Delta_3$ system mentioned above, the hyperfine splitting also conforms to the Hund's case a_β coupling scheme. The hyperfine parameter for the $^3\Phi_4$ state ($\Lambda = 2$ and $\Sigma = 1$) is h = 3a + (b+c). For the (0, 1) band, 130 and 139 transition lines were included in the separate least-squares fitting for ^{99}RuC and ^{101}RuC respectively. In the case of the (1, 1) band, 144 and 150 transition lines were separately fitted for ^{99}RuC and ^{101}RuC molecules, respectively. The results obtained are listed in Table 5.3. The obtained hyperfine parameters h for the v = 0 and 1 levels of the $[1.0]^3\Delta_3$ state are found very close for either isotopic species. They are -0.0267(3) and -0.0247(10) cm^{-1}, respectively, for ^{99}RuC and -0.0294(5) and -0.0302(10) cm^{-1}, respectively, for ^{101}RuC.

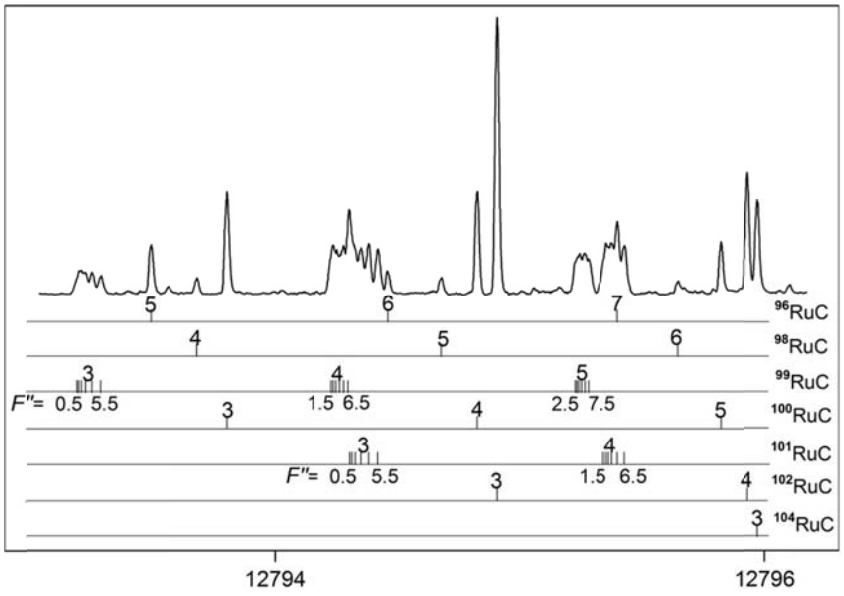

Figure 5.4 The R branch of (0,1) band of the $[13.9]^3\Phi_4 - [0.1]^3\Delta_3$ transition of RuC showing transition lines with isotopic shift and hyperfine structure.

5.3.3 The $[13.5]^3\Phi_3 - [0.9]^3\Delta_2$ transition

Three vibrational bands, namely (0, 0), (1, 0) and (1, 1) have been analyzed for the $[13.5]^3\Phi_3 - [0.9]^3\Delta_2$ transition system. Similar to systems discussed above, each vibrational band showed resolved P, Q and R branches with the first lines of the branches assigned to P(4), Q(2) and R(2) respectively, corresponding to $\Omega' = 3$ and $\Omega'' = 2$ values for the electronic states involved. Furthermore, the R and Q branches have higher intensity than the P branch, consistent with a $\Delta\Lambda = +1$ transition. Figure 5.5 shows the band head region of the (0, 0) band. Transition lines of all the seven isotopic molecules were measured and included in the least-squares fitting. The molecular constants for the $[13.5]^3\Phi_3$ and $[0.9]^3\Delta_2$ states obtained from the fitting are listed in Table 5.2-5.4, respectively. Since the $[0.9]^3\Delta_2$ state is 850.386 cm^{-1} above the ground state for ^{102}RuC isotope,[54] the difference is designated by b in Table 5.2 and Table 5.3.

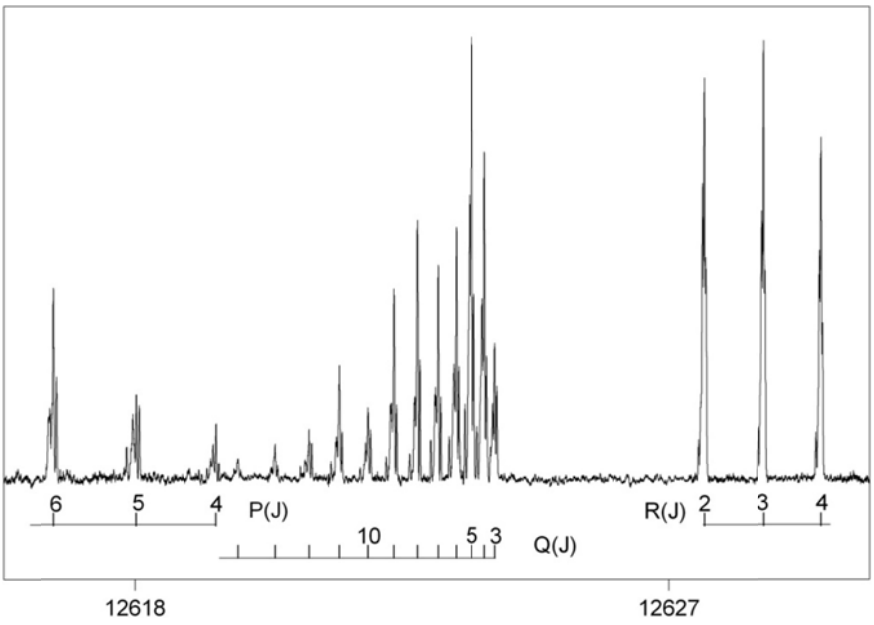

Figure 5.5 The (0,0) band of the $[13.5]^3\Phi_3 - [0.9]^3\Delta_2$ transition of RuC.

5.3.4 The $[13.9]^3\Pi_1 - [0.9]^3\Delta_2$ transition

Only the (0, 0) and (1, 1) bands of the $[13.9]^3\Pi_1 - [0.9]^3\Delta_2$ transition system were observed and analyzed. Both vibrational bands showed resolved P, Q and R branches with the first lines of the branches assigned to P(2), Q(2) and R(2) respectively, consistent with $\Omega' = 1$ and $\Omega'' = 2$ values for the electronic states involved. Furthermore, the P and Q branches have higher intensity than the R branch, consistent with a $\Delta\Lambda = -1$ transition. Figure 5.6 depicts a portion of the P branch of the (1, 1) band, where transition lines of the seven isotopic molecules are present. Molecular constants obtained from least-squares fitting for each isotopic species are listed in Table 5.2 with their corresponding equilibrium molecular constants listed in Table 5.4.

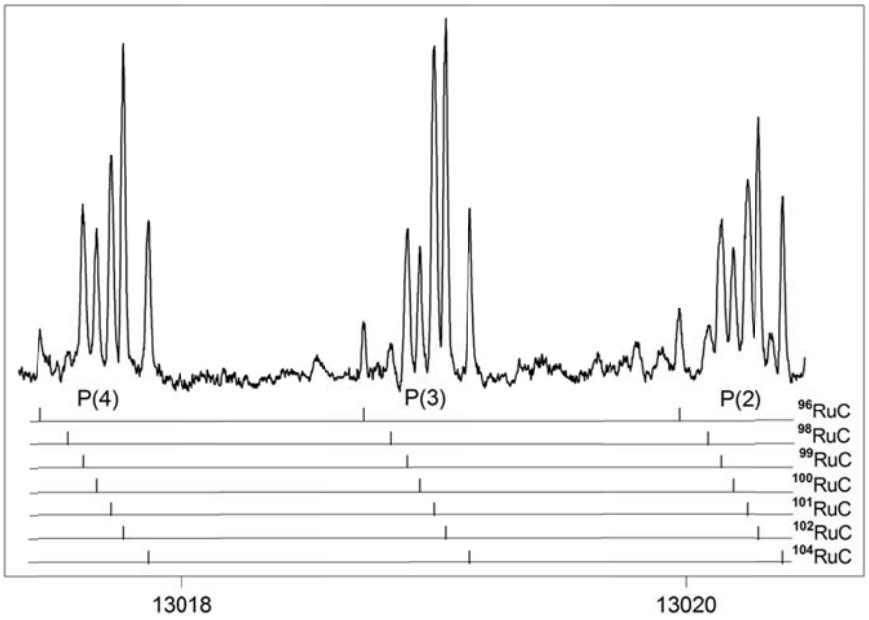

Figure 5.6 The P branch of (1,1) band of the $[13.9]^3\Pi_1 - [0.9]^3\Delta_2$ transition of RuC showing transition lines of all seven isotopic molecules.

5.4 Discussion

As discussed by Morse and coworkers[54], the $[0.1]^3\Delta_3$ and the $[0.9]^3\Delta_2$ sub-states are spin components of a low-lying $^3\Delta_i$ state with an electronic configuration of

$10\sigma^2 11\sigma^2 5\pi^4\ 2\delta^3 12\sigma^1$. For transition metal systems with unpaired electron in orbital with significant σ*s* character on the transition metal atom, h is dominated by the Fermi contact interaction, b_F, which is much larger than either the a or c constants. Since the 12σ orbital is basically a non-bonding orbital formed from the 4*s* orbital of the Ru atom, the hyperfine constant, h, for the $[0.1]^3\Delta_3$ state, can be estimated using the following expression[63]:

$$b = b_F - \frac{1}{3}c \qquad (5)$$

$$a = \left(\frac{\mu_o}{4\pi\, hc}\right) g\, g_N\, \mu_B\, \mu_N \left(\frac{1}{2S}\right) \sum_i \left\langle r_i^{-3} \right\rangle_{n\ell} \qquad (6)$$

$$b_F = \left(\frac{\mu_o}{4\pi hc}\right) \frac{8\pi}{3} g\, g_N \mu_B\, \mu_N \left(\frac{1}{2S}\right) \sum_i \left\langle \psi_i^2(o) \right\rangle_{n\ell}, \text{ and} \qquad (7)$$

$$c = \left(\frac{\mu_o}{4\pi hc}\right) \frac{3}{2} g\, g_N\, \mu_B \mu_N \left(\frac{1}{2S}\right) \sum_i \left\langle 3\cos^2\theta_i - 1 \right\rangle_{\ell\lambda} \left\langle r_i^{-3} \right\rangle_{n\ell}. \qquad (8)$$

$h = a\Lambda + (b + c)\,\Sigma = a\Lambda + (b_F + 2c/3)\,\Sigma$

The expected value in the expressions above should be averaged over the electronic space coordinates and where g, g_N, μ_B and μ_N are the usual g-factor, nuclear g-factor, Bohr magneton and the nuclear magneton, respectively, for ^{101}Ru and ^{99}Ru.[65] S is the spin multiplicity (for the triplet state S=1) and the expectation values $\left\langle \psi_{5s}^2(o) \right\rangle$ and $\left\langle r^{-3} \right\rangle_{n\ell}$ of the Ru atom can be found from Weltner.[66] The angular expectation value of atomic function, $\left\langle 3\cos^2\theta_i - 1 \right\rangle$, for the three dδ electrons is 3×(-4/7).[67] Despite of the fact that the electric quadrupole interaction, e^2Qq_0, contributes to the hyperfine structure of the $X^1\Sigma^+$ state,[57] we did not include this term because it is a very small effect compared with the magnetic hyperfine interaction and also the hyperfine splitting lines in our spectrum are only partially resolved. Using expressions (5) to (8), we estimated the hyperfine constants for the $[0.1]^3\Delta_3$ sub-state for the two RuC isotopic molecules. The experimentally measured hyperfine constants and those values estimated from theory are compared below.

$h_{\Omega=3}$	^{99}RuC	^{101}RuC
Cal.	-0.0233	-0.0299

Exp.	-0.0267	-0.0294

The agreement between these values is good. For the $[0.9]^3\Delta_2$ state, because Σ = 0, there will not be any contribution from the Fermi contact and dipolar terms to the $h_{\Omega=2}$ parameter, and its hyperfine splitting is very small, and in fact for transitions involving the $[0.9]^3\Delta_2$ state we have not been able to notice any broadening in line width. As far as the excited states are concerned, the electronic configuration $10\sigma^2 11\sigma^2 5\pi^4 2\delta^3 6\pi^1$ will give rise to the $^3\Phi_i$ and $^3\Pi_i$ observed in this work.[54] Since there is no electron in any σs orbital, the Fermi contact interaction term is negligible and the hyperfine structure is generally very small. Estimating from the hyperfine parameters mentioned above in expression (5) to (8), the signs are correctly predicted but the values are about 0.010 cm^{-1} for both isotopes, which are larger than the experimental values stated in Table 5.3.

The molecular parameters of different isotopic molecules are related by various powers of the mass dependence: $\rho=(\mu/\mu_i)^{1/2}$, where μ and μ_i are the reduced mass of the molecule and its isotopic molecule. Since ^{102}RuC is the most abundant isotope, the isotopic effects of other molecules are calculated relative to it. Table 5.5 shows the calculated isotopic parameters: B_0 and $\Delta G_{1/2}$, which are related to ρ^2 and ρ respectively.[62] The agreement between experimental and calculated values is excellent.

It is rather unusual to be able to record and analyze electronic transition spectrum of all the seven isotopic molecules of ruthenium compounds with natural abundance. It is probably due to the very intense molecular source used in this work, which allows even the ^{98}RuC isotope with only 1.9% to be recorded. This outcome was a surprise to us because we were targeting the RuBr molecule at the start. In our preliminary search for the electronic transition spectrum of gas-phase ruthenium halides, the Ru atom generated in the ablation source were allowed to react with ethyl bromide (C_2H_5Br), but we have not been able to find any RuBr spectrum in the spectral region scanned. However, the spectrum of the RuC molecule showed up with very high intensity, which indicates the Ru atom has very strong affiliation towards the carbon atoms in the ethyl bromide than the usual bromine atom. The

phenomenon should be quite familiar to people working in the area of catalyst such as Grubbs catalyst[68] for manipulating carbon atoms in the formation and destruction of carbon bonds.

In conclusion, the electronic spectrum of diatomic RuC generated in laser vaporization/reaction supersonic free jet expansion was recorded from 12000 to 14060 cm^{-1} using high resolution laser induced fluorescence spectroscopy. Four electronic transition systems, namely, the $[12.7]^3\Pi_2$-$[0.9]^3\Delta_3$, the $[13.5]^3\Phi_3$-$[0.9]^3\Delta_2$, the $[13.9]^3\Phi_4$-$[0.1]^3\Delta_3$, and $[13.9]^3\Pi_1$-$[0.9]^3\Delta_2$ transitions were observed and analyzed. All the seven RuC isotopomers were observed in the spectrum and the corresponding molecular constants of all isotopomers were obtained. The transitions originated from the $[0.1]^3\Delta_3$ state show clear hyperfine splitting in the spectrum. Hyperfine constants of the $[0.1]^3\Delta_3$(v=0, 1), $[12.7]^3\Pi_2$(v=1), and $[13.9]^3\Phi_4$(v=0, 1) are retrieved with better accuracy compared to the previous work by Morse's group. Based on the fitting results, it is confirmed the observed hyperfine structure is essentially from $[0.1]^3\Delta_3$ state.

Table 5.1 Molecular constants for the $[13.9]^3\Phi_4$, $[12.7]^3\Pi_2$ and $[0.1]\ ^3\Delta_3$ electronic states of RuC (cm^{-1}).[a]

State	Parameter	^{96}RuC	^{98}RuC	^{100}RuC	^{102}RuC	^{104}RuC	^{102}RuC[b]
$[13.9]^3\Phi_4$	T_1	14766.783(1)	14765.762(2)	14764.780(1)	14763.837(1)	14762.921(1)	14763.810
	B_1	0.56710(2)	0.56585(3)	0.56459(2)	0.56334(2)	0.56220(1)	0.56325
	T_0	13820.0118(7)	13820.049(2)	13820.0916(6)	13820.1319(7)	13820.1629(6)	13820.116
	B_0	0.57128(2)	0.57007(4)	0.56875(1)	0.56750(1)	0.56635(1)	0.56739
$[12.7]^3\Pi_2$	T_2			14584.771(1)	14582.790(1)	14580.871(1)	14582.764
	B_2	0.56514(8)		0.56254(2)	0.56130(2)	0.56028(2)	0.56118
	T_1	13628.7630(5)	13627.678(2)	13626.6490(6)	13625.6527(6)	13624.6897(6)	13625.622
	B_1	0.56981(2)	0.56869(5)	0.56729(2)	0.56607(2)	0.56490(1)	0.56603
	T_0				12658.3094(9)		12658.110
	B_0				0.57005(2)		0.56994
$[0.1]\ ^3\Delta_3$	T_2			2051.671(2)	2049.543(2)	2047.486(2)	
	B_2	0.58216(9)		0.57942(3)	0.57817(3)	0.57703(3)	
	T_1	1032.941(1)	1031.777(2)	1030.6633(9)	1029.590(1)	1028.5504(8)	1029.593
	B_1	0.58574(2)	0.58454(4)	0.58317(2)	0.58189(2)	0.58072(1)	0.58201
	T_0	*a*					
	B_0	0.58950 (2)	0.58804(5)	0.58691(1)	0.58565(2)	0.58443(1)	0.58553

[a] Error limits are given in parentheses in units of the last reported digits and represent 1σ in the fitted quality.

[b] The absolute value of *a* is 75.953 cm^{-1} (other T_n values in this table are relative to *a*) and the molecular constants for ^{102}RuC are from Ref[54].

Table 5.2 Molecular constants for the $[13.9]^3\Pi_1$, $[13.5]^3\Phi_3$ and $[0.9]\ ^3\Delta_2$ electronic states of RuC (cm^{-1}).[a]

State	Parameter	^{96}RuC	^{98}RuC	^{100}RuC	^{102}RuC	^{104}RuC	^{102}RuC[b]
$[13.9]^3\Pi_1$	T_1			14053.567(2)	14052.590(1)	14051.643(2)	14052.556
	B_1	0.56872(3)	0.56775(11)	0.56635(2)	0.56508(2)	0.56396(2)	0.56505
	T_0	13094.812			13094.869		13094.844
	B_0	0.57296(3)			0.56912(1)		0.56908
$[13.5]^3\Phi_3$	T_1			13565.3776(7)	13563.4393(5)	13563.5324(7)	
	B_1	056478(4)		0.56234(2)	0.56110(2)	0.55996(2)	
	T_0	12624.211	12624.260	12624.2908(7)	12624.3305(5)	12624.3660(6)	12624.318
	B_0	0.56906(3)	0.56770(16)	0.56655(2)	0.56528(1)	0.56415(2)	0.56524
$[0.9]\ ^3\Delta_2$	T_1			1031.007(1)	1029.9338(8)	1028.8972(9)	
	B_1	0.58718(4)	0.58609(12)	0.58468(2)	0.58337(2)	0.58221(2)	0.58711
	T_0	b[b]					
	B_0	0.59107(3)	0.58978(12)	0.58846(2)	0.58716(1)	0.58597(2)	

[a] Error limits are given in parentheses in units of the last reported digits and represent 1σ in the fitted quality.

[b] The value of *b* is 850.386 cm^{-1} (other T_n values in this table are relative to b) and the molecular constants for ^{102}RuC are from Ref[54].

Table 5.3 Molecular constants for the $[13.9]^3\Pi_1$, $[13.9]^3\Phi_4$, $[13.5]^3\Phi_3$, $[12.7]^3\Pi_2$, $[0.9]\ ^3\Delta_2$ and $[0.1]\ ^3\Delta_3$ electronic states of ^{99}RuC and ^{101}RuC (cm^{-1}).[a]

State	Parameter	^{99}RuC	^{101}RuC	^{101}RuC[b]
$[13.9]^3\Pi_1$	B_1	0.56705(3)	0.56570(3)	
$[13.9]^3\Phi_4$	B_1	0.565213(13)	0.563885(11)	
	h_1	-0.0047(2)	-0.0077(2)	
	B_0	0.569369(11)	0.568061(10)	
	h_0	-0.0034(8)	-0.0043(8)	
$[13.5]^3\Phi_3$	T_1	b+13565.868	b+13564.910	
	B_1	0.56294(6)	0.56168(3)	
$[12.7]^3\Pi_2$	T_1	a+13627.169	a+13626.150	
	B_1	0.567906(4)	0.566719(6)	
	h_1	0.0020(4)	0.0068(7)	0.008(5)
$[0.9]\ ^3\Delta_2$	B_1	0.58542(3)	0.58403(3)	
	T_0	b		
	B_0	0.58914(6)	0.58778(3)	
$[0.1]\ ^3\Delta_3$	B_1	0.583839(13)	0.582459(11)	
	h_1	-0.0247(10)	-0.0302(10)	
	T_0	a		
	B_0	0.587518(3)	0.586291(6)	
	h_0	-0.0267(3)	-0.0294(5)	-0.030(3)

[a] Error limits are given in parentheses in units of the last reported digits and represent 1σ in the fitted quality.

[b] The values of *a* and *b* are 75.953 and 850.386 cm^{-1} and the molecular constants for ^{102}RuC are from Ref[54].

Table 5.4 Equilibrium molecular constants for the electronic states of RuC (cm^{-1}).[a]

!

	Parameter	^{96}RuC	^{98}RuC	^{99}RuC	^{100}RuC	^{101}RuC	^{102}RuC	^{104}RuC	^{102}RuC[b]
$[13.9]^3\Pi_1$	$\Delta G_{1/2}$						957.721(1)		957.713
	B_e	0.57507					0.57115		0.57131
	α_e	0.00423					0.00405		0.00409
	r_e (Å)	1.65797							1.65785
$[13.9]^3\Phi_4$	$\Delta G_{1/2}$	946.771(2)	945.713(3)	945.192	944.688(1)	944.191	943.705(1)	942.758(1)	943.694
	B_e	0.57338	0.57218	0.57145	0.57083	0.57015	0.56957	0.56842	0.56952
	α_e	0.00419	0.00422	0.00416	0.00416	0.00418	0.00416	0.00415	0.00414
	r_e (Å)	1.66031							1.66046
$[13.5]^3\Phi_3$	$\Delta G_{1/2}$				941.087(1)		940.1088(7)	939.1664(9)	
	B_e	0.57120			0.56865		0.56738	0.56624	0.56725
	α_e	0.00428			0.00421		0.00419	0.00418	0.00411
	r_e (Å)	1.66352							1.66377
$[12.7]^3\Pi_2$	$\Delta G_{3/2}$				958.122(2)			956.181(2)	
	ω_e						977.5493		977.81
	$\omega_e x_e$						5.1031		5.165
	B_e	0.57681			0.57442		0.57237(38)	0.57186	0.57187
	α_e	0.00467			0.00475		0.00437(22)	0.00462	0.00402
	r_e (Å)	1.65554							1.65704
$[0.9]\ ^3\Delta_2$	$\Delta G_{1/2}$				1031.007(1)		1029.9338(8)	1028.8972(9)	
	B_e	0.59302	0.59163	0.59100	0.59035	0.58965	0.58905	0.58784	
	α_e	0.00389	0.00370	0.00372	0.00378	0.00375	0.00379	0.00376	
	r_e (Å)	1.63265							
$[0.1]\ ^3\Delta_3$	$\Delta G_{1/2}$		1031.777(2)		1030.663(1)		1029.590(1)	1028.550(1)	1029.587
	ω_e				1040.3194		1039.2258	1038.1656	
	$\omega_e x_e$				4.82805		4.81805	4.80760	
	B_e	0.59131(9)	0.58978	0.58935	0.58878(0)	0.58821	0.58751(2)	0.58627(1)	0.58729
	α_e	0.00367(5)	0.00350	0.00368	0.00374(0)	0.00383	0.00374(1)	0.00370(0)	0.00351
	r_e (Å)	1.63489							1.63515

[a] Error limits are given in parentheses in units of the last reported digits and represent 1σ in the fitted quality.

[b] The molecular constants for ^{102}RuC are from Ref[54].

Table 5.5 Mass scaled molecular constants for the observed electronic states of RuC (cm^{-1}).

State	Parameter	^{96}RuC	^{98}RuC	^{99}RuC	^{100}RuC	^{101}RuC	^{102}RuC	^{104}RuC
$[13.9]^3\Pi_1$	B_0	0.573809	0.572505	0.571873	0.571254	0.570646	0.569123	0.567967
	$\Delta G_{1/2}$	960.873	959.780	959.250	958.731	958.221	957.721	956.748
$[13.9]^3\Phi_4$	B_0	0.571236	0.569938	0.569309	0.568693	0.568087	0.567495	0.566343
	$\Delta G_{1/2}$	946.811	945.734	945.212	944.700	944.197	943.705	942.746
$[13.5]^3\Phi_3$	B_0	0.569011	0.567717	0.567091	0.566477	0.565874	0.565284	0.564136
	$\Delta G_{1/2}$	943.203	942.130	941.610	941.100	940.599	940.109	939.154
$[12.7]^3\Pi_2$	B_0	0.573809	0.572504	0.571873	0.571254	0.570646	0.570051	0.568893
	$\Delta G_{1/2}$	970.526	969.422	968.888	968.363	967.848	967.343	966.360
$[0.9]\ ^3\Delta_2$	B_0	0.591028	0.589684	0.589034	0.588396	0.587770	0.587157	0.585965
	$\Delta G_{1/2}$	1033.323	1032.148	1031.579	1031.020	1030.471	1029.934	1028.888
$[0.1]^3\Delta_3$	B_0	0.589506	0.588166	0.587517	0.586881	0.586256	0.585645	0.584456
	$\Delta G_{1/2}$	1032.978	1031.803	1031.234	1030.676	1030.127	1029.590	1028.544

Chapter 6 **Preliminary spectroscopic studies of IrP and IrB**

In this chapter, preliminary results of Ir-containing diatomic molecules are discussed. Iridium plays important roles in catalysis process. For instance, iridium compounds are known as catalysts in the formation of carbon-hydrogen and carbon-oxygen bonds. The study of the electronic structure of Ir-containing compounds will no doubt provide some insight in understanding mechanism of these processes. Two molecules, namely, iridium phosphide (IrP) and iridium boride (IrB) have been studied using high resolution LIF spectroscopy in the near infrared region using our apparatus. The details of these studies are presented below.

6.1 Laser induced fluorescence spectrum of IrP

6.1.1 Background

Transition metal phosphides have remarkable properties which hold the promise in the applications of semiconductor, electronic devices, and catalysts and so on.[69,70] Simple transition metal phosphides can serve as simple model for more complex organic/inorganic transition metal ligand systems.[19] Gas phase spectroscopic studies of these simple systems provide information on the bonding nature between the transition metal and phosphide, which will provide a better understanding of their properties.

Simple iridium compounds have been model systems in studying the role of 5d valence electrons. As far as the gas phase iridium containing diatomic molecules are concerned, only six species have been reported to date, IrO,[71] IrC,[72] IrN,[72] IrF,[73] IrB[6] and IrP[74,75]. Among these species, IrP was observed independently by Pang et al.[75] and A.G. Adam et al.[74] in 2010. Pang et al. reported medium resolution spectrum of five electronic transitions of IrP in the visible region and confirmed the $X^1\Sigma^+$ ground state. In addition to observing two electronic transitions in the same region at higher resolution, Adam et al. also calculated the electronic properties of IrP based on multi-reference configuration interaction (MRCI). Based on these studies, we studied

the electronic spectrum of IrP in the near infrared region involving transitions between low lying states. Four new electronic transitions have been observed for the two isotopes ^{193}IrP and ^{191}IrP. Molecular constants for the states involved were derived from least-squares fitting of the observed transitions.

6.1.2 Experimental conditions

IrP molecules were produced by reacting laser ablated iridium vapor with phosphine (PH_3) gas followed by supersonic free jet expansion. Laser pulses of 1064 nm radiation at 20 mJ from a Nd:YAG laser operated at 10 Hz repetition rate were focused onto the surface of a iridium rod to generate iridium vapor, which was then allowed to react with a mixture of 1% PH_3 in argon released from a pulsed valve to produce the IrP molecule. The backing pressure at the pulsed valve was set to 5 atm and the background pressure of the working chamber is around 10^{-4} torr.

Jet cooled IrP molecules were excited by a ring Ti-sapphire laser operated in 12000 - 14000 cm^{-1} region. The ring laser was pumped by a diode pump solid state (DPSS) laser with the wavelength set at 532 nm. A lens system collected the laser induced fluorescence signal which was then sent through a monochromator, and the signal was monitored by a photomultiplier tube (PMT). The Ti-sapphire laser output frequency was calibrated to an uncertainty of about $\pm$0.002 cm^{-1} as described before.

6.1.3 Results and analysis

Laser induced fluorescence spectrum of IrP in the NIR region 12000-14000 cm^{-1} has been recorded. During a low resolution broadband scan, 7 transition bands were observed as shown in Figure 6.1. Among the five bands recorded, to date, in high resolution scans, two bands are assigned to $[12.3]^1\Pi_1$- $X^1\Sigma^+$ transition, two bands are assigned to transitions between unidentified triplet states, and one band appears to be seriously perturbed. While iridium element has two isotopes, ^{191}Ir (37.3%) and ^{193}Ir (62.7%), only the isotopic specie ^{193}IrP in the two bands of the $[12.3]^1\Pi_1$- $X^1\Sigma^+$ transition were assigned. On the other hand, both two isotopic species have been

observed in the other four bands at high resolution.

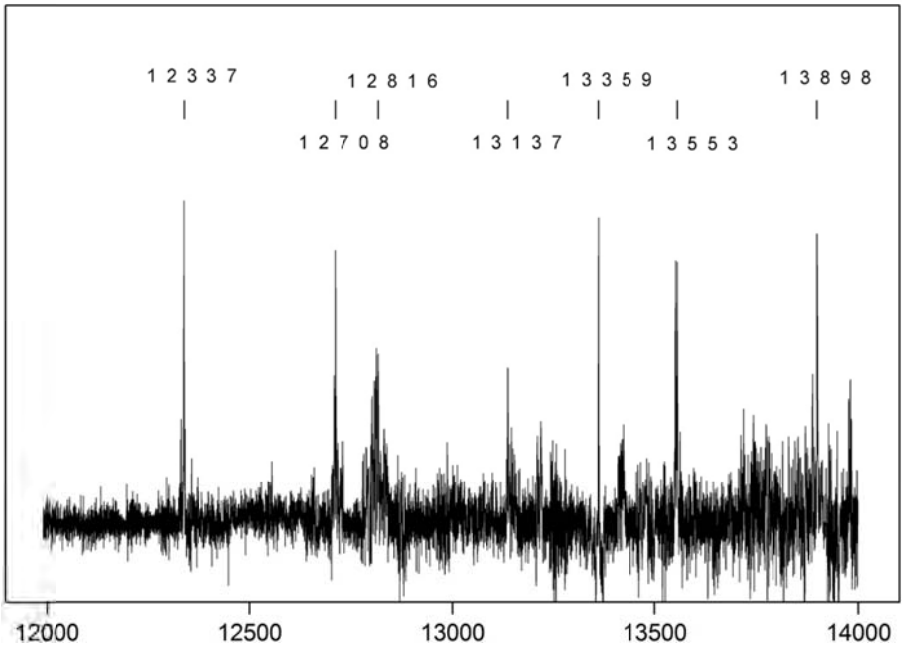

Figure 6.1 Broadband scanned spectrum between 12000 and 14000 cm^{-1} of IrP.

(1) The $[12.3]^1\Pi_1$- $X^1\Sigma^+$ transition

Two vibrational bands with band head located at 12337 cm^{-1} and 12816 cm^{-1} have been analyzed for the $[12.3]^1\Pi_1$-$X^1\Sigma^+$ transition system. Each vibrational band shows resolved P, Q and R branches. The first lines of each branch were assigned to P(2), Q(1) and R(0) respectively, in agreement with $\Omega' = 1$ and $\Omega'' = 0$ values for the electronic states involved. Furthermore, the R branches show greater intensity than the P branches, which was consistent with a $\Delta\Lambda = 1$ transition. The band located at 12337 cm^{-1} is shown in Figure 6.2. Only the transitions of ^{193}IrP were assigned from the spectrum. While transitions due to ^{191}IrP was not picked up, there were many identified weaker lines (marked with red stars *). It will need a better signal-to-noise ratio in order to investigate if they are the transitions of ^{191}IrP. The band located at 12816 cm^{-1} exhibited a similar pattern, with lines of ^{193}IrP assigned and remaining lines to be identified, as seen in Figure 6.3. These two bands located at 12337 cm^{-1} and 12816 cm^{-1} are preliminarily assigned to (v,0) and (v+1,0) vibrational bands respectively based on the least-squares fitting of the assigned lines. The vibrational quantum number v in the excited state cannot be determined with no ambiguity due to the limited information to date. Rotational line positions of each band were fitted

to the following expression:

$$\nu = \nu_0 + B'J'(J'+1) - D'[J'(J'+1)]^2 - \{B''J''(J''+1) - D''[J''(J''+1)]^2\}, \quad (62)$$

where the constants carry the usual meaning. In the least-squares fitting, the molecular constants for v=0 level of the $X^1\Sigma^+$ state were fixed to those reported by Adam et al., while the centrifugal distortion constant was set to zero since only low J lines were recorded. The fitted molecular constants are listed in Table 6.1.

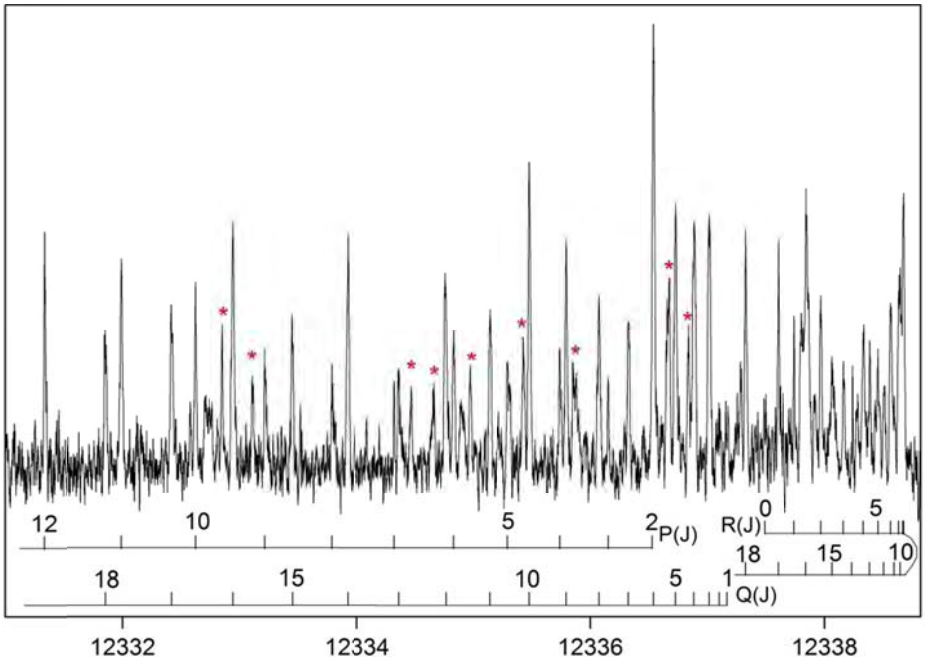

Figure 6.2 The (v,0) band of the $[12.3]^1\Pi_1$- $X^1\Sigma^+$ transition of IrP.

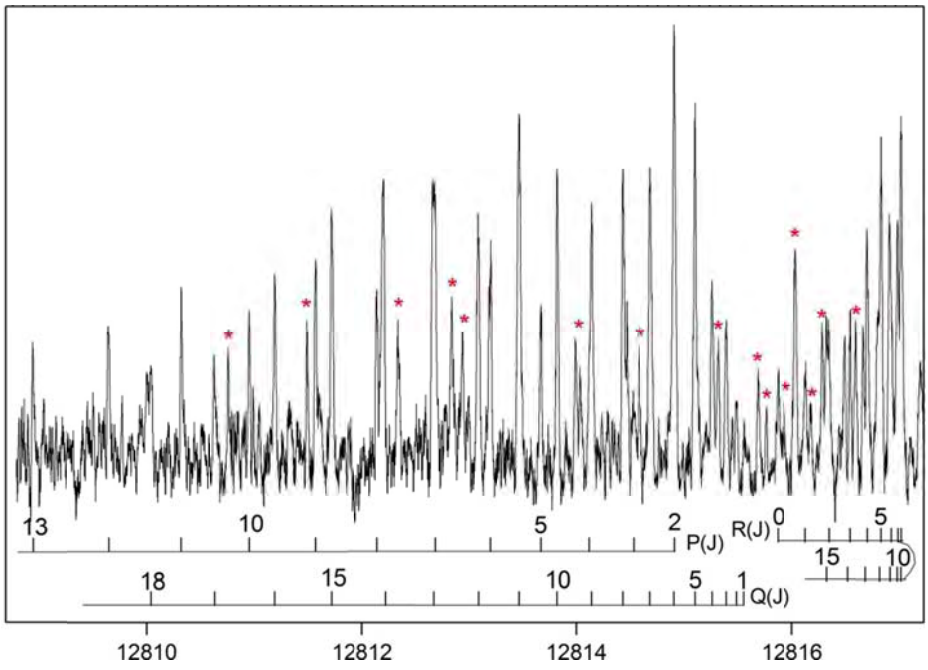

Figure 6.3 The (v+1,0) band of the $[12.3]^1\Pi_1$- $X^1\Sigma^+$ transition of IrP.

(2) The two triplet transition systems at 13359 cm^{-1} and 13553 cm^{-1}

Two bands observed at 13359 cm^{-1} and 13553 cm^{-1} are assigned to triplet transitions. For the one with band head located at 13359 cm^{-1}, resolved P, Q and R branches were observed with the first line of each branch tentatively assigned to P(3), Q(2) and R(2) respectively. While this band was tentatively analyzed to be a $\Omega=2\leftarrow2$ transition, there may be some uncertainty in the assignment due to the uncertainty in the position of the first lines of the branches as a result of low signal-to-noise ratio. It was found that the molecules primarily populated in the v=0 level of the low lying electronic states due to low temperature resulting from jet-cooling. This band is therefore preliminarily assigned to a (v,0) band, while the upper vibrational number v cannot be determined with limited information to date. The observed spectrum is shown in Figure 6.4, in which bands of both ^{193}IrP and ^{191}IrP were identified. The derived molecular constants are listed in Table 6.1.

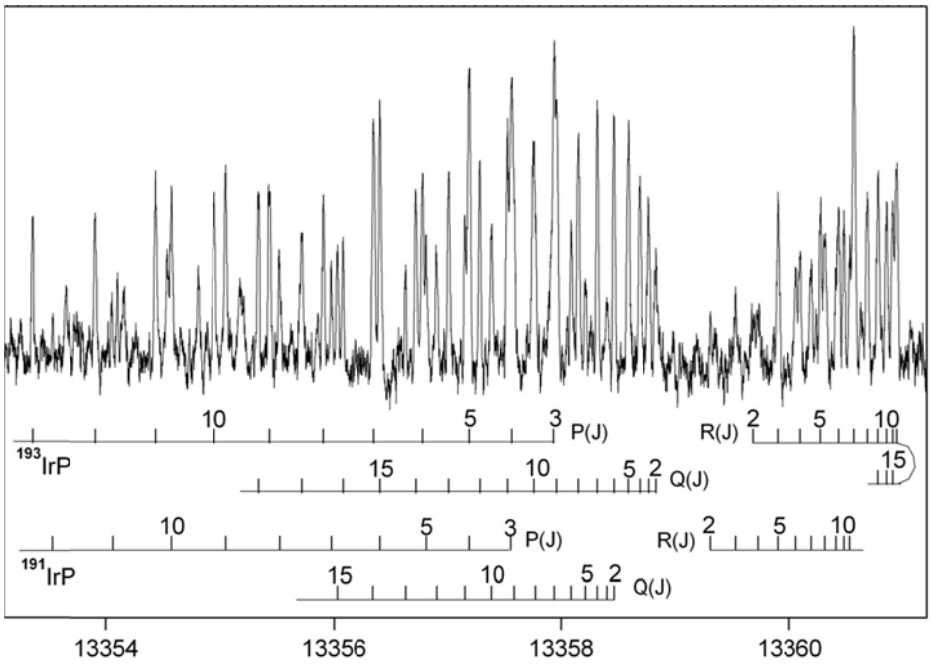

Figure 6.4 The band with band head located at 13359 cm^{-1} of IrP.

For the band with band head located at 13553 cm^{-1}, resolved P, Q and R branches were observed with the first line of each branch assigned to P(4), Q(3) and R(2) respectively. Once again the tentative assignment of a $\Omega=3\leftarrow2$ transition for this band may have some uncertainty as a result of the low signal-to-noise ratio. This band is also preliminarily assigned to a (v,0) band with unidentified upper vibrational number v and electronic states. As shown in Figure 6.5, lines of both ^{193}IrP and ^{191}IrP are well identified in the observed spectrum. The fitted molecular constants are listed in Table 6.1.

As seen in Table 6.1, rotational constants of the lower states of both two bands are very close, so it is very likely that these two bands come from the same lower electronic states and their upper states may belong to different sub states of the same triplet state. It is obvious that further experimental investigation is necessary to have a definite assignment of the electronic states involved.

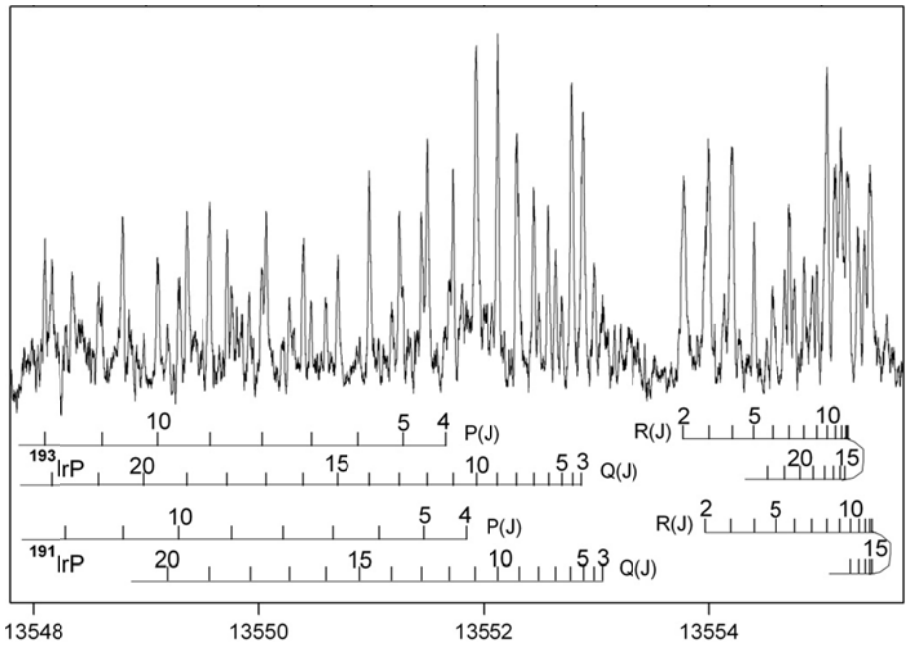

Figure 6.5 The band with band head located at 13553 cm^{-1} of IrP.

(3) The perturb band at 12708 cm^{-1}

The high resolution spectrum of the band observed at 12708 cm^{-1} is shown in Figure 6.6. While rotational structure was clearly shown for the P, Q and R branches, the assignment of the first line of each band may be uncertain. Assuming the first lines of each branch are P(2), Q(1) and R(0) as tentatively assigned, this band is likely due to the $[12.7]^1\Pi_1$ - $X^1\Sigma^+$ transition as the estimated rotational constant in the lower state is close to that in the ground state. Lines from both ^{193}IrP and ^{191}IrP were observed in the spectrum. However, the least-squares fitting of the assigned transition was not converged because of possible perturbation. Since no perturbation has been reported for the ground state, we defer the perturbation might be from the upper state. As shown in Figure 6.7**,** the plot of reduced term value against J(J+1) of upper state for both ^{193}IrP and ^{191}IrP indicates that there may be perturbation in the low J levels. For a more detailed analysis of the perturebation, more experimental work is on the way.

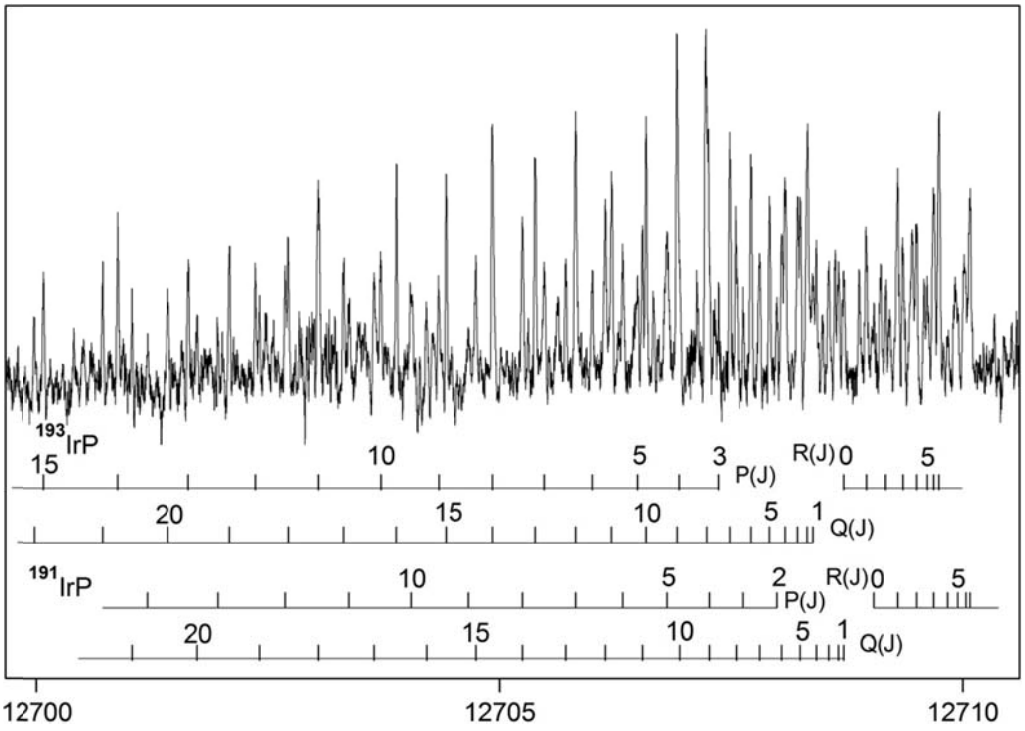

Figure 6.6 The perturbed band with band head located at 12708 cm^{-1} of IrP.

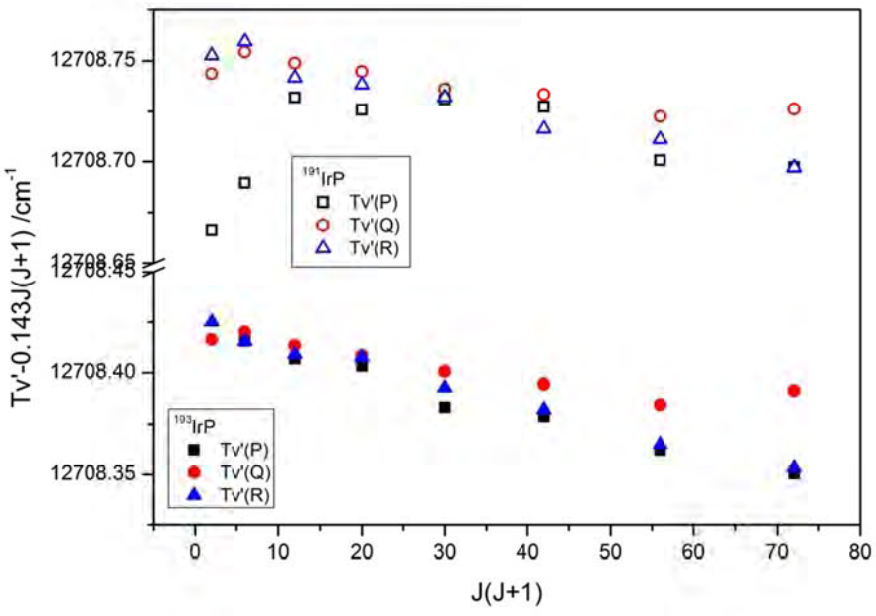

Figure 6.7 Reduced term value plot against J(J+1) of ^{193}IrP and ^{191}IrP of the perturbed band at 12708 cm^{-1} of IrP.

Table 6.1 Molecular constants of observed transitions of IrP (cm^{-1}).

		^{193}IrP		^{191}IrP	
Band system	v	T_0	B	T_0	B
13553 cm^{-1} band	v’	b+13552.981	0.141549(22)	b+13553.170	0.141960(44)
	0’’	b	0.151077(22)	b	0.151437(42)
13359 cm^{-1} band	v’	a+13358.897	0.140235(23)	a+13358.524	0.140484(41)
	0’’	a	0.150606(22)	a	0.150869(38)
$[12.3]^1\Pi_1$ - $X^1\Sigma^+$	v+1’	12815.580	0.143026(5)		
	v’	12337.200	0.143431(4)		
	0’’	0	0.159035*		

* value fixed from Ref[74].

6.1.4 Summary

In our preliminary study of IrP, a few low lying electronic systems were newly observed, including the $[12.3]^1\Pi_1$- $X^1\Sigma^+$ system, two triplet transition systems, and the perturbed possible the $[12.7]^1\Pi_1$ - $X^1\Sigma^+$ system. Although only one or two bands were recorded for each transition system due to the low transition intensities, these observation are consistent with the calculations based on MRCI by Adam et al.[74] According to their calculations, two lowest $^1\Pi$ states (labeled $1^1\Pi$ and $2^1\Pi$) lie above the ground state with observable transition intensities together with the two lowest lying triplet states $1^3\Pi$ and $1^3\Phi$ both belong to the $\delta^3\pi$ configuration were predicted. These four states may be accounted for the four observed band systems. In addition, a predicted crossover the potential curves of $2^1\Pi$ and $1^1\Delta$ is also consistent with our observed perturbation in the band located at 12708 cm^{-1}.

The Λ-type doubling was not observed in any band system recorded in our spectrum. It may be due to the broad line width of about 0.03 cm^{-1} (FWHM) in the transition. The width appeared to be Doppler-limited according to the cooling effect of the expansion. It will be interesting to investigate the magnitude of Λ-doubling using a cooler source. However, this can only be achieved with a modified supersonic nozzle and pumping system.

6.2 Laser induced fluorescence spectrum of IrB

6.2.1 Background

Metal borides possess a lot of attractive properties, most of which are refractory materials with exceeding hardness and excellent conductivity.[76-81] It has been recently reported that ReB2 bulk[80] and RhB and IrB films[81] have super-hardness properties. In addition, MgB_2[77,78] was found to be a superconductor at very low temperature. In addition, many transition metal borides are known to be good catalysts for hydrogenation of alkenes and alkynes, deoxygenation reactions, etc.[82] Iridium compounds are also very important catalysts in the formation of carbon-hydrogen and carbon-oxygen bonds.[83] Following our study of IrP, we also search for electronic transitions of IrB in the near infrared region. IrB was first experimentally observed in the visible region by Pang et al. in 2008.[6] In a later work, they found several more electronic transitions of IrB involving ground and low-lying states.[84] In our study, a new electronic transition from the ground state was observed and analyzed for $^{193}Ir^{11}B$ and $^{191}Ir^{11}B$. Spectroscopic constants were also derived from the least-squares fitting of the observed transitions.

6.2.2 Experimental conditions

IrB molecules were produced by reacting laser ablated iridium vapor with diborane (B_2H_6) gas followed by supersonic free jet expansion. The experimental conditions of IrB were very similar to those for IrP except that the 1% PH_3 in argon gas mixture was replaced by a mixture of 0.5% B_2H_6 in argon. LIF spectrum at medium resolution in the region of 12000 – 14000 cm^{-1} was scanned and two bands at 12320 cm^{-1} and 13073 cm^{-1} have been studied using high resolution LIF spectroscopy to date.

6.2.3 Results and analysis

Laser induced fluorescence spectrum of IrB in the region of 12000 - 14000 cm^{-1} has been recorded at moderate resolution. As shown in Figure 6.8, 3 transition bands were observed. High resolution scans have been carried out for the bands at 12320 cm^{-1} and 13073 cm^{-1} to date. In our preliminary assignment, these two bands are tentatively assigned to a $^3\Delta_3$-$X^3\Delta_3$ transition. Among the four isotopomers due to the isotopes of iridium and boron elements, namely, ^{191}Ir (37.3%), ^{193}Ir (62.7%) and ^{10}B (19.9%), ^{11}B (80.1%) respectively, only two isotopic species $^{191}Ir^{11}B$ and $^{193}Ir^{11}B$ were observed in our spectrum.

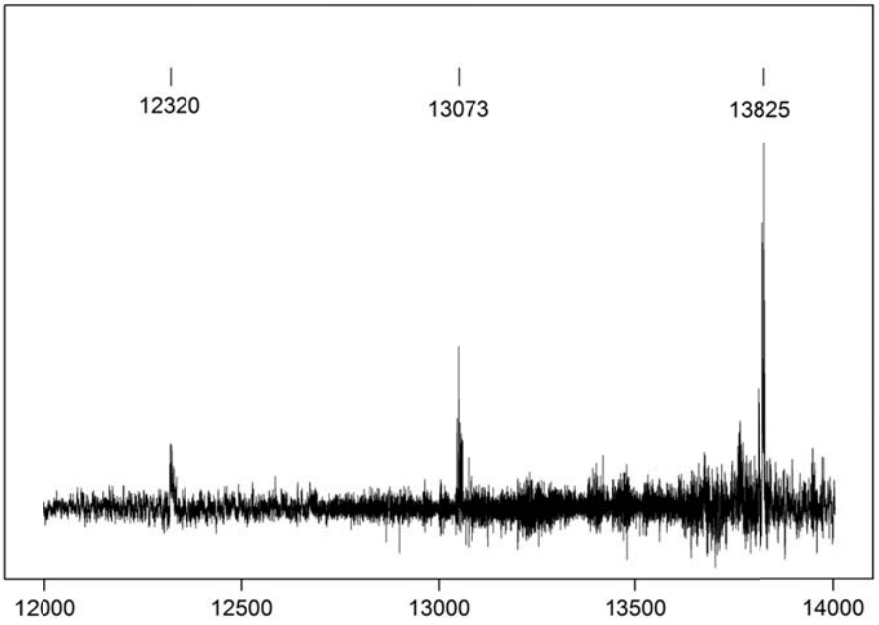

Figure 6.8 Broadband scan between 12000 and 14000 cm^{-1} of IrB.

The $[12.3]^3\Delta_3$-$X^3\Delta_3$ transition

Two vibrational bands originated at 12320 cm^{-1} and 13073 cm^{-1} have been analyzed for the $[12.3]^3\Delta_3$-$X^3\Delta_3$ transition system. Each vibrational band exhibited resolved P, Q and R branches with first line of each branch assigned to P(4), Q(3) and R(3) respectively, unambiguously confirmed $\Omega' = 3$ and $\Omega'' = 3$ values for the electronic states involved. Furthermore, the strong intensities of P and R branches were also consistent with a $\Delta\Lambda=0$ transition. The band at 12320 cm^{-1} and 13073 cm^{-1} are shown in Figure 6.9 and Figure 6.10, respectively. As shown in the spectra, only

transitions of $^{191}Ir^{11}B$ and $^{193}Ir^{11}B$ were assigned. Rotational line positions of each band were fit to the following expression:

$$\nu = \nu_0 + B'J'(J'+1) - D'[J'(J'+1)]^2 - \{B''J''(J''+1) - D''[J''(J''+1)]^2\}, \quad (62)$$

with constants carrying usual meaning as explained before. In the least-squares fitting, the centrifugal distortion constant was set to zero since only low J lines were involved. The molecular constants for v=0 level of the ground $X^3\Delta_3$ state were fixed to those found in literature. The fitted molecular constants are listed in Table 6.2. Based on the fitted constants, these two bands were preliminarily assigned to the (v,0) and (v+1,0) bands at 12320 cm^{-1} and 13073 cm^{-1} of the $[12.3]^3\Delta_3$ - $X^3\Delta_3$ transition. With only two rovibronic bands observed, it is impossible to make a definite assignment for the vibrational number v. according to the vibrational separation between the observed bands, the band at 13825 cm^{-1} may belong to the (v+2,0) band of the same transition system.

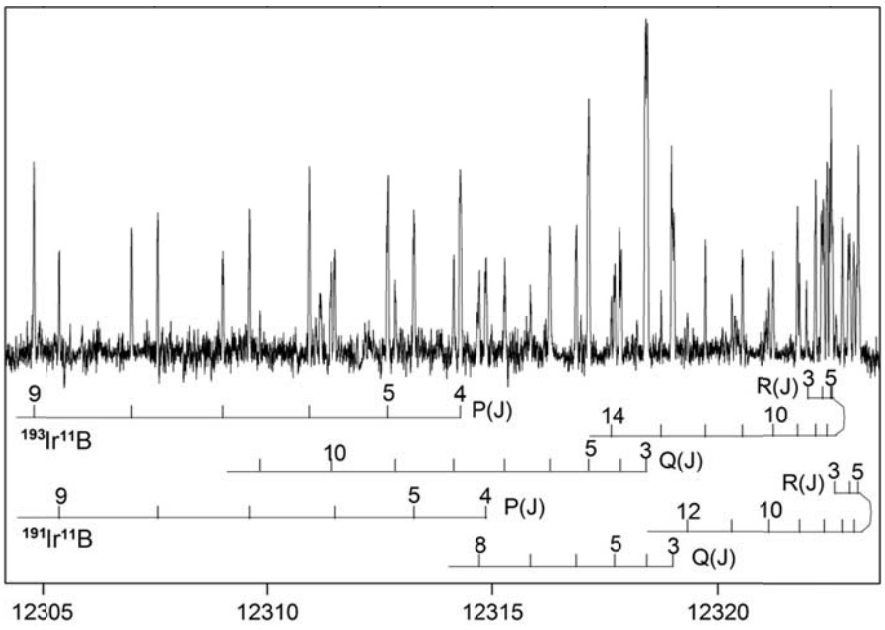

Figure 6.9 The (v,0) band of the $[12.3]^3\Delta_3$-$X^3\Delta_3$ transition of IrB.

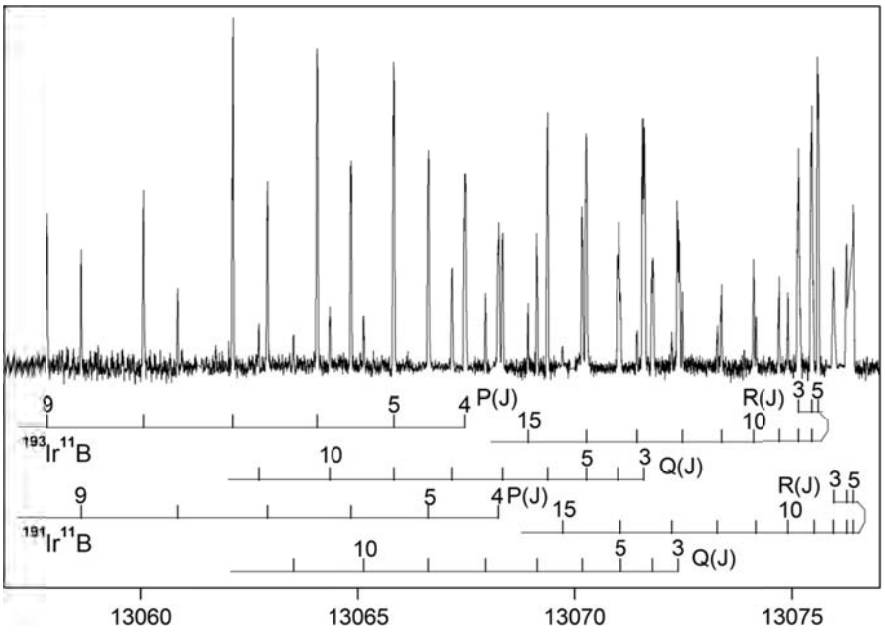

Figure 6.10 The (v+1,0) band of the $[12.3]^3\Delta_3$-$X^3\Delta_3$ transition of IrB.

Table 6.2 Molecular constants of the $[12.3]^3\Delta_3$-$X^3\Delta_3$ transition of IrB (cm^{-1}).

		$^{193}Ir^{11}B$		$^{191}Ir^{11}B$	
Band system	v	T_0	B	T_0	B
$[12.3]^3\Delta_3$-$X^3\Delta_3$	v+1'	13072.489	0.444062(7)	13073.283	0.444317(8)
	v'	12319.289	0.446474(10)	12319.874	0.446733(11)
	0''	0	0.51809*	0	0.51839*

*:value fixed from ref[84].

6.2.4 Discussion

As shown in Figure 6.11, the typical line width observed for IrB was unusually large that may be ascribed to the partially resolved hyperfine structure. Since both ^{191}Ir(I=3/2, μ/μ_N=0.146) and ^{193}Ir(I=3/2, μ/μ_N=0.159) posess small nuclear magnetic moments while the ^{11}B(I=3/2, μ/μ_N=2.689) atom has a much larger nuclear magnetic moment,[66] it is expected that the hyperfine structure should be dominated by the ^{11}B atom. As shown in Figure 6.11, the rapid decrease in line width with increasing J value indicates the Hund's case a_β coupling scheme for the hyperfine coupling.

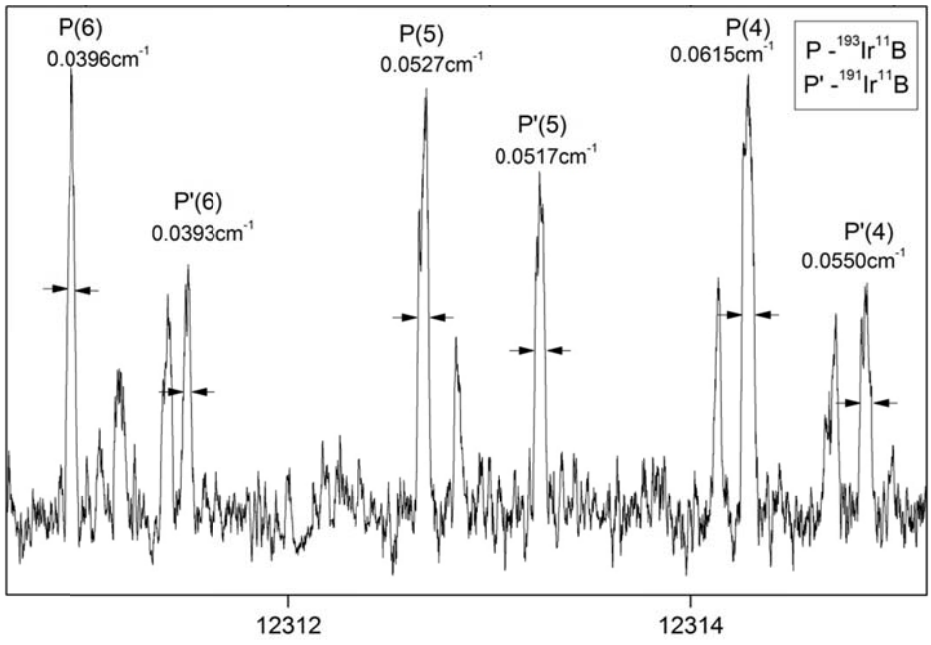

Figure 6.11 The (v,0) band of the $[12.3]^3\Delta_3$-$X^3\Delta_3$ transition of IrB with partially resolved hyperfine structure.

Based on the qualitative MO energy diagram of IrB given by Pang et al.[6] as shown in Figure 6.12. The ground electronic state is correlated to the $\delta^3\sigma$ configuration as shown below:

IrB: $(1\sigma)^2(1\pi)^4(1\delta)^3(2\sigma)^1 \rightarrow {}^1\Delta$ and $X^3\Delta_i$.

With one electron excited from 2σ to 3σ orbital, two low-lying electronic states $^1\Delta$ and $^3\Delta_i$ are formed:

IrB: $(1\sigma)^2(1\pi)^4(1\delta)^3(3\sigma)^1 \rightarrow {}^1\Delta$ and $^3\Delta_i$.

With two electrons excited from $(1\delta)^3(2\sigma)^1$ to $(1\delta)^2(2\pi)^2$, various electronic states are formed as listed below:

IrB: $(1\sigma)^2(1\pi)^4(1\delta)^2(2\pi)^2 \rightarrow {}^1\Sigma^+(2)$, $^3\Sigma^-(2)$, $^5\Sigma^+$, $^1\Delta(2)$, $^3\Delta_i$, $^1\Gamma$ and $^1\Lambda$=6.

So the energy of these orbitals are expected to be very close and accurate theoretical calculations have yet to be done, the excited $^3\Delta_i$ electronic states observed in our spectrum may correlate to the electronic configurations $\delta^3\sigma$ and $\delta^2\pi^2$. Nevertheless, the limited information at hand to date has prevented us to draw a definite conclusion.

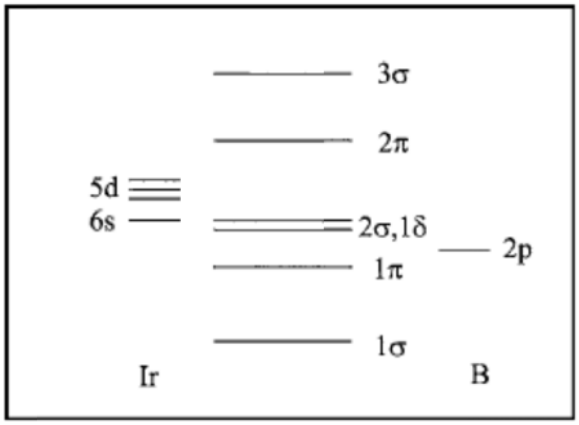

Figure 6.12 MO energy level diagram of IrB.

6.3 Summary

In this chapter, we discussed our preliminary LIF study of IrP and IrB in the 12000-14000 cm^{-1} region. In the case of IrP, the four transition systems observed are consistent with the low-lying states predicted by Adams et al. In the case of IrB, the $[12.3]^3\Delta_3$-$X^3\Delta_3$ transition system has been observed and analyzed. The exact excited electronic state with the electronic configuration cannot be determined because of limited information obtained from experiments. For both molecules, isotopomers due to isotopes of iridium have been observed. Further experiments on improving the S/N ratio and extending the frequency coverage of the spectra are underway.

Chapter 7 **Concluding remarks**

In this thesis, we reported our studies of solid hydrogen and gaseous diatomic transition-metal compounds using infrared laser spectroscopy. In both cases, the advantages of high resolution afforded by laser sources have been fully exploited to observe the fine details in the spectra. In the case of solid hydrogen, not only we observed the crystal field splitting of the W (ΔJ=6) transitions but also the temperature effect on the transitions were investigated. These results provide a wealth of new information on the relaxation mechanism for further theoretical studies. While the signal-to-noise ratio of our spectra may not be satisfactory, it does demonstrate the great impact of high resolution spectroscopy.

In studying the electronic structure of transition metal compounds, near infrared high resolution LIF spectroscopy was combined with the technique of laser ablation/reaction followed by free expansion to obtain rovibronic spectra of RuC, IrP and IrB molecules. In these spectra, not only the isotropic species have been identified but also the hyperfine structure was observed as a result of Doppler-limited resolution achieved. While the analysis of the spectra is still not completed and more experiments are underway, there is no doubt that a number of new electronic states of the species have been found that will provide crucial information for testing the accuracy of high level *ab initio* calculations.

Comparing to other spectroscopic techniques, high resolution spectroscopy is relatively simple in experiment setup and more cost effective. Applying appropriate modulation/detection technique, it can achieve excellent sensitivity that can be extremely useful in detecting species at low concentration and short lifetime as illustrated in the work discussed here. The advancement of laser technology will no doubt play crucial role in its future development.

Reference

(1) Linton, C.; Zhuang, X.; Steimle, T. C.; Adam, A. G. *J. Chem. Phys.* **2011**, *135*.

(2) Ran, Q.; Tam, W. S.; Cheung, A. S. C.; Merer, A. J. *J. Mol. Spectrosc.* **2003**, *220*, 87.

(3) Momose, T.; Uchida, M.; Sogoshi, N.; Miki, M.; Masuda, S.; Shida, T. *Chem. Phys. Lett.* **1995**, *246*, 583.

(4) Hoshina, H.; Fushitani, M.; Momose, T. *J. Mol. Spectrosc.* **2011**, *268*, 164.

(5) Gudeman, C. S.; Begemann, M. H.; Pfaff, J.; Saykally, R. J. *Phys. Rev. Lett.* **1983**, *50*, 727.

(6) Ye, J.; Pang, H. F.; Wong, A. M.-Y.; Leung, J. W.-H.; Cheung, A. S.-C. *J. Chem. Phys.* **2008**, *128*.

(7) J. C. McLennan, J. A. M. *Nature* **1929**, *123*, 160.

(8) Van Kranendonk, J. *Solid Hydrogen, Theory of the Properties of Solid H2, HD, and D2*; Plenum Press: New York, **1983**.

(9) Silvera, I. F. *Rev. Mod. Phys.* **1980**, *52*, 393.

(10) Van Kranendonk, J.; Karl, G. *Rev. Mod. Phys.* **1968**, *40*, 531.

(11) Chan, M.; Lee, S.; Okumura, M.; Oka, T. *J. Chem. Phys.* **1991**, *95*, 88.

(12) Chan, M. C.; Song, Y.; Yan, L. *Chem. Phys. Lett.* **2009**, *468*, 166.

(13) Momose, T.; Weliky, D. P.; Oka, T. *J. Mol. Spectrosc.* **1992**, *153*, 760.

(14) Kerr, K. E.; Momose, T.; Weliky, D. P.; Gabrys, C. M.; Oka, T. *Phys. Rev. Lett.* **1994**, *72*, 3957.

(15) Kuroda, K.; Koreeda, A.; Takayanagi, S.; Suzuki, M.; Hakuta, K. *Phys. Rev. B* **2003**, *67*, 184303.

(16) Zhang, Y.; Byers, T. J.; Chan, M. C.; Momose, T.; Kerr, K. E.; Weliky, D. P.; Oka, T. *Phys. Rev. B: Condens. Matter* **1998**, *58*, 218.

(17) Dickson, R.; Momose, T.; Byers, T.; Oka, T. *Phys. Rev. B: Condens. Matter* **1998**, *57*, 941.

(18) Veillard, A. *Chem. Rev.* **1991**, *91*, 743.

(19) Koga, N.; Morokuma, K. *Chem. Rev.* **1991**, *91*, 823.

(20) Rao, C. N. R. *Annu. Rev. Phys. Chem.* **1989**, *40*, 291.

(21) Wojciechowska, M.; Haber, J.; Łomnicki, S.; Stoch, J. *J. Mol. Catal. A: Chem.* **1999**, *141*, 155.

(22) Rosenblatt, G. M. *High Temperature Science: Future Needs and Anticipated Developments*; National Academy of Science: Washington.D.C, **1979**.

(23) Carlson, K. D.; Claydon, C. R. In *Advances in High Temperature Chemistry*; Leroy, E., Ed.; Elsevier: **1967**; Vol. Volume 1, p 43.

(24) Weltner, W. *Science* **1967**, *155*, 155.

(25) N. M. White, R. F. W. *Astrophys. J.* **1978**, *222*, 209.

(26) C. W. Bauschlicber, S. P. W., S. R. Langhoff *Quantum Chemistry; The Challenge of Tranition Metals and Chemistry*; NATO Advanced Studies Institute **1986**.

(27) Merer, A. J. *Annu. Rev. Phys. Chem.* **1989**, *40*, 407.

(28) Dietz, T. G.; Duncan, M. A.; Powers, D. E.; Smalley, R. E. *J. Chem. Phys.* **1981**, *74*, 6511.

(29) Demtröder, W. *Laser Spectrosocpy*; 4th ed.; Springer: Verlag Berlin Heidelberg, **2008**.

(30) Landau, L. D.; Lifshitz, E. M. *Quantum Mechanics: Non-Relativistic Theory*; 3rd ed.; Pergamon: New York, 1977.

(31) Born, M.; Oppenheimer, R. *Annalen der Physik* **1927**, *389*, 457.

(32) Levine, I. N. *Molecular Spectroscopy*; Wiley: New York, **1975**.

(33) Herzberg, G. *Spectra of Diatomic Molecules*; 2nd ed.; D. Van Nostrand Company: Princeton, New Jersey, 1950.

(34) Shen, Y.-R. *Nonlinear Infrared Generation*; Springer: Berlin, Heidelberg, **1977**.

(35) Chou, M. H.; Hauden, J.; Arbore, M. A.; Fejer, M. M. *Opt. Lett.* **1998**, *23*, 1004.

(36) Ran, Q.; Tam, W. S.; Ma, C.; Cheung, A. S. C. *J. Mol. Spectrosc.* **1999**, *198*, 175.

(37) Oka, T. *Annu. Rev. Phys. Chem.* **1993**, *44*, 299.

(38) Weliky, D. P.; Kerr, K. E.; Byers, T. J.; Zhang, Y.; Momose, T.; Oka, T. *J. Chem. Phys.* **1996**, *105*, 4461.

(39) Mulder, F.; Van der Avoird, A.; Wormer, P. *Mol. Phys.* **1979**, *37*, 159.

(40) Fajardo, M.; Tam, S.; DeRose, M. *J. Mol. Struct.* **2004**, *695*, 111.

(41) Fajardo, M. E.; Lindsay, C. M.; Momose, T. *J. Chem. Phys.* **2009**, *130*.

(42) Tam, S.; Fajardo, M. E. *J. Low Temp. Phys.* **2000**, *26*, 653.

(43) Abouaf-Marguin, L.; Vasserot, A. M. *J. Low Temp. Phys.* **2011**, *37*, 357.

(44) Toda, N.; Mizoguchi, A.; Kanamori, H. *J. Chem. Phys.* **2010**, *132*, 234504.

(45) Momose, T.; Hoshina, H.; Fushitani, M.; Katsuki, H. *Vib. Spectrosc.* **2004**, *34*, 95.

(46) Skinner, J. L.; Hsu, D. *J. Phys. Chem.* **1986**, *90*, 4931.

(47) Song, Y. Ph.D, The Chinese University of Hong Kong, 2009.

(48) Yan, L. Ph.D, The Chinese University of Hong Kong, 2011.

(49) Miller, R. E.; Decius, J. C. *J. Chem. Phys.* **1973**, *59*, 4871.

(50) Balasubramanian, T.; D'souza, R.; D'Cunha, R.; Rao, K. *Can. J. Phys.* **1989**, *67*, 79.

(51) Souers, P. C. *Hydrogen Properties for Fusion Energy* : University of California Press, **1986**.

(52) Scullman, R.; Thelin, B. *Phys. Scr.* **1971**, *3*, 19.

(53) Scullman, R.; Thelin, B. *Phys. Scr.* **1972**, *5*, 201.

(54) Langenberg, J. D.; Dabell, R. S.; Shao, L.; Dreessen, D.; Morse, M. D. *J. Chem. Phys.* **1998**, *109*, 7863.

(55) Shim, I.; Gingerich, K. A. *Chem. Phys. Lett.* **2000**, *317*, 338.

(56) DaBell, R. S.; Meyer, R. G.; Morse, M. D. *J. Chem. Phys.* **2001**, *114*, 2938.

(57) Steimle, T. C.; Virgo, W. L.; Brown, J. M. *J. Chem. Phys.* **2003**, *118*, 2620.

(58) Guo, R.; Balasubramanian, K. *J. Chem. Phys.* **2004**, *120*, 7418.

(59) Virgo, W. L.; Steimle, T. C.; Aucoin, L. E.; Brown, J. M. *Chem. Phys. Lett.* **2004**, *391*, 75.

(60) Fang Wang, A. D. A., T.C. Steimle In *68th Ohio State University International Symposium on Molecular Spectroscopy* **2013**.

(61) Shim, I.; Finkbeiner, H. C.; Gingerich, K. A. *J. Phys. Chem.* **1987**, *91*, 3171.

(62) Herzberg, G. *Atomic Spectra and Atomic Structure*; Dover: New York, **1944**.

(63) Frosch, R. A.; Foley, H. M. *Phys. Rev.* **1952**, *88*, 1337.

(64) Azuma, Y.; Barry, J. A.; Lyne, M. P. J.; Merer, A. J.; Schröder, J. O.; Féménias, J. L. *J. Chem. Phys.* **1989**, *91*, 1.

(65) I. M. Mills, T. C., K. Homann, N. Kallay, K. Kuchitsu; Blackwell Scientific Publ.: Oxford, **1993**.

(66) Weltner, W. *Magnetic Atoms and Molecules*; Van Nostrand Reinhold: New York, **1983**.

(67) Varberg, T. D.; Field, R. W.; Merer, A. J. *J. Chem. Phys.* **1991**, *95*, 1563.

(68) R.H. Grubbs, T. M. T. In *Ruthenium in Organic Synthesis*; Murahashi, S.-I., Ed.; Wiley-VCH: Germany, **2004**.

(69) B. Aronsson, T. L., S. Rurdquist *Borides, Silicides and Phosphides*; John Wiley and Sons: New York, **1965**.

(70) Corbridge, D. E. C. *Phosphorous 2000 - Chemistry, Biochemistry and Technology*; Elsevier: New York, **2000**.

(71) Jansson, K.; Scullman, R. *Berichte der Bunsengesellschaft für physikalische Chemie* **1978**, *82*, 92.

(72) Marr, A. J.; Flores, M. E.; Steimle, T. C. *J. Chem. Phys.* **1996**, *104*, 8183.

(73) Adam, A. G.; Granger, A. D.; Downie, L. E.; Tokaryk, D. W.; Linton, C. *Can. J. Phys.* **2009**, *87*, 557.

(74) Adam, A. G.; Downie, L. E.; Granger, A. D.; Grein, F.; Slaney, M. E.; Linton, C.; Tokaryk, D. W. *J. Mol. Spectrosc.* **2010**, *263*, 111.

(75) Pang, H. F.; Liu, A.; Xia, Y.; Cheung, A. S. C. *Chem. Phys. Lett.* **2010**, *494*, 155.

(76) Trenary, M. *Materials Science of Carbides, Nitrides and Borides*; Kluwer Academic: Dordrecht, **1998**; Vol. 68.

(77) Nagamatsu, J.; Nakagawa, N.; Muranaka, T.; Zenitani, Y.; Akimitsu, J. *Nature* **2001**, *410*, 63.

(78) Choi, H. J.; Roundy, D.; Sun, H.; Cohen, M. L.; Louie, S. G. *Nature* **2002**, *418*, 758.

(79) Will, G. *J. Solid State Chem.* **2004**, *177*, 628.

(80) Chung, H. Y.; Weinberger, M. B.; Levine, J. B.; Kavner, A.; Yang, J. M.; Tolbert, S. H.; Kaner, R. B. *Science* **2007**, *316*, 436.

(81) Latini, A.; Rau, J. V.; Teghil, R.; Generosi, A.; Albertini, V. R. *ACS Appl. Mater. Interfaces* **2010**, *2*, 581.

(82) Ciriano, M. A.; Lopez, J. A.; Oro, L. A.; Perez-Torrente, J. J.; Lanfranchi, M.; Tiripicchio, A.; Camellini, M. T. *Organometallics* **1995**, *14*, 4764.

(83) Osby, J. O.; Heinzman, S. W.; Ganem, B. *J. Am. Chem. Soc.* **1986**, *108*, 67.

(84) Pang, H. F.; Ng, Y. W.; Xia, Y.; Cheung, A. S. C. *Chem. Phys. Lett.* **2011**, *501*, 257.

Appendix 1 Line list of RuC

Assigned rotational lines of the $[12.7]^3\Pi_2$-$[0.1]^3\Delta_3$ transition

^{96}RuC

	(1, 1)		
J	P	Q	R
3	12592.2097		12600.1929
4	12590.9433		12601.2002
5	12589.6444		12602.1825
6	12588.3143		12603.1321
7	12586.9521		
8	12585.5588	12594.6768	12604.9339
9	12584.1332		
10	12582.6747		
11	12581.1886		

	(2, 2)		
J	P	Q	R
3	12529.1963	12532.5924	
4	12527.9312		12538.1047
5	12526.6269	12532.2846	12539.0660
6	12525.3005		12539.9933
7	12523.9272		12540.8864
8	12522.5296		12541.7354

	(1, 0)		
J	P	Q	R
3	13625.1087	13628.5268	13633.0855
4	13623.8112	13628.3690	13634.0665
5	13622.4687	13628.1739	13635.0100
6	13621.0977	13627.9366	13635.9134
7	13619.6854	13627.6617	13636.7772
8	13618.2290	13627.3438	13637.6024
9	13616.7337	13626.9873	13638.3864
10	13613.6276	13626.5903	13639.1301
11	13612.0148		
12	13610.3634		
13	13608.6720		
14	13625.1087		

^{98}RuC

(1, 1)			
J	P	Q	R
3	12592.3011		
4	12591.0352		
5	12589.7439		12602.2518
6			12603.1995
7			
8			12604.9979
9			12605.8483
10			12606.6691

(1, 0)			
J	P	Q	R
3		13627.4482	13631.9959
4	13622.7435	13627.2907	13632.9777
5	13621.4077	13627.0930	13633.9176
6	13620.0367		
7	13618.6259		

^{99}RuC

(1, 0)				
J	F	P	Q	R
3	5.5		13626.9867	13631.5302
	4.5		13626.9459	13631.4909
	3.5		13626.9146	13631.4593
	2.5		13626.8897	13631.4350
	1.5		13626.8741	13631.4171
	0.5		13626.8636	13631.4071
4	6.5	13622.2756	13626.8186	13632.4974
	5.5	13622.2462	13626.7903	13632.4695
	4.5	13622.2214	13626.7673	13632.4472
	3.5	13622.2051	13626.7485	13632.4289
	2.5	13622.1908	13626.7349	13632.4147
	1.5	13622.1793	13626.7242	13632.4037
5	7.5	13620.9371	13626.6150	13633.4307
	6.5	13620.9153	13626.5947	13633.4096
	5.5	13620.8971	13626.5769	13633.3910
	4.5	13620.8814	13626.5600	13633.3759
	3.5	13620.8681	13626.5480	13633.3630
	2.5	13620.8582	13626.5378	13633.3532
6	8.5	13619.5603	13626.3750	13634.3259
	7.5	13619.5438	13626.3580	13634.3085
	6.5	13619.5284	13626.3430	13634.2943
	5.5	13619.5149	13626.3301	13634.2804
	4.5	13619.5047	13626.3191	13634.2705
	3.5	13619.4946	13626.3108	13634.2610
7	9.5	13618.1466	13626.0972	13635.1829
	8.5	13618.1318	13626.0829	13635.1681
	7.5	13618.1193	13626.0701	13635.1565
	6.5	13618.1070	13626.0584	13635.1456
	5.5	13618.0981	13626.0495	13635.1350
	4.5	13618.0899	13626.0404	13635.1265
8	10.5	13616.6931	13625.7803	13636.0019
	9.5	13616.6805	13625.7680	13635.9907
	8.5	13616.6702	13625.7566	13635.9787
	7.5	13616.6600	13625.7475	13635.9694
	6.5	13616.6513	13625.7381	13635.9609
	5.5	13616.6436	13625.7309	13635.9528
9	11.5	13615.2030	13625.4255	13636.7823
	10.5	13615.1924	13625.4138	13636.7716
	9.5	13615.1817	13625.4042	13636.7619
	8.5	13615.1728	13625.3954	13636.7530
	7.5	13615.1648	13625.3878	13636.7451
	6.5	13615.1578	13625.3809	13636.7381

10	12.5	13613.6727	13637.5243
	11.5	13613.6624	13637.5155
	10.5	13613.6537	13637.5056
	9.5	13613.6468	13637.4986
	8.5	13613.6387	13637.4908
	7.5	13613.6321	13637.4842
11	13.5	13612.1036	13638.2271
	12.5	13612.0944	13638.2183
	11.5	13612.0866	13638.2098
	10.5	13612.0795	13638.2026
	9.5	13612.0723	13638.1959
	8.5	13612.0667	13638.1906
12	14.5	13610.4956	
	13.5	13610.4885	
	12.5	13610.4808	
	11.5	13610.4737	
	10.5	13610.4675	
	9.5	13610.4618	
13	15.5	13608.8486	
	14.5	13608.8409	
	13.5	13608.8344	
	12.5	13608.8293	
	11.5	13608.8228	
	10.5	13608.8167	
14	16.5	13607.1628	
	15.5	13607.1561	
	14.5	13607.1499	
	13.5	13607.1440	
	12.5	13607.1387	
	11.5	13607.1333	
15	17.5	13605.4374	
	16.5	13605.4309	
	15.5	13605.4262	
	14.5	13605.4203	
	13.5	13605.4159	
	12.5	13605.4105	

^{100}RuC

(1, 1)			
J	P	Q	R
3	12592.3904	12595.7916	12600.3315
4	12591.1291	12595.6659	12601.3450
5	12589.8327	12595.5098	12602.3198
6	12588.5111		12603.2634
7	12587.1533	12595.0973	12604.1735
8	12585.7679	12594.8442	12605.0558
9	12584.3472	12594.5589	12605.9058
10	12582.8959	12594.2408	12606.7220
11	12581.4129	12593.8905	12607.5089
12		12593.5141	12608.2554
13		12593.0971	12608.9753

(2, 2)			
J	P	Q	R
3	12529.5180		12537.3940
4	12528.2580	12532.7622	12538.3903
5	12526.9698	12532.5924	12539.3497
6	12525.6421	12532.3952	12540.2686
7	12524.2836	12532.1589	12541.1601
8	12522.8911	12531.8818	12542.0058
9	12521.4575		12542.8261
10	12519.9905		

	(1, 0)		
J	P	Q	R
3	13623.0110	13626.4122	13630.9530
4	13621.7187	13626.2546	13631.9305
5	13620.3876	13626.0606	13632.8683
6	13619.0174	13625.8225	13633.7683
7	13617.6078	13625.5509	13634.6262
8	13616.1600	13625.2364	13635.4469
9	13614.6717	13624.8838	13636.2268
10	13613.1461	13624.4904	13636.9703
11	13611.5802	13624.0601	13637.6726
12	13609.9753	13623.5875	13638.3349
13	13608.3307		13638.9579
14	13606.6489		
15	13604.9261		

	(2, 1)		
J	P	Q	R
3	13550.4761	13553.8585	13558.3611
4	13549.1928	13553.6952	13559.3208
5	13547.8621	13553.4901	13560.2433
6	13546.4924	13553.2458	13561.1179
7	13545.0800	13552.9515	13561.9547
8	13543.6236	13552.6236	13562.7501
9	13542.1281	13552.2477	13563.5009
10	13540.5873		
11	13539.0036		13564.8872

^{101}RuC

		(1, 0)		
J	F	P	Q	R
3	5.5		13625.9786	13630.5128
	4.5		13625.9313	13630.4668
	3.5		13625.8938	13630.4296
	2.5		13625.8636	13630.3996
	1.5		13625.8433	13630.3799
	0.5		13625.8303	13630.3675
4	6.5	13621.2763	13625.8099	13631.4784
	5.5	13621.2417	13625.7755	13631.4455
	4.5	13621.2132	13625.7475	13631.4184
	3.5	13621.1874	13625.7250	13631.3925
	2.5	13621.1690	13625.7084	13631.3754
	1.5	13621.1568	13625.6958	13631.3638
5	7.5	13619.9379	13625.6053	13632.4052
	6.5	13619.9114	13625.5803	13632.3791
	5.5	13619.8889	13625.5580	13632.3581
	4.5	13619.8707	13625.5391	13632.3401
	3.5	13619.8556	13625.5242	13632.3262
	2.5	13619.8438	13625.5122	13632.3136
6	8.5	13618.5631	13625.3652	13633.2982
	7.5	13618.5422	13625.3444	13633.2767
	6.5	13618.5238	13625.3270	13633.2585
	5.5	13618.5073	13625.3108	13633.2431
	4.5	13618.4946	13625.2969	13633.2309
	3.5	13618.4834	13625.2869	13633.2207
7	9.5	13617.1508	13625.0871	13634.1534
	8.5	13617.1335	13625.0697	13634.1357
	7.5	13617.1179	13625.0540	13634.1208
	6.5	13617.1047	13625.0407	13634.1077
	5.5	13617.0929	13625.0280	13634.0964
	4.5	13617.0829	13625.0180	13634.0860
8	10.5	13615.7019	13624.7696	13634.9676
	9.5	13615.6861	13624.7555	13634.9535
	8.5	13615.6729	13624.7420	13634.9404
	7.5	13615.6603	13624.7302	13634.9329
	6.5	13615.6498	13624.7201	13634.9296
	5.5	13615.6427	13624.7101	13634.9194
9	11.5	13614.2122	13624.4155	13635.7559
	10.5	13614.1995	13624.4021	13635.7335
	9.5	13614.1872	13624.3903	13635.7222
	8.5	13614.1767	13624.3799	13635.7124
	7.5	13614.1668	13624.3698	13635.7029
	6.5	13614.1585	13624.3610	13635.6949
10	12.5	13612.6853	13624.0217	13636.4871

	11.5	13612.6740	13624.0102	13636.4746
	10.5	13612.6635	13623.9995	13636.4644
	9.5	13612.6529	13623.9899	13636.4554
	8.5	13612.6440	13623.9810	13636.4446
	7.5	13612.6360	13623.9730	13636.4391
11	13.5	13611.1198		
	12.5	13611.1090		
	11.5	13611.0995		
	10.5	13611.0901		
	9.5	13611.0828		
	8.5	13611.0742		
12	14.5	13609.5152		
	13.5	13609.5060		
	12.5	13609.4964		
	11.5	13609.4883		
	10.5	13609.4812		
	9.5	13609.4748		
13	15.5	13607.8710		
	14.5	13607.8624		
	13.5	13607.8539		
	12.5	13607.8463		
	11.5	13607.8400		
	10.5	13607.8341		
14	16.5	13606.1888		
	15.5	13606.1799		
	14.5	13606.1725		
	13.5	13606.1662		
	12.5	13606.1602		
	11.5	13606.1535		
15	17.5	13604.4674		
	16.5	13604.4599		
	15.5	13604.4525		
	14.5	13604.4457		
	13.5	13604.4394		
	12.5	13604.4345		

^{102}RuC

(0, 0)			
J	P	Q	R
3	12654.7034	12658.1248	12662.6822
4	12653.4364	12657.9991	12663.6971
5	12652.1391	12657.8444	12664.6843
6	12650.8102	12657.6541	12665.6364
7	12649.4531	12657.4392	12666.5551
8	12648.0651	12657.1832	12667.4488
9	12646.6429	12656.9051	12668.3087
10	12645.1949	12656.5946	12669.1338
11	12643.7107	12656.2518	12669.9317
12	12642.1952	12655.8765	12670.6916
13	12640.6498	12655.4760	
14	12639.0765	12655.0339	

(1, 1)			
J	P	Q	R
3	12592.4757	12595.8718	12600.4015
4	12591.2180	12595.7465	12601.4108
5	12589.9258	12595.5887	12602.3823
6	12588.6038	12595.3986	12603.3247
7	12587.2496	12595.1792	12604.2377
8	12585.8657	12594.9256	12605.1151
9	12584.4492	12594.6391	12605.9610
10	12583.0003	12594.3216	12606.7771
11	12581.5214	12593.9745	12607.5579
12	12580.0100	12593.5932	12608.3106
13	12578.4670	12593.1817	12609.0271
14	12576.8911	12592.7382	12609.7147
15	12575.2857		
16	12573.6479		

(2, 2)			
J	P	Q	R
3	12529.6685	12533.0406	12537.5356
4	12528.4162		12538.5282
5	12527.1272	12532.7429	
6	12525.8036	12532.5408	12540.3974
7	12524.4483	12532.3066	
8	12523.0546	12532.0372	12542.1315
9	12521.6292	12531.7323	12542.9468
10	12520.1681	12531.3868	
11	12518.6684		

(1, 0)			
J	P	Q	R
3	13622.0224	13625.4149	13629.9485
4	13620.7313	13625.2614	13630.9244
5	13619.4041	13625.0665	13631.8593
6	13618.0364	13624.8328	13632.7563
7	13616.6311	13624.5567	13633.6147
8	13615.1848	13624.2433	13634.4326
9	13613.7005	13623.8903	13635.2109
10	13612.1762	13623.5003	13635.9510
11	13610.6150	13623.0707	13636.6545
12	13609.0142	13622.5982	13637.3104
13	13607.3736	13622.0899	
14	13605.6931	13621.5411	
15	13603.9744		
16	13602.216	13620.3247	
17	13600.4203		
18	13598.5852		

	(2, 1)		
J	P	Q	R
3	13549.5806	13552.9515	13557.4444
4	13548.2935	13552.7863	13558.4053
5	13546.9670	13552.5838	13559.3208
6	13545.6004	13552.3383	13560.1999
7	13544.1898	13552.0529	13561.0334
8	13542.7390	13551.7190	13561.8229
9	13541.2482	13551.3483	
10	13539.7098		
11	13538.1255		

^{104}RuC

(1, 1)			
J	P	Q	R
3	12592.5568	12595.9470	12600.4667
4	12591.2998	12595.8197	12601.4717
5	12590.0112	12595.6659	12602.4449
6	12588.6920	12595.4741	12603.3839
7	12587.3429	12595.2568	12604.2948
8	12585.9598	12595.0000	12605.1701
9	12584.5482	12594.7159	12606.0158
10	12583.0999	12594.3977	12606.8319
11	12581.6240	12594.0548	12607.6110
12	12580.1158	12593.6728	12608.3582
13	12578.5740	12593.2618	12609.0749
14		12592.8214	12609.7579
15			12610.4132
16	12573.7584		

(2, 2)			
J	P	Q	R
3	12529.8164	12533.1832	
4	12528.5616		12538.6576
5	12527.2750		12539.6100
6	12525.9598	12532.6848	12540.5227
7	12524.6039	12532.4441	
8	12523.2201	12532.1829	12542.2689
9	12521.7920	12531.8818	
10	12520.3337		
11	12518.8407		

(1, 0)			
J	P	Q	R
3	13621.0657	13624.4552	13628.9760
4	13619.7801	13624.2995	13629.9485
5	13618.4531	13624.1049	13630.8856
6	13617.0900	13623.8699	13631.7838
7	13615.6866	13623.5915	13632.6371
8	13614.2444	13623.2836	13633.4546
9	13612.7627	13622.9345	13634.2307
10	13611.2435	13622.5364	13634.9677
11	13609.6836	13622.1119	
12	13608.0868	13621.6444	
13	13606.4494	13621.1342	
14	13604.7726	13620.5872	
15	13603.0571	13620.0004	
16	13601.3021	13619.3751	
17	13599.5123	13618.7067	

(2, 1)			
J	P	Q	R
3	13548.7110	13552.0743	13556.5582
4	13547.4261	13551.9120	13557.5197
5	13546.1008	13551.7120	13558.4331
6	13544.7378	13551.4646	
7	13543.3314	13551.1768	13560.1448
8	13541.8849	13550.8482	13560.9297
9	13540.3961	13550.4761	
10	13538.8607		

Assigned rotational lines of the $[13.9]^3\Phi_4$-$[0.1]^3\Delta_3$ transition

^{96}RuC

(0, 0)			
J	P	Q	R
3			13824.3639
4		13819.6444	13825.3647
5	13813.7488	13819.4654	13826.3222
6	13812.3917	13819.2486	13827.2420
7	13810.9936	13818.993	13828.1349
8	13809.5566	13818.7017	13828.9833
9	13808.0878	13818.3716	13829.7947
10	13806.5824	13818.0069	13830.5748
11	13805.0392	13817.6064	
12	13803.4622	13817.1685	
13		13816.6959	

(1, 1)			
J	P	Q	R
3			13738.1574
4		13733.4693	13739.1416
5	13727.6127	13733.2798	13740.0895
6	13726.2515		13741.0003
7	13724.8588		13741.8731
8	13723.4241		13742.7092
9	13721.9570		13743.5066
10	13720.4496		13744.2656
11	13718.9085		13744.9912
12	13717.3242		

(0, 1)			
J	P	Q	R
3			12791.4691
4		12786.7801	12792.4963
5	12780.9220	12786.6347	12793.4938
6	12779.6079	12786.4647	12794.4612
7	12778.2621	12786.2628	12795.4013
8	12776.8924	12786.0305	12796.3139
9	12775.4880	12785.7702	
10		12785.4845	
11		12785.1627	12798.8738
12		12784.8159	12799.6677

^{98}RuC

(0, 0)			
J	P	Q	R
4		13819.6909	13825.3891
5		13819.5073	13826.3516
6	13812.4575	13819.2971	
7		13819.0431	
8		13818.7551	
9		13818.4305	

(1, 1)			
J	P	Q	R
3			13738.2911
4			13739.2667
5	13727.7656		13740.2139
6	13726.4097		13741.1200
7			13741.9933
8	13723.5838		13742.8270
9	13722.1208		13743.6212
10	13720.6100		
11			13745.0983

(0, 1)			
J	P	Q	R
3			12792.6593
4		12787.9816	12793.6818
5		12787.8384	12794.6782
6		12787.6642	12795.6482
7		12787.4623	
8		12787.2312	12797.4933
9		12786.9691	12798.3703

^{99}RuC

(1, 1)				
J	F	P	Q	R
3	5.5			13738.3886
	4.5			13738.3626
	3.5			13738.3401
	2.5			13738.3222
	1.5			13738.3108
	0.5			13738.3015
4	6.5			13739.3639
	5.5			13739.3454
	4.5			13739.3303
	3.5			13739.3174
	2.5			13739.3071
	1.5			13739.3005
5	7.5	13727.8675		13740.3017
	6.5	13727.8542		13740.2864
	5.5	13727.8428		13740.2720
	4.5	13727.8333		13740.2612
	3.5	13727.8265		13740.2549
	2.5	13727.8199		13740.2490
6	8.5	13726.5097	13733.2911	13741.2095
	7.5	13726.4977	13733.2785	13741.1972
	6.5	13726.4889	13733.2673	13741.1859
	5.5	13726.4801	13733.2590	13741.1754
	4.5	13726.4731	13733.2531	13741.1659
	3.5	13726.4663	13733.2484	13741.1576
7	9.5	13725.1170		13742.0741
	8.5	13725.1065		13742.0639
	7.5	13725.0969		13742.0575
	6.5	13725.0900		13742.0505
	5.5	13725.0844		13742.0441
	4.5	13725.0788		13742.0382
8	10.5	13723.6844	13732.7282	13742.9027
	9.5	13723.6741	13732.7184	13742.8921
	8.5	13723.6666	13732.7100	13742.8843
	7.5	13723.6619	13732.7036	13742.8787
	6.5	13723.6583	13732.6994	13742.8730
	5.5	13723.6558	13732.6961	13742.8685
9	11.5	13722.2167	13732.3914	13743.6968
	10.5	13722.2079	13732.3842	13743.6889
	9.5	13722.2018	13732.3769	13743.6833
	8.5	13722.1966	13732.3711	13743.6765
	7.5	13722.1941	13732.3666	13743.6725
	6.5	13722.1909	13732.3626	13743.6684

10	12.5	13720.7157	13732.0175	13744.4548
	11.5	13720.7078	13732.0100	13744.4478
	10.5	13720.7009	13732.0039	13744.4418
	9.5	13720.6956	13731.9989	13744.4354
	8.5	13720.6918	13731.9951	13744.4309
	7.5	13720.6884	13731.9923	13744.4274
11	13.5	13719.1734	13731.6074	13745.1745
	12.5	13719.1671	13731.6001	13745.1678
	11.5	13719.1613	13731.5945	13745.1625
	10.5	13719.1558	13731.5899	13745.1578
	9.5	13719.1516	13731.5865	13745.1548
	8.5	13719.1469	13731.5834	13745.1523
12	14.5	13717.5968		13745.8541
	13.5	13717.5914		13745.8493
	12.5	13717.5852		13745.8445
	11.5	13717.5806		13745.8403
	10.5	13717.5770		13745.8357
	9.5	13717.5740		13745.8318
13	15.5	13715.9791		
	14.5	13715.9730		
	13.5	13715.9682		
	12.5	13715.9645		
	11.5	13715.9617		
	10.5	13715.9582		

(0, 1)				
J	F	P	Q	R
3	5.5			12793.2878
	4.5			12793.2526
	3.5			12793.2260
	2.5			12793.2087
	1.5			12793.1986
	0.5			12793.1907
4	6.5		12788.6037	12794.2991
	5.5		12788.5847	12794.2789
	4.5		12788.5676	12794.2613
	3.5		12788.5541	12794.2471
	2.5		12788.5443	12794.2353
	1.5		12788.5362	12794.2262
5	7.5	12782.7582	12788.4535	12795.2855
	6.5	12782.7427	12788.4379	12795.2692
	5.5	12782.7301	12788.4238	12795.2557
	4.5	12782.7195	12788.4125	12795.2437
	3.5	12782.7108	12788.4029	12795.2358
	2.5	12782.7043	12788.3952	12795.2284
6	8.5	12781.4421	12788.2745	12796.2508
	7.5	12781.4305	12788.2620	12796.2368
	6.5	12781.4193	12788.2513	12796.2249
	5.5	12781.4113	12788.2427	12796.2154
	4.5	12781.4037	12788.2351	12796.2080
	3.5	12781.3956	12788.2286	12796.2021
7	9.5	12780.0976	12788.0687	12797.1819
	8.5	12780.0881	12788.0585	12797.1695
	7.5	12780.0795	12788.0501	12797.1594
	6.5	12780.0719	12788.0438	12797.1514
	5.5		12788.0375	12797.1454
	4.5		12788.0319	12797.1410
8	10.5	12778.7250	12787.8377	12798.0835
	9.5	12778.7168	12787.8290	12798.0737
	8.5	12778.7097	12787.8204	12798.0663
	7.5	12778.7031	12787.8149	12798.0589
	6.5	12778.6966	12787.8076	12798.0534
	5.5	12778.6916	12787.8034	12798.0491
9	11.5	12777.3265	12787.5729	12798.9623
	10.5	12777.3186	12787.5655	12798.9528
	9.5	12777.3117	12787.5586	12798.9449
	8.5	12777.3053	12787.5525	12798.9394
	7.5	12777.3005	12787.5475	12798.9341
	6.5	12777.2965	12787.5417	12798.9308
10	12.5		12787.2854	12799.8122

	11.5	12787.2780	12799.8034
	10.5	12787.2706	12799.7961
	9.5	12787.2651	12799.7906
	8.5	12787.2602	12799.7866
	7.5	12787.2562	12799.7833
11	13.5	12786.9670	
	12.5	12786.9594	
	11.5	12786.9531	
	10.5	12786.9479	
	9.5	12786.9445	
	8.5	12786.9411	
12	14.5		12801.4209
	13.5		12801.4138
	12.5		12801.4076
	11.5		12801.4025
	10.5		12801.3980
	9.5		12801.3936

^{100}RuC

(0, 0)			
J	P	Q	R
3			13824.4255
4		13819.7289	13825.4124
5	13813.8568	13819.5472	13826.3731
6	13812.5015	13819.3299	13827.2942
7	13811.1111	13819.0794	13828.1755
8	13809.6814	13818.7839	13829.0206
9	13808.2201	13818.4588	13829.8346
10	13806.7189	13818.0951	
11	13805.1835	13817.6953	
12	13803.6090	13817.2560	
13	13802.0012	13816.7863	
14		13816.2789	

(1, 1)			
J	P	Q	R
3			13738.4101
4		13733.7447	13739.3924
5	13727.9128	13733.5589	13740.3364
6	13726.5607	13733.3334	13741.2409
7	13725.1732	13733.0718	13742.1102
8	13723.7437	13732.7780	13742.9422
9	13722.2826	13732.4441	13743.7363
10	13720.7841	13732.0721	13744.4942
11	13719.2447	13731.6666	13745.2131
12	13717.6704		13745.8946
13	13716.0580	13730.7346	

	(0, 1)		
J	P	Q	R
3			12793.8045
4		12789.1419	12794.8279
5	12783.3045	12788.9949	12795.8228
6	12781.9960	12788.8232	12796.7880
7	12780.6570	12788.6217	12797.7218
8	12779.2909		12798.6290
9	12777.8910	12788.1330	12799.5050
10	12776.4681	12787.8384	12800.3551
11	12775.0143	12787.5247	12801.1752
12		12787.1804	12801.9650
13		12786.8020	12802.7283
14			12803.4632
15			12804.1676

^{101}RuC

(1, 1)				
J	F	P	Q	R
3	5.5			13738.5160
	4.5			13738.4875
	3.5			13738.4611
	2.5			13738.4415
	1.5			13738.4303
	0.5			13738.4231
4	6.5			13739.4866
	5.5			13739.4656
	4.5			13739.4479
	3.5			13739.4343
	2.5			13739.4243
	1.5			13739.4157
5	7.5	13728.0174		13740.4247
	6.5	13728.0012		13740.4094
	5.5	13727.9870		13740.3960
	4.5	13727.9775		13740.3835
	3.5	13727.9675		13740.3743
	2.5	13727.9608		13740.3675
6	8.5	13726.6599	13733.4282	13741.3268
	7.5	13726.6480	13733.4146	13741.3117
	6.5	13726.6369	13733.4037	13741.3008
	5.5	13726.6293	13733.3954	13741.2930
	4.5	13726.6228	13733.3889	13741.2849
	3.5	13726.6165	13733.3827	13741.2789
7	9.5	13725.2715	13733.1654	13742.1915
	8.5	13725.2608	13733.1550	13742.1805
	7.5	13725.2522	13733.1455	13742.1712
	6.5	13725.2452	13733.1384	13742.1629
	5.5	13725.2387	13733.1318	13742.1556
	4.5	13725.2331	13733.1263	13742.1488
8	10.5	13723.8439	13732.8656	13743.0187
	9.5	13723.8342	13732.8568	13743.0073
	8.5	13723.8252	13732.8492	13742.9989
	7.5	13723.8187	13732.8430	13742.9918
	6.5	13723.8129	13732.8360	13742.9862
	5.5	13723.8078	13732.8317	13742.9810
9	11.5	13722.3793	13732.5307	13743.8103
	10.5	13722.3694	13732.5228	13743.8014
	9.5	13722.3616	13732.5149	13743.7946
	8.5	13722.3552	13732.5089	13743.7888
	7.5	13722.3506	13732.5038	13743.7834
	6.5	13722.3463	13732.4993	13743.7786
10	12.5	13720.8795	13732.1594	13744.5652

	11.5	13720.8723	13732.1507	13744.5588
	10.5	13720.8660	13732.1433	13744.5524
	9.5	13720.8612	13732.1376	13744.5460
	8.5	13720.8565	13732.1328	13744.5403
	7.5	13720.8527	13732.1291	13744.5361
11	13.5	13719.3396	13731.7480	13745.2826
	12.5	13719.3336	13731.7407	13745.2762
	11.5	13719.3282	13731.7343	13745.2706
	10.5	13719.3240	13731.7295	13745.2659
	9.5	13719.3189	13731.7260	13745.2615
	8.5	13719.3139	13731.7223	13745.2581
12	14.5	13717.7656		13745.9629
	13.5	13717.7594		13745.9576
	12.5	13717.7548		13745.9523
	11.5	13717.7497		13745.9482
	10.5	13717.7454		13745.9435
	9.5	13717.7414		13745.9392
13	15.5	13716.1567		
	14.5	13716.1500		
	13.5	13716.1449		
	12.5	13716.1404		
	11.5	13716.1371		
	10.5	13716.1353		

		(0, 1)		
J	F	P	Q	R
3	5.5			12794.4192
	4.5			12794.3828
	3.5			12794.3512
	2.5			12794.3288
	1.5			
	0.5			
4	6.5			12795.4302
	5.5			12795.4015
	4.5			12795.3790
	3.5			12795.3651
	2.5			12795.3521
	1.5			12795.3432
5	7.5	12783.9126	12789.5971	12796.4137
	6.5	12783.8956	12789.5762	12796.3913
	5.5	12783.8807	12789.5603	12796.3748
	4.5	12783.8680	12789.5469	12796.3622
	3.5	12783.8574	12789.5359	12796.3525
	2.5	12783.8490	12789.5274	12796.3446
6	8.5	12782.5997	12789.4201	12797.3712
	7.5	12782.5857	12789.4036	12797.3542
	6.5	12782.5733	12789.3904	12797.3398
	5.5	12782.5625	12789.3790	12797.3292
	4.5	12782.5532	12789.3700	12797.3206
	3.5	12782.5455	12789.3640	12797.3130
7	9.5	12781.2590	12789.2148	12798.3012
	8.5	12781.2472	12789.1980	12798.2873
	7.5	12781.2365	12789.1872	12798.2756
	6.5	12781.2271	12789.1776	12798.2656
	5.5	12781.2188	12789.1685	12798.2584
	4.5	12781.2118	12789.1610	12798.2523
8	10.5	12779.8902		12799.2043
	9.5	12779.8799		12799.1927
	8.5	12779.8706		12799.1824
	7.5	12779.8622		12799.1742
	6.5	12779.8548		12799.1673
	5.5	12779.8483		12799.1613
9	11.5	12778.4930	12788.7165	12800.0799
	10.5	12778.4839	12788.7071	12800.0690
	9.5	12778.4757	12788.6986	12800.0601
	8.5	12778.4681	12788.6912	12800.0516
	7.5	12778.4614	12788.6847	12800.0440
	6.5	12778.4554	12788.6793	12800.0374
10	12.5		12788.4286	12800.9263
	11.5		12788.4205	12800.9174

	10.5	12788.4139	12800.9088
	9.5	12788.4070	12800.9015
	8.5	12788.4019	12800.8964
	7.5	12788.3955	12800.8910
11	13.5	12788.1105	12801.7450
	12.5	12788.1030	12801.7374
	11.5	12788.0961	12801.7314
	10.5	12788.0897	12801.7244
	9.5	12788.0839	12801.7179
	8.5	12788.0786	12801.7123
12	14.5	12787.7650	12802.5374
	13.5	12787.7569	12802.5296
	12.5	12787.7501	12802.5225
	11.5	12787.7440	12802.5154
	10.5	12787.7390	
	9.5	12787.7345	
13	15.5	12787.3884	
	14.5	12787.3822	12803.2890
	13.5	12787.3763	12803.2854
	12.5	12787.3709	12803.2778
	11.5	12787.3659	12803.2713
	10.5	12787.3613	12803.2664

^{102}RuC

(0, 0)			
J	P	Q	R
3			13824.4558
4		13819.7675	13825.4475
5	13813.9094	13819.5861	13826.3982
6	13812.5558	13819.3692	13827.3136
7	13811.1668	13819.1192	13828.1978
8	13809.7413	13818.8255	13829.0376
9	13808.2812	13818.4990	13829.8530
10	13806.7842	13818.1344	13830.6238
11	13805.2512	13817.7359	13831.3583
12	13803.6829	13817.3020	
13	13802.0772	13816.8300	
14		13816.3200	13833.3413
15		13815.7780	
16		13815.1910	13834.4900

(1, 1)			
J	P	Q	R
3			13738.5317
4		13733.8728	13739.5121
5	13728.0582	13733.6885	13740.4534
6	13726.7049	13733.4693	13741.3582
7	13725.3197	13733.2076	13742.2247
8	13723.8960	13732.9114	13743.0538
9	13722.4386	13732.5783	13743.8459
10	13720.9383	13732.2077	13744.6012
11	13719.4060	13731.7993	13745.3195
12	13717.8339		13745.9983
13	13716.2270	13730.8702	13746.6417
14	13714.5804	13730.3539	13747.2462
15		13729.7972	

	(0, 1)		
J	P	Q	R
3			12794.9097
4		12790.2531	12795.9307
5	12784.4339	12790.1095	12796.9209
6	12783.1247	12789.9361	12797.8828
7	12781.7897	12789.7368	12798.8172
8	12780.4247	12789.5076	12799.7225
9	12779.0316	12789.2465	12800.5989
10	12777.6106	12788.9616	12801.4449
11	12776.1592	12788.6425	12802.2615
12	12774.6808	12788.2950	12803.0521
13		12787.9234	12803.8119
14		12787.5247	12804.5427
15		12787.0882	12805.2432

^{104}RuC

(0, 0)			
J	P	Q	R
3			13824.4744
4		13819.8016	13825.4611
5	13813.9562	13819.6222	13826.4179
6	13812.6052	13819.4036	13827.3350
7	13811.2216	13819.1511	13828.2136
8	13809.7994	13818.8625	13829.0545
9	13808.3397	13818.5370	13829.8613
10	13806.8467	13818.1751	
11	13805.3178	13817.7767	
12	13803.7498	13817.3412	
13	13802.1494	13816.8726	
14		13816.3650	
15		13815.8226	
16		13815.2440	

(1, 1)			
J	P	Q	R
3			13738.6463
4		13733.9986	13739.6217
5	13728.1914	13733.8126	13740.5644
6	13726.8447	13733.5939	13741.4667
7	13725.4630	13733.3334	13742.3314
8	13724.0403	13733.0357	13743.1594
9	13722.5856	13732.7043	13743.9493
10	13721.0905	13732.3347	13744.7026
11	13719.5592	13731.9275	13745.4203
12	13717.9917	13731.4827	13746.0981
13	13716.3852	13730.9996	13746.7395
14	13714.7433	13730.4848	13747.3441
15		13729.9265	

	(0, 1)		
J	P	Q	R
3			12795.9716
4		12791.3231	12796.9895
5	12785.5188	12791.1809	12797.9783
6	12784.2102	12791.0082	12798.9402
7	12782.8767	12790.8078	12799.8705
8	12781.5122	12790.5775	12800.7742
9	12780.1217	12790.3194	12801.6477
10	12778.7097	12790.0325	12802.4944
11		12789.7168	12803.3086
12			12804.0966
13		12788.9949	12804.8533
14			12805.5837

Assigned rotational lines of the $[13.5]^3\Phi_3$-$[0.9]^3\Delta_2$ transition

^{96}RuC

(0, 0)			
J	P	Q	R
2			12627.4951
3			12628.5007
4	12619.2162	12623.7701	12629.4618
5	12617.8571	12623.5511	12630.3793
6	12616.4595	12623.2854	12631.2518
7	12615.0123	12622.9796	12632.0823
8	12613.5198	12622.6235	12632.8693
9	12611.9871	12622.2303	12633.6108
10		12621.7928	12634.3090
11		12621.3053	12634.9619
12		12620.7761	

(1, 1)			
J	P	Q	R
2			12537.3388
3			12538.3351
4	12529.1176	12533.6365	12539.2852
5	12527.7593	12533.4125	12540.1886
6	12526.3685		12541.0498
7			12541.8674
8			12542.6358

^{98}RuC

	(0, 0)		
J	P	Q	R
2			12627.5308
3		12623.9971	12628.5397
4	12619.2726		12629.4970
5			12630.4082
6			
7			
8	12613.5855	12622.6662	
9	12612.0571		

^{99}RuC

(1, 0)			
J	P	Q	R
2			13569.0923
3		13565.5572	13570.0628
4	13560.8381	13565.3426	13570.9741
5			13571.8375
6	13558.0063	13564.7656	
7	13556.5196	13564.3956	13573.4073
8	13554.9784	13563.9822	13574.1153
9	13553.3820		13574.7697
10		13562.9810	13575.3711
11		13562.4115	13575.9215
12		13561.7845	13576.4157

^{100}RuC

(0, 0)			
J	P	Q	R
2			12627.5607
3		12624.0328	12628.5627
4	12619.3199	12623.8531	12629.5198
5	12617.9624	12623.6336	12630.4332
6	12616.5695	12623.3661	12631.3007
7	12615.1322	12623.0595	12632.1306
8	12613.6488		12632.9084
9	12612.1224	12622.3169	12633.6504
10	12610.5502	12621.8818	
11	12608.9368	12621.3974	
12		12620.8724	

(1, 1)			
J	P	Q	R
2			12537.6150
3		12534.1023	12538.6019
4	12529.4226	12533.9232	12539.5488
5	12528.0740	12533.7006	12540.4509
6	12526.6830	12533.4310	
7	12525.2494	12533.1205	
8		12532.7622	12542.8862
9	12522.2382	12532.3588	
10	12520.6655		
11	12519.0532		
12			
13		12530.3047	

	(1, 0)		
J	P	Q	R
2			
3			13569.5641
4		13564.8532	13570.4803
5	13558.968		13571.3423
6		13564.2803	13572.1538
7	13556.0433	13563.9167	13572.9120
8	13554.4986		13573.6189
9	13552.9044		13574.2733
10	13551.2604	13562.5048	13574.8727
11		13561.9302	
12	13547.8060	13561.3040	13575.9215
13		13560.6253	
14		13559.8929	
15		13559.1084	
16		13558.2731	

^{101}RuC

(1, 0)			
J	P	Q	R
2			13568.1213
3		13564.5946	13569.0923
4	13559.8929		13570.0067
5		13564.1243	13570.8649
6	13557.0716	13563.8129	13571.6758
7	13555.5813	13563.4491	13572.4358
8	13554.0412		13573.1411
9	13552.4523	13562.5631	13573.7943
10	13550.8052	13562.0393	13574.3974
11	13549.1074	13561.4656	13574.9484
12	13547.3642	13560.8381	
13	13545.5578		
14	13543.7035	13559.4300	
15		13558.6430	
16		13557.8118	
17		13556.9215	
18		13555.9816	

^{102}RuC

(0, 0)			
J	P	Q	R
2			12627.5928
3		12624.0648	12628.5919
4	12619.3703	12623.8924	12629.5453
5	12618.0204	12623.6727	12630.4586
6	12616.6266	12623.4111	12631.3260
7	12615.1903	12623.1038	12632.1515
8	12613.7116	12622.7544	12632.9321
9	12612.1858	12622.3610	12633.6674
10	12610.6205	12621.9248	12634.3619
11	12609.0091	12621.4442	12635.0120
12		12620.9210	12635.6155
13		12620.3520	12636.1790
14		12619.7338	12636.6955
15			
16			12637.5964

(1, 1)			
J	P	Q	R
2			12537.7413
3		12534.2377	12538.7236
4	12529.5723	12534.0585	12539.6719
5	12528.2267	12533.8385	12540.5726
6	12526.8355	12533.5687	12541.4244
7	12525.4018	12533.2574	12542.238
8	12523.9272	12532.9018	12543.0031
9	12522.4016	12532.5017	12543.7241
10	12520.8323	12532.0526	12544.3997
11	12519.2249	12531.5683	12545.0317
12			
13		12530.4511	

	(1, 0)		
J	P	Q	R
2			13567.6522
3		13564.1243	
4	13559.4300	13563.9167	13569.5319
5	13558.0444	13563.6576	13570.3926
6	13556.6103	13563.3452	13571.2006
7	13555.1218	13562.9810	13571.9576
8	13553.5836	13562.5631	
9	13551.9931		13573.3159
10	13550.3505	13561.5730	13573.9152
11	13548.6540	13560.9995	
12	13546.9102		
13	13545.1092	13559.6958	
14	13543.2600		
15		13558.1827	
16		13557.3489	

^{104}RuC

(0, 0)			
J	P	Q	R
2			12627.6182
3		12624.1028	12628.6157
4	12619.4161	12623.9293	12629.5722
5	12618.0683	12623.7116	12630.4790
6	12616.6785	12623.4503	12631.3490
7	12615.2455	12623.1454	12632.1720
8	12613.7693	12622.7967	12632.9507
9	12612.2474	12622.4047	12633.6812
10	12610.6837	12621.9680	12634.3774
11	12609.0760	12621.4882	12635.0242
12		12620.9643	12635.6267
13		12620.3954	
14		12619.7802	

(1, 1)			
J	P	Q	R
2			12537.8632
3		12534.3672	12538.8496
4	12529.7105	12534.1907	12539.7899
5	12528.3658	12533.9685	12540.6882
6	12526.9772	12533.7006	12541.5428
7	12525.5483	12533.3887	12542.3501
8	12524.0733		12543.1127
9	12522.5523	12532.6360	12543.8365
10	12520.9878		12544.5115
11	12519.3820		12545.1366
12			
13		12530.5853	

		(1, 0)	
J	P	Q	R
2			13566.7383
3		13563.2201	13567.7027
4			13568.6158
5	13557.1515	13562.7501	13569.4735
6	13555.7193	13562.4411	13570.2798
7	13554.2361		13571.0360
8	13552.6992	13561.6625	13571.7384
9	13551.1070	13561.1927	13572.3912
10	13549.4729	13560.6740	13572.9902
11	13547.7826	13560.1000	13573.5380
12	13546.0374	13559.4741	13574.0314
13	13544.2449	13558.8002	
14	13542.3968		
15		13557.2906	

Assigned rotational lines of the $[13.9]^3\Pi_1$-$[0.9]^3\Delta_2$ transition

^{96}RuC

	(0, 0)		
J	P	Q	R
2	13092.4084		
3	13091.1567	13094.5944	
4	13089.8674	13094.4522	
5	13088.5393	13094.2700	
6	13087.1751	13094.0531	
7	13085.7748	13093.7962	
8	13084.3407		
9	13082.8689	13093.1804	
10	13081.3599	13092.8194	

	(1, 1)		
J	P	Q	R
2	13019.9727	13022.2456	13025.6570
3	13018.7216		13026.6854
4	13017.4389		13027.6765
5	13016.1169		13028.6319
6	13014.7580		13029.5475
7	13013.3603		
8	13011.9287		
9	13010.4611		13032.0708
10	13008.9527		13032.8361

^{98}RuC

	(1, 1)		
J	P	Q	R
2	13020.0853		13025.7595
3	13018.8275		13026.7823
4	13017.5490		13027.7650
5	13016.2335		13028.7198
6			
7	13013.4770		13030.5114
8	13012.0582		
9	13010.5897		13032.1685

^{99}RuC

	(1, 1)		
J	P	Q	R
2	13020.1368		13025.8068
3	13018.8930		13026.8282
4	13017.6100	13022.1440	13027.8186
5	13016.2918		13028.7675
6	13014.9398		13029.6816
7	13013.5469	13021.4887	13030.5572
8	13012.1204	13021.1933	13031.4018
9	13010.6543	13020.8622	13032.2026
10	13009.1514	13020.4932	13032.9674
11		13020.0859	

^{100}RuC

	(1, 1)		
J	P	Q	R
2	13020.1849		13025.8469
3	13018.9426	13022.3396	13026.8690
4	13017.6625		13027.8566
5	13016.3449	13022.0079	13028.8033
6	13014.9943	13021.7936	13029.7186
7	13013.6028	13021.5335	13030.5955
8	13012.1778	13021.2406	13031.4346
9	13010.7147	13020.9118	13032.2381
10	13009.2115	13020.5441	13033.0013
11	13007.6803		

^{101}RuC

	(1, 1)		
J	P	Q	R
2	13020.2415	13022.5052	13025.8993
3	13018.9992	13022.3924	13026.9184
4	13017.7203	13022.2456	13027.9053
5	13016.4064	13022.0626	13028.8530
6	13015.0537	13021.8437	13029.7643
7	13013.6655	13021.5863	13030.6370
8	13012.2440	13021.2946	13031.4788
9	13010.7818	13020.9600	13032.2796
10	13009.2800	13020.5995	13033.0382
11	13007.7532		

^{102}RuC

(0, 0)			
J	P	Q	R
2	13092.0476	13094.7589	13098.1770
3	13091.2331	13094.6522	13099.2071
4	13089.9505	13094.5070	13100.2045
5	13088.6348	13094.3302	13101.1633
6	13087.2805	13094.1113	13102.0842
7	13085.8881	13093.8595	13102.9706
8	13084.4616		13103.8195
9	13083.0004	13093.2469	13104.6333
10	13081.5032	13092.8868	13105.4077
11	13079.9621	13092.4847	13106.1539
12		13092.0476	13106.8537
13			13108.1544
14			13108.7524
15			13098.1770

(1, 1)			
J	P	Q	R
2	13020.2857	13022.5419	13025.9389
3	13019.0441	13022.4372	13026.9587
4	13017.7679	13022.2907	13027.9421
5	13016.4559	13022.1051	13028.8882
6	13015.1062	13021.8883	13029.7988
7	13013.7191	13021.6327	13030.6741
8	13012.2950	13021.3372	13031.5110
9	13010.8358	13021.0128	13032.3139
10	13009.3456	13020.6440	13033.0694
11	13007.8093		

^{104}RuC

(1, 1)			
J	P	Q	R
2	13020.3819	13022.6378	13026.0195
3	13019.1433		13027.0409
4	13017.8668		13028.0211
5	13016.5593	13022.1978	13028.9686
6	13015.2121		13029.8729
7	13013.8289		13030.7517
8	13012.4073	13021.4297	13031.5864
9	13010.9500	13021.1061	13032.3835
10	13009.4583	13020.7414	13033.1416
11		13020.3368	13033.8744

Appendix 2 Line list of IrP

TABLE 1 Rotational Lines Assigned to the (v,0) band of the $[12.3]^1\Pi_1$ - $X^1\Sigma^+$ transition of ^{193}IrP(cm^{-1})

J	^{193}IrP		
	P	Q	R
0			12337.4882
1		12337.1681	12337.7420
2	12336.5346	12337.1026	12337.9675
3	12336.1519	12337.0164	12338.1605
4	12335.7391	12336.8862	12338.3238
5	12335.2928	12336.7322	12338.4498
6	12334.8264	12336.5459	12338.5550
7	12334.3194	12336.3228	12338.6226
8	12333.7825	12336.0746	12338.6584
9	12333.2160	12335.7936	12338.6656
10	12332.6200	12335.4798	12338.6373
11	12331.9876	12335.1360	12338.5841
12	12331.3243	12334.7619	12338.4985
13		12334.3585	12338.3788
14		12333.9204	12338.2277
15		12333.4507*	12338.0617(perturbed)
16		12332.9457*	12337.8413*
17		12332.4169*	12337.6029*
18		12331.8522*	12337.3240*
19			

* :did not include in fitting

TABLE 2 Rotational Lines Assigned to the (v+1,0) band of the $[12.3]^1\Pi_1$ - $X^1\Sigma^+$ transition of ^{193}IrP(cm^{-1})

J	^{193}IrP		
	P	Q	R
0			
1			
2		12815.4825	12816.3383
3		12815.388	12816.5341
4	12814.1151	12815.2589	12816.6928
5	12813.6687	12815.1003	12816.8180
6	12813.1905	12814.9092	12816.913
7	12812.6775	12814.6868	12816.9689
8	12812.1403	12814.4304	12817.0021
9	12811.5665	12814.1388	12817.0021
10	12810.9563	12813.8209	12816.9689
11	12810.3228	12813.4680	12816.8964
12	12809.6469	12813.0798	12816.7899*
13	12808.9444	12812.6696*	12816.6528*
14		12812.1988*	12816.4834*
15		12811.7158*	12816.2795*
16		12811.1920*	12816.0299*
17		12810.6384*	12815.7570*
18		12810.0409*	
19			

TABLE 3 Rotational Lines Assigned to the (v,0) band of the [13.4]2-2 transition of ^{191}IrP(cm^{-1})

J	^{191}IrP		
	P	Q	R
0			
1			
2		13358.4607	13359.3079
3	13357.56*	13358.3991	13359.5261
4	13357.1863	13358.3157	13359.72*
5	13356.8110	13358.2119	13359.8974
6	13356.4051	13358.0873	13360.0562
7	13355.9763	13357.9393	13360.1889
8	13355.5279	13357.78*	13360.3080
9	13355.0555	13357.59*	13360.4035
10	13354.5752	13357.38*	13360.4736
11	13354.06*	13357.1493	13360.5234
12	13353.5316	13356.9027	13360.56*
13	13352.9762	13356.6285	13360.58*
14	13352.4119	13356.34*	13360.56*
15	13351.82*	13356.0283	13360.53*
16	13351.2087	13355.70*	13360.48*
17	13350.57*	13355.35*	13360.40*
18	13349.9172	13354.97*	13360.31*
19		13354.58*	
20		13354.16*	
21			

TABLE 4 Rotational Lines Assigned to the (v,0) band of the [13.4]2-2 transition of ^{193}IrP(cm^{-1})

J	^{193}IrP		
	P	Q	R
0			
1			
2		13358.8322	13359.68*
3	13357.93*	13358.7709	13359.8974
4	13357.5679	13358.6878	13360.0916
5	13357.1863	13358.5852	13360.2709
6	13356.7773	13358.4607	13360.4275
7	13356.3502	13358.3157	13360.5600
8	13355.9053	13358.1492	13360.6763
9	13355.4381	13357.9594	13360.7689
10	13354.9542	13357.7618	13360.8429
11	13354.4364	13357.5283	13360.8952
12	13353.9078	13357.2788	13360.9295
13	13353.3597	13357.0074	13360.9295
14	13352.7909	13356.7198	13360.9295
15	13352.2008	13356.4051	13360.8952
16	13351.5923	13356.0761	13360.8429
17	13350.9605	13355.7183	13360.7689
18	13350.30*	13355.3450	13360.68*
19	13349.6300		13360.57*
20	13348.9338		13360.43*
21			13360.28*
22			13360.10*
23			13359.90*
24			

TABLE 5 Rotational Lines Assigned to the (v,0) band of the [13.6]3-2 transition of ^{191}IrP(cm^{-1})

J	^{191}IrP		
	P	Q	R
0			
1			
2			13553.9684
3		13553.0548	13554.19*
4	13551.8441	13552.9816	13554.3973
5	13351.47*	13552.89*	13554.59*
6	13551.0639	13552.77*	13554.7601
7		13552.6392	13554.91*
8	13550.2117	13552.4902	13555.04*
9	13549.7650	13552.3120	13555.16*
10	13549.2912	13552.1267	13555.25*
11	13548.7937	13551.92*	13555.33*
12	13548.2875	13551.6909	13555.38*
13	13547.7555	13551.4436	13555.42*
14	13547.2059	13551.1817	13555.44*
15	13546.6365	13550.8972	13555.44*
16	13546.0506	13550.5895	13555.42*
17	13545.4384	13550.2705	13555.38*
18		13549.93*	13555.32*
19		13549.57*	13555.25*
20		13549.19*	13555.15*
21			

TABLE 6 Rotational Lines Assigned to the (v,0) band of the [13.6]3-2 transition of ^{193}IrP(cm^{-1})

J	^{193}IrP		
	P	Q	R
0			
1			
2			13553.7776
3		13552.87*	13553.9956
4	13551.6552	13552.79*	13554.2018
5	13551.2786	13552.6966	13554.3967
6		13552.5741	13554.5611
7	13550.4607	13552.4466	13554.7144
8	13550.0295	13552.2954	13554.8451
9	13549.5694	13552.1267	13554.9556
10	13549.1034	13551.9287	13555.0461
11	13548.6081	13551.7242	13555.1161
12	13548.0973	13551.4953	13555.17*
13	13547.5683	13551.2496	13555.21*
14	13547.0170	13550.9829	13555.23*
15	13546.4482	13550.6956	13555.22*
16	13545.8614	13550.3924	13555.20*
17	13545.2491	13550.0666	13555.16*
18	13544.6283	13549.7235	13555.10*
19	13543.9784	13549.3632	13555.0203
20	13543.31*	13548.9800	13554.9188
21		13548.5773	13554.81*
22		13548.1579	13554.6732
23		13547.7217	13554.51*
24		13547.2588	
25		13546.78*	
26		13546.29*	
27		13545.77*	

Appendix 3 Line list of IrB

TABLE 1 Rotational Lines Assigned to the (v,0) band of the $[12.3]^3\Delta_3$-$X^3\Delta_3$ transition of $^{193}Ir^{11}B(cm^{-1})$

J	$^{193}Ir^{11}B$		
	P	Q	R
0			
1			
2			
3		12318.43*	12322.97**
4	12314.2830	12317.8566	12322.32*
5	12312.6739	12317.1434	12322.50*
6	12310.9242	12316.2867	12322.5340
7	12309.0257	12315.2804	12322.4199
8	12306.9864	12314.1357	12322.1700
9	12304.8063	12312.8400	12321.7701
10	12302.4843	12311.4080	12321.2310
11	12300.0180	12309.8386	12320.5450
12	12297.4035		12319.7258
13	12294.6511		12318.7566
14			12317.6444
15			

TABLE 2 Rotational Lines Assigned to the (v,0) band of the $[12.3]^3\Delta_3$-$X^3\Delta_3$ transition of $^{191}Ir^{11}B(cm^{-1})$

J	$^{191}Ir^{11}B$		
	P	Q	R
0			
1			
2			
3		12319.0136	12322.61**
4	12314.8647	12318.44*	12322.9108
5	12313.2540	12317.7200	12323.0916
6	12311.5050	12316.8642	12323.12*
7	12309.6090	12315.8563	12323.0086
8	12307.5704	12314.7125	12322.7558
9	12305.3846		12322.3579
10	12303.0589		12321.8164
11	12300.5883		12321.1378
12	12297.9771		12320.3081
13	12295.2213		12319.3390
14			

TABLE 3 Rotational Lines Assigned to the (v+1,0) band of the $[12.3]^3\Delta_3$-$X^3\Delta_3$ transition of $^{193}Ir^{11}B(cm^{-1})$

J	$^{193}Ir^{11}B$		
	P	Q	R
0			
1			
2			
3		13071.5951	13075.1497
4	13067.4567	13071.0058	13075.4490
5	13065.8286	13070.2654	13075.5951
6	13064.0481	13069.3764	13075.5995
7	13062.1256	13068.3427	13075.4490
8	13060.0568	13067.1614	13075.1513
9	13057.8357	13065.8286	13074.7092
10	13055.4657	13064.3424	13074.1131
11	13052.9499	13062.7164	13073.3780
12	13050.2854		13072.4847
13	13047.47**		13071.4450
14	13044.52**		13070.2654
15	13041.41**		13068.9285
16			

TABLE 4 Rotational Lines Assigned to the (v+1,0) band of the $[12.3]^3\Delta_3$-$X^3\Delta_3$ transition of $^{191}Ir^{11}B(cm^{-1})$

J	$^{191}Ir^{11}B$		
	P	**Q**	**R**
0			
1			
2			
3		13072.3875	13075.9506
4	13068.2487	13071.8008	
5	13066.6186	13071.0605	
6	13064.8375	13070.1701	
7	13062.9139	13069.1335	
8	13060.8409	13067.9500	13075.9452
9	13058.6223	13066.6186	13075.50*
10	13056.2509	13065.1320	13074.9102
11	13053.7350	13063.5057	13074.1681
12	13051.0661		13073.2790
13	13048.26**		13072.2409
14	13045.29**		13071.06*
15	13042.19**		13069.7223
16			